

January 2016

# MULTISCALE SIMULATIONS OF THERMAL TRANSPORT IN GRAPHENE-BASED MATERIALS AND ACROSS METAL- SEMICONDUCTOR INTERFACES

Yan Wang  
*Purdue University*

Follow this and additional works at: [https://docs.lib.purdue.edu/open\\_access\\_dissertations](https://docs.lib.purdue.edu/open_access_dissertations)

---

## Recommended Citation

Wang, Yan, "MULTISCALE SIMULATIONS OF THERMAL TRANSPORT IN GRAPHENE-BASED MATERIALS AND ACROSS METAL-SEMICONDUCTOR INTERFACES" (2016). *Open Access Dissertations*. 1399.  
[https://docs.lib.purdue.edu/open\\_access\\_dissertations/1399](https://docs.lib.purdue.edu/open_access_dissertations/1399)

This document has been made available through Purdue e-Pubs, a service of the Purdue University Libraries. Please contact [epubs@purdue.edu](mailto:epubs@purdue.edu) for additional information.

**PURDUE UNIVERSITY  
GRADUATE SCHOOL  
Thesis/Dissertation Acceptance**

This is to certify that the thesis/dissertation prepared

By YAN WANG

Entitled

MULTISCALE SIMULATIONS OF THERMAL TRANSPORT IN GRAPHENE-BASED MATERIALS AND ACROSS  
METAL-SEMICONDUCTOR INTERFACES

For the degree of Doctor of Philosophy

Is approved by the final examining committee:

Xiulin Ruan

Chair

Alejandro Strachan

Mark S. Lundstrom

Timothy S. Fisher

To the best of my knowledge and as understood by the student in the Thesis/Dissertation Agreement, Publication Delay, and Certification Disclaimer (Graduate School Form 32), this thesis/dissertation adheres to the provisions of Purdue University's "Policy of Integrity in Research" and the use of copyright material.

Approved by Major Professor(s): Xiulin Ruan

Approved by: Jay P. Gore

Head of the Departmental Graduate Program

6/20/2016

Date

MULTISCALE SIMULATIONS OF THERMAL TRANSPORT IN  
GRAPHENE-BASED MATERIALS AND ACROSS METAL-SEMICONDUCTOR  
INTERFACES

A Dissertation

Submitted to the Faculty

of

Purdue University

by

Yan Wang

In Partial Fulfillment of the

Requirements for the Degree

of

Doctor of Philosophy

August 2016

Purdue University

West Lafayette, Indiana

## ACKNOWLEDGMENTS

It has been nearly six years since I came to West Lafayette to pursue my Ph.D. degree. I still vividly remember when Prof. Xiulin Ruan mentioned DFT in our first meeting, Discrete Fourier Transform was the term that came to my mind, since I just obtained my bachelor's degree in Measurement and Control; while it turned out to be Density Functional Theory, which is a quantum mechanical modeling method that I would use extensively as a Ph.D. student in thermal science. Despite the great uncertainty at the beginning, the journey to this entirely new area has turned out to be exciting and rewarding, for which I would like to express my sincere gratitude to everyone I met during this period.

First, I would like to express my deepest gratitude to my Ph.D. advisor, Prof. Xiulin Ruan, for his continued support, guidance, and encouragement throughout my doctoral study at Purdue. Prof. Ruan devoted tremendous time and efforts to guide me into the wonderland of thermal science. He has granted me great freedom in research and provided me with invaluable advice throughout my graduate study, so that I was able to keep a smooth progress in research. I appreciate Prof. Ruan's trust in me for granting me the chance to present my work in IMECE-2011 as a second-year Ph.D. student and write research proposals with him after I became more senior, from which I have gained the confidence and skills required for an independent researcher. Prof. Ruan has also been a great mentor and role model to me, who has helped me countless in life and career.

I would also like to thank the members of my thesis committee, Prof. Alejandro H. Strachan, Prof. Mark S. Lundstrom, and Prof. Timothy S. Fisher, for their constructive and insightful advice that has significantly improved the quality of my work. My work on superlattice and random multilayer has benefited a lot from Prof. Strachan's precedent work as well as our fruitful discussions on phonon nonequilibrium



in heat bath in molecular dynamics simulations. I benefited significantly from Prof. Lundstrom's textbooks and classes on carrier transport and our collaborations in the DARPA project, which have helped me gain a deeper understanding of Albert Einstein's quote: "Make things as simple as possible, but not simpler." I enjoyed my interactions with Prof. Fisher in his ME503 class and during our collaborations in the MURI program, through which I learnt how a great researcher and entrepreneur thinks.

I am grateful to Dr. Ajit K. Roy from the Airforce Research Lab, and Prof. Yue Wu, who is now at Iowa State University, for their support in my research and career. I would like to thank Prof. Ali Shakouri, Prof. Xianfan Xu, and Prof. Yong Chen, because of whom I have enjoyed the collaborative research environment at Purdue. I want to express my sincere appreciation to former Purdue students Ajit Vallabhaneni, Bo Qiu, Eshaan Matthew, Guoping Xiong, Hua Bao, Jiuning Hu, Liangliang Chen, Liang Guo, and Yalin Dong for their countless help. I would like to specially thank Bo Qiu, with whom I had lots of fruitful discussions regarding research, career, and life. Bo and his wife, Jianfang, have unreservedly shared their career experience with me. In addition, I have received countless help from: Amr Mohammed Shahat Mohammed, Chongjie Gu, Haoxiang Huang, Jingjing Shi, Kelly Rickey, Rajib Paul, Scott W. Finefrock, Siyu Chen, Tianli Feng, Xiangyu Li, Xin Jin, Zexi Lu, Zhifeng Huang, and Zuyuan Wang. I am grateful to the Frederick N. Andrews Fellowship and the Bilsland Dissertation Fellowship provided by Purdue University as well as the financial support from AFOSR, NSF, and DARPA.

Last but not least, I would like to thank my parents and my sister for their unconditional love and support for me. I would like to thank my wife, Lei Cao, for her consistent and unselfish love to me and devotion to the family. I am thankful to my son Leo for giving me happiness during the last one year of my Ph.D. study. It is because of my family that I have enjoyed my life at Purdue so much, and it is because of them that I can always keep optimistic towards my life.

## TABLE OF CONTENTS

	Page
LIST OF TABLES . . . . .	vii
LIST OF FIGURES . . . . .	viii
ABSTRACT . . . . .	xvi
1. INTRODUCTION . . . . .	1
1.1 Thermal Issues in Electronic Devices . . . . .	1
1.2 Thermal Transport in Graphene . . . . .	3
1.2.1 Horizontal Alignment of Graphene on Substrate . . . . .	3
1.2.2 Vertical Alignment of Graphene on Substrate . . . . .	5
1.2.3 3D Architectures . . . . .	6
1.2.4 Beyond Phonon-phonon Coupling . . . . .	6
1.3 Thermal Rectification . . . . .	7
1.4 Numerical Methods for Thermal Transport . . . . .	8
1.4.1 Classical Molecular Dynamics Simulations . . . . .	8
1.4.2 Nonequilibrium Green's Function Method . . . . .	11
1.4.3 Boltzmann Transport Equation . . . . .	12
1.5 Objective . . . . .	13
1.6 Organization of this thesis . . . . .	14
2. THERMAL CONDUCTIVITY OF GRAPHENE NANORIBBONS . . . . .	15
2.1 Introduction . . . . .	15
2.2 Methodology . . . . .	17
2.3 Results and Discussions . . . . .	18
2.4 Summary . . . . .	22
3. THERMAL RECTIFICATION . . . . .	23
3.1 Introduction . . . . .	23
3.2 Homogeneous Nanoribbon . . . . .	24
3.3 Asymmetrically Defected Graphene Nanoribbon . . . . .	37
3.4 Summary . . . . .	45
4. THERMAL TRANSPORT IN MULTILAYER STRUCTURES . . . . .	47
4.1 Introduction . . . . .	47
4.2 Methodology . . . . .	51
4.2.1 Simulation Setup . . . . .	51
4.2.2 Model Structures . . . . .	54
4.2.3 Convergence Study . . . . .	55

	Page
4.2.4 Simulation Uncertainty . . . . .	57
4.3 Two-phonon Model . . . . .	57
4.4 Results and Discussions . . . . .	59
4.4.1 Effect of Random Layer Thickness . . . . .	59
4.4.2 Transition between Coherent and Incoherent Behavior . . . .	63
4.4.3 Thermal Boundary Resistance of Individual Interfaces in SL and RML . . . . .	66
4.4.4 Comparison between the Effect of Random Layer Thickness, Interface Mixing, and Interface Roughness . . . . .	69
4.5 Summary . . . . .	74
5. TWO-TEMPERATURE MOLECULAR DYNAMICS SIMULATION OF THERMAL TRANSPORT ACROSS METAL-NONMETAL INTERFACES	76
5.1 Introduction . . . . .	76
5.2 Theory . . . . .	78
5.2.1 Two-temperature Model . . . . .	78
5.2.2 Input Parameters . . . . .	83
5.3 Case Studies . . . . .	87
5.3.1 Pure Copper . . . . .	87
5.3.2 Si-Cu Interface . . . . .	91
5.3.3 CNT-Cu Interface . . . . .	96
5.4 Summary . . . . .	98
6. FIRST-PRINCIPLES CALCULATION OF PHONON-ELECTRON AND PHONON-PHONON SCATTERING RATES IN SOLIDS . . . . .	99
6.1 Introduction . . . . .	99
6.2 Methodology . . . . .	100
6.2.1 Phonon-phonon Scattering . . . . .	100
6.2.2 Phonon-electron Scattering . . . . .	103
6.2.3 Lattice Thermal Conductivity . . . . .	104
6.3 Results and Discussions . . . . .	106
6.3.1 Cu, Ag, and Au: Noble Metals with Weak Electron-phonon Interaction . . . . .	106
6.3.2 Pt and Ni: d-band Metals with Strong Electron-phonon Inter- action . . . . .	111
6.3.3 Al: Metal with Intermediate Electron-phonon Coupling Con- stant . . . . .	113
6.4 Summary . . . . .	113
7. TWO-TEMPERATURE BOLTZMANN TRANSPORT EQUATION SIM- ULATION OF THERMAL TRANSPORT ACROSS LAYERED METAL- NONMETAL STRUCTURES . . . . .	117
7.1 Introduction . . . . .	117
7.2 Two-temperature Boltzmann Transport Equation . . . . .	118

	Page
7.3 Input Parameters . . . . .	120
7.3.1 Bulk Properties: $v_p$ , $c_p$ , $\tau_p$ , and $\tau_e$ . . . . .	121
7.3.2 Interfacial Thermal Transport Properties . . . . .	123
7.4 Results and Discussions . . . . .	125
7.4.1 Steady-State Thermal Transport . . . . .	125
7.4.2 Ultrafast Electron Cooling in Au Thin Films . . . . .	129
7.5 Summary . . . . .	132
8. MONTE CARLO BASED SPECTRAL BOLTZMANN SIMULATION OF ELECTRON-PHONON COUPLED THERMAL TRANSPORT ACROSS METAL-SEMICONDUCTOR INTERFACES . . . . .	133
8.1 Introduction . . . . .	133
8.2 Methodology: Monte Carlo Boltzmann Solver . . . . .	136
8.3 Results and Discussions . . . . .	140
8.4 Summary . . . . .	142
9. SUMMARY . . . . .	143
LIST OF REFERENCES . . . . .	146
VITA . . . . .	161

## LIST OF TABLES

Table	Page
4.1 The effect of heat bath length $L_{bath}$ , temperature bias $\Delta T$ and cross-sectional area $A$ on the prediction of the thermal conductivity $\kappa$ of LJ04 $\epsilon_{Ar}$ and LJ16 $\epsilon_{Ar}$ SLs with layer thickness $\delta = 4.3$ nm and total device length $L_{tot} = 137$ nm at $T = 30$ K. . . . .	56
5.1 $g_{ep}$ for Cu obtained via various methods. . . . .	83
5.2 $\kappa$ of Cu obtained via different methods. Table reproduced from Ref. [24].	90
5.3 Comparison of $R_I$ of CNT-Cu interface from MD, TTM-MD and experiment. Table reproduced from Ref. [24]. . . . .	97
6.1 Material properties of Cu, Ag, Au, Al, Pt, and Ni. The 2nd column is the electron configuration of these elements. Columns 3 and 4 are the lattice constants calculated through structural relaxation in this work using LDA and GGA, respectively, while column 5 shows the experimental data. Columns 6 and 7 are the electron-phonon mass enhancement parameter ( $\lambda^{ep}$ ) calculated in this work using LDA and GGA, respectively, and column 8 lists the data from literature. . . . .	105
7.1 Average phonon and electron properties of Au, Al, Pt, and Si used in the BTE or Fourier calculations. Table reproduced from Ref. [207]. . . . .	122

## LIST OF FIGURES

Figure	Page
1.1 (a) $G_I$ resolved by polarization, i.e., in-plane (xy) and out-of-plane (z), as a function of $T$ . (b) and (c) $G_{I,measured}$ and $G_{I,real}$ as a function of filling fraction. Panels reproduced with permission from: (a) Ref. 10; (b) and (c), Ref. 12. . . . .	4
2.1 Normalized cumulative thermal conductance ( $G$ ) as a function of the reciprocal phonon wavelength, $\lambda^{-1} = k/2\pi$ . Figure reproduced from Ref. [56].	16
2.2 (a) and (b): the $\kappa$ of aGNRs and zGNRs at different $T$ (width = 4 nm) and for different GNR width ( $T = 300$ K). 15 independent simulations are performed to account for the statistical fluctuation of the MD results. The inset shows how aGNR and zGNR are cut from graphene. Figure reproduced from Ref. [56]. . . . .	19
2.3 Cross-sectional heat flux distribution in aGNRs and zGNRs at various temperatures. The inset shows the simulation domain setup for these calculations. Figure reproduced from Ref. [56]. . . . .	19
2.4 (a) and (b): the vDOS and the phonon participation ratio of a bulk graphene, aGNR and zGNR. (c): the spatial distribution ( $\Phi$ ) of modes within $\Gamma = \{\gamma : p_\gamma < 0.4\}$ for aGNR and zGNRs, and $\Gamma = \Gamma_{aGNR} \cup \Gamma_{zGNR}$ for graphene. The height in (c) corresponds to the magnitude of localization at that position (x, y). Figure reproduced from Ref. [56]. . . . .	20
3.1 (a) geometrical definition of the length (L) and width (w) of the trapezoidal-GNRs and T-shaped GNRs; the width ratio of the GNRs is maintained at 3:1; the <i>forward</i> direction is indicated by the arrows. (b) heat current in a trapezoidal-GNR as a function of $ \Delta T $ . (c) temperature profiles in the trapezoidal-GNRs. (d) $\eta$ as a function of the length or width of GNRs. $w = 2$ nm when L varies and $L = 6$ nm when w varies for the T-shaped GNRs, and $L = 2\sqrt{3}w$ for the trapezoidal-GNRs. Figure reproduced from Ref. [92]. . . . .	25

Figure	Page
3.2 Schematic of the structure of an arbitrary shape applied with <i>forward</i> (left) and <i>backward</i> (right) temperature bias. $S_1$ and $S_2$ denote two surfaces maintained at $T_{hot}$ and $T_{cold}$ respectively for the <i>forward</i> direction and reversed for the <i>backward</i> direction. $S_{ins}$ denotes insulating (adiabatic) thermal boundaries. $J_f$ and $J_b$ are the total heat transfer rates, and $\vec{J}''_f(\vec{x})$ and $\vec{J}''_b(\vec{x})$ are the local heat fluxes. Figure reproduced from Ref. [92].	26
3.3 Numerical verification for isotropic $\kappa$ . The inset is the structure used for the numerical calculations. The heat flux, which has $x$ and the $y$ components, is measured along an arbitrary path (from the filled circle to the filled square) as a function of the distance to the starting point. f and b represent <i>forward</i> and <i>backward</i> cases, respectively. Figure reproduced from Ref. [92]. . . . .	29
3.4 Numerical verification for anisotropic $\kappa$ , i.e., $\kappa_{xx} \neq \kappa_{yy}$ . Figure reproduced from Ref. [92]. . . . .	30
3.5 $\kappa$ 's used for the isotropic case in Fig. 3.3 and the anisotropic case in Fig. 3.4. Figure reproduced from Ref. [92]. . . . .	30
3.6 (a) out-of-plane vibrational density of states. (b) $H$ and $\eta$ as a function of $\Delta T$ . Figure reproduced from Ref. [92]. . . . .	32
3.7 (a) participation ratio of bulk graphene and T-shaped GNRs. Spatial distribution of localized modes when heat flows in the direction of (b) decreasing width ( <i>forward</i> ), and (c) increasing width ( <i>backward</i> ). Figure reproduced from Ref. [92]. . . . .	35
3.8 Spring constant spectra of (a): in-plane motion and (b): out-of-plane motion of atoms. Figure reproduced from Ref. [92]. . . . .	36
3.9 Homogeneous nanostructures as potential thermal rectifiers: (a) nano thin films with non-uniform thickness, (b) asymmetric quantum dots, (c) nano thin films with non-uniform width, (d) non-uniform nanowires, and (e) thermal rectifier series as proposed in literature [99], but with atomic smoothness for all edges. Directions of higher $\kappa$ and the value of $\eta$ are indicated. (a)-(d) have diamond lattice while (e) is cut from graphene, and all $\eta$ 's are calculated using the optimized Tersoff potential at $T = 300$ K and $\Delta T = 90$ K. Figure reproduced from Ref. [92]. . . . .	38
3.10 (a) Types of point defect studied in this work. (b) Simulation domain setup for pdGNRs. The dashed line divides the GNR into pristine region and defected region, where defects are randomly created inside the latter. Figure reproduced from Ref. [35]. . . . .	40

Figure	Page
3.11 Temperature dependence of $\eta$ for pdGNRs with different types of point defect. Figure reproduced from Ref. [35]. . . . .	42
3.12 (a) $\eta$ as a function of $L$ of the pdGNRs for different $\Delta T$ . Data points denoted by unfilled and filled markers are computed by MD simulation and by solving the 1D, steady-state Fourier heat conduction equation, respectively. (b) $\eta$ as a function of $\alpha$ for pdGNRs with different $R_L$ . Figure reproduced from Ref. [35]. . . . .	43
3.13 (a) vDOS of the perfect region and defected region for opposite heat flow directions. (b) $H$ and $\eta$ for various $\Delta T$ . Figure reproduced from Ref. [35].	44
4.1 Phonon dispersions along the [100] direction. (a) LJ crystals ( $\epsilon = 16\epsilon_{Ar}$ ) with atomic masses of $m = 40$ g/mol (m40) and $m = 90$ g/mol (m90). (b) A SL built from repetitions of 1 UC thick of m40 layer and 1 UC thick of m90 layer (1UC $\times$ 1UC) along the [100] direction. (c) A 2UC $\times$ 2UC SL.	50
4.2 (a) Schematic of the simulation domain setup in this work. $L_{bath}$ is the length of the heat bath and $L_{tot}$ is the total length of the device. The hot (cold) bath is maintained at $T + \Delta T/2$ ( $T - \Delta T/2$ ). $T_L$ and $T_R$ are the steady-state local temperature at the buffer regions next to the two ends of the device. $J$ is the steady-state heat current. (b) Superlattice made of alternating layers of m40 and m90 with layer thickness $\delta_{m40}$ and $\delta_{m90}$ , respectively. (c) Superlattice of which the UC is a random 4-layer (R4L-SL). (d) Random multilayer (RML). (e) Superlattice with interface mixing (IM-SL). (f) Superlattice with interface roughness (IR-SL). (g) Random multilayer with interface mixing (IM-RML). . . . .	52
4.3 Histogram of $\kappa$ normalized by the corresponding average for 48 individual samples for SLs with 16 layers (16L-SL), RMLs with 16 layers (16L-RML), SLs with 64 layers (64L-SL) and RMLs with 64 layers (64L-RML), of which the average layer thickness $\delta = 4.3$ nm. . . . .	55
4.4 (a) and (b): $G$ of SL, R4L-SL and RML as a function of $L_{tot}$ for LJ04 $\epsilon_{Ar}$ systems (a) and LJ16 $\epsilon_{Ar}$ ones (b), and the solid lines are fitting curves based on Eq. (4.7) and Eq. (4.10). (c) and (d): $\kappa$ of SL, R4L-SL and RML as a function of $L_{tot}$ for LJ04 $\epsilon_{Ar}$ systems (c) and LJ16 $\epsilon_{Ar}$ ones (d), respectively, and the dashed lines are guides for the eyes. For all cases, The average layer thickness $\delta = 4.3$ nm. . . . .	60
4.5 (a) Fitting of simulation data using the two-phonon model depicted by Eqs. 4.7-4.12. (b) Top panel: MFP $\lambda$ of coherent phonons and incoherent phonons in SLs and the localization length $L_{loc}$ of coherent phonons in RMLs; bottom panel: ballistic-limit thermal conductance $G_0$ of coherent phonons and incoherent ones in SLs. . . . .	62



Figure	Page
4.6 (a) and (b): Left Y-axis is for the thermal conductivity of SL, RML and the difference between them as a function of temperature; right Y-axis is for the ratio of MFP to average layer thickness as a function of $T$ . (a) is for $\delta = 1.1$ nm and (b) is for $\delta = 4.3$ nm. (c) and (d): Left Y-axis is for the $\kappa$ of SL, RML and the difference between them as a function of $\delta$ ; right Y-axis is for $\lambda/\delta$ as a function of $T$ . (c) and (d) are for $T = 30$ K and $T = 100$ K, respectively. The solid lines are guides for the eyes. . .	64
4.7 Temperature profiles (left Y-axis) and the thermal boundary resistances of each individual interface (right Y-axis) for: (a) a SL with $\delta = 4.3$ nm and $L_{tot} = 68.4$ nm; (b) a RML with $\delta = 4.3$ nm and $L_{tot} = 68.4$ nm; (c) a SL with $\delta = 4.3$ nm and $L_{tot} = 34.2$ nm; (d) a SL with $\delta = 17.1$ nm and $L_{tot} = 273.5$ nm. The red dashed lines show the diffusive limit of the thermal boundary resistance, i.e., $3.4 \times 10^{-9}$ m <sup>2</sup> K/W. . . . .	67
4.8 (a) Phase-diagram of the thermal conductance contributed by phonons characterized by different length scales, i.e., long-wavelength (lw), short-wavelength (sw), coherent (coh) or incoherent (inc). (b), (c) and (d) are the phase diagrams for RML with perfect interfaces, SL with interface defects and RML with interface defects, respectively. . . . .	70
4.9 (a) Comparison of the thermal conductivity of SL and RMLs with different degree of randomness in layer thickness $\delta$ as a function of the total length. (b) Comparison of the thermal conductivity of perfect SLs and those with different types of interface roughness. (c) Comparison of the thermal conductivity of perfect SLs and those with different degrees of interface mixing. (d) Thermal conductance of SL, RML, IM-SL, IR-SL and IM-RML as a function of the total length. All structures have $\delta = 4.3$ nm, or 8 UC. . . . .	72
5.1 Representative temperature profiles in TTM for a metal-nonmetal interface. $T_n$ , $T_p$ and $T_e$ are temperature profiles for phonons in the nonmetal side, phonons in the metal side and electrons in the metal side. $T_{fit}$ is a linear fit of the temperature profile of the electron-phonon equilibrium region. In the metal side near the interface, electrons and phonons have different temperature, which indicates electron-phonon non-equilibrium. $\Delta T_{ep}$ and $\Delta T_{pp}$ denote the temperature continuity related to the electron-phonon coupling in the metal side and the phonon-phonon coupling across the interface, respectively. $\Delta T = \Delta T_{ep} + \Delta T_{pp}$ is the total temperature jump at the interface. Figure reproduced from Ref. [24]. . . . .	79

Figure	Page	
5.2	Illustration of the coupled electronic and phononic subsystems using FD and MD in TTM-MD simulations. Lines represent FD grids, with solid ones denoting the grid of interest. Dots are atoms in MD simulations, with enlarged ones denoting the atoms inside the FD grid of interest. Thermal transport in the electronic subsystem is modeled by solving Eq. (7.3a) using FD method, where each grid has its own $T_e$ , and $T_p$ is the average temperature of the MD atoms inside this grid. Phononic subsystem is modeled by the MD simulation, with each atom subject to a Langevin force, which equilibrates their temperatures to the $T_e$ of the overlapping FD grid. Figure reproduced from Ref. [24]. . . . .	85
5.3	(a): the simulation setup. (b) and (c): the steady-state temperature profiles obtained in conventional MD and TTM-MD simulations on pure Cu. Electron-phonon non-equilibrium can be seen at and near the thermostat region in (b). Electron and phonon are always in equilibrium in (c) since we use $\kappa_e = 0$ . Figure reproduced from Ref. [24]. . . . .	88
5.4	(a) illustrates the simulation domain setup, where the segments denoted by different colors are fixed end, hot thermostat, Si system, Cu system, cold thermostat and fixed end from left to right. (b) shows the steady-state temperature profiles obtained in conventional MD and TTM-MD simulations on a Si-Cu system. The inset is a zoom-in of $T_e$ and $T_p$ adjacent to the interface. Figure reproduced from Ref. [24]. . . . .	92
5.5	$\kappa_e$ dependence of $R_I$ predicted by TTM-MD simulations. $R_I$ saturates when $\kappa_e > 100$ W/m-K. The data for MD (crosses) are duplicates of the single data obtained from repeated MD simulations at 300 K. Figure reproduced from Ref. [24]. . . . .	94
5.6	$R_I$ calculated from MD and TTM-MD simulations for Si-Cu interface. $g_{ep,1} = 2.6 \times 10^{17}$ W/m <sup>3</sup> -K, and $g_{ep,2} = 5.5 \times 10^{16}$ W/m <sup>3</sup> -K. $c_e(T)$ means the use of temperature dependent volumetric heat capacity $C_e (= 96.8 \text{ J/m}^3\text{-K}^2 \times T_e)$ in TTM-MD simulation. Figure reproduced from Ref. [24]. . . . .	95
5.7	(a): perspective view (front) of the CNT-Cu interface; (b): schematic of the definition of the cross-sectional area of the Cu substrate ( $A_s$ ) and the contact ( $A_c$ ) in Eq. (5.23). Figure reproduced from Ref. [24]. . . . .	96
5.8	$R_I$ calculated from MD and TTM-MD simulations for the CNT-Cu interface, where $A_c/A_s = 1.0\%$ is used. Figure reproduced from Ref. [24]. . . . .	97

Figure	Page
6.1 Results for Cu. (a) Electronic density of states as well as the Fermi window at 300 K and 1,000 K. All data in this panel and below are obtained under the GGA approximation otherwise mentioned. The inset shows the phonon dispersion relations calculated in this work as well as experimental data. [195] (b) and (c) Contour plot of the p-p and p-e scattering rates in the $k_x$ - $k_y$ plane of the FBZ. (d) Lattice thermal conductivity computed from first-principles with the LDA and GGA approximations with and without the effect of p-e scattering. The inset shows $\kappa_L$ when only p-e scattering is considered. Figure reproduced from Ref. [196]. . . . .	107
6.2 Results for Ag. (a) Electronic density of states as well as the Fermi window at 300 K and 1,000 K. All calculations are obtained under the LDA approximation otherwise mentioned. The inset shows the phonon dispersion relations in the $\Gamma$ - $X$ direction in the FBZ calculated in this work as well as experimental data. [197] (b) and (c) Contour plot of $\gamma^{pp}$ and $\gamma^{pe}$ in the $k_x$ - $k_y$ plane of the FBZ of Ag. (d) $\kappa_L$ with and without the effect of electron-phonon scattering. The inset shows $\kappa_L$ when only p-e scattering is considered. Figure reproduced from Ref. [196]. . . . .	108
6.3 Results for Au. (a) Electronic density of states as well as the Fermi window at 300 K and 1,000 K. All calculations are obtained under the LDA approximation otherwise mentioned. The inset shows the phonon dispersion relations calculated in this work as well as experimental data. [198] (b) and (c) Contour plot of $\gamma^{pp}$ and $\gamma^{pe}$ in the $k_x$ - $k_y$ plane of the FBZ. (d) $\kappa_L$ with and without the effect of electron-phonon scattering. The inset shows $\kappa_L$ when only p-e scattering is considered. Figure reproduced from Ref. [196]. . . . .	110
6.4 Results for Pt. (a) Electronic density of states as well as the Fermi window at 300 K and 1,000 K. All calculations are obtained under the LDA approximation otherwise mentioned. The inset shows the phonon dispersion relations calculated in this work as well as experimental data (dark symbols). [201] (b) and (c) Contour plot of $\gamma^{pp}$ and $\gamma^{pe}$ in the $k_x$ - $k_y$ plane of the FBZ. (d) $\kappa_L$ with and without the effect of electron-phonon scattering. The inset at the upper left corner shows $\kappa_L$ when only p-e scattering is considered, and the inset at the upper right corner shows the cumulative thermal conductivity with respect to phonon mean-free-path at 300 K. Figure reproduced from Ref. [196]. . . . .	111

Figure	Page
6.5 Results for Ni. (a) Electronic density of states as well as the Fermi window at 300 K and 1,000 K. All calculations are obtained under the GGA approximation otherwise mentioned. The inset shows the phonon dispersion relations calculated in this work as well as experimental data (dark symbols). [202] (b) and (c) Contour plot of $\gamma^{pp}$ and $\gamma^{pe}$ in the $k_x$ - $k_y$ plane of the FBZ. (d) $\kappa_L$ considering p-e scattering only, p-p scattering only, and both p-e and p-p scattering. The inset shows the cumulative thermal conductivity with respect to phonon mean-free-path at 300 K. Figure reproduced from Ref. [196]. . . . .	114
6.6 Results for Al. (a) Electronic density of states as well as the Fermi window at 300 K and 1,000 K. All calculations are obtained under the GGA approximation otherwise mentioned. The inset shows the phonon dispersion relations calculated in this work as well as experimental data (dark symbols). [203] (b) and (c) Contour plot of $\gamma^{pp}$ and $\gamma^{pe}$ in the $k_x$ - $k_y$ plane of the FBZ. (d) $\kappa_L$ with and without the effect of electron-phonon scattering. The inset shows $\kappa_L$ when only p-e scattering is considered. Figure reproduced from Ref. [196]. . . . .	115
7.1 (a) The vibrational density of states of Au, Al, Pt, and Si. (b) The interfacial thermal resistance, electronic ( $R_{ee}$ ) or phononic ( $R_{pp}$ ), for various interfaces. Figure reproduced from Ref. [207]. . . . .	124
7.2 (a) Schematic illustration of the simulated Au-Si and Au-interlayer-Si systems. (b) The ratio of the effective interfacial thermal resistance, $R_{\text{eff}}$ , to the original interfacial thermal resistance, $R_{\text{original}}$ , as a function of interlayer thickness. (c) and (d) Temperature profiles of electron and phonon obtained in the simulation. Figure reproduced from Ref. [207]. . . . .	126
7.3 (a) Heat transfer channels in Au-Si without an interlayer. (I) and (II) denote lattice heat transfer channels, with (I) denoting electron-phonon coupling while (II) denoting phonon transmission into the substrate. (b) Heat transfer channels in Au-Si with an interlayer. (I) denotes the same process as that in (a), while (III) denotes backflow of heat from the hotter interlayer lattice to the Au lattice. The heat flow direction indicated by the dashed arrow is also possible, for example, when $G_{ep}$ of the interlayer is lower than that of Au. (c) Transient electron temperature at the surface of a Au thin film for different interlayer thickness, $G_{ee}$ between Au film and interlayer, and interlayer material. Figure reproduced from Ref. [207]. . . . .	128

Figure	Page
7.4 (a) Lattice temperature rise of the Au film as a function of time for different interlayer thickness or $G_{ee}$ . A laser fluence of $20 \text{ J/m}^2$ is used for all cases. The heating or cooling of the Au lattice is dominated by different mechanisms at different stages: (I) heat transfer from hot electrons; (II) heat dissipation into the substrate; (III) backflow of heat from the hotter interlayer lattice. (b) Lattice temperature rise of the interlayer as a function of time. Figure reproduced from Ref. [207]. . . . .	130
8.1 Flowchart of our Monte Carlo simulation of electron-phonon coupled thermal transport. . . . .	137
8.2 Illustration of the simulated Au/Si structure. . . . .	139
8.3 Simulation results for a Au/Si system under ultrafast laser radiation. (a) average temperature of electron, LA phonon, and TA phonon as a function of time. The dark line is an exponential fit of the temperature of electrons in the thin film. (b)-(d) temperature profiles at different time instants after the laser radiation. . . . .	141

## ABSTRACT

Wang, Yan Ph.D., Purdue University, August 2016. Multiscale Simulations of Thermal Transport in Graphene-based Materials and across Metal-semiconductor Interfaces. Major Professor: Xiulin Ruan, School of Mechanical Engineering.

The rapid advance in modern electronics and photonics is pushing device design to the micro- and nano-scale, and the resulting high power density imposes immense challenges to thermal management. When device size shrinks to the same order of or even below the wavelength or mean-free-path of heat carriers, the transport of heat carriers and the interaction between them will differ from those in the macroscopic regime. This imposes challenges on designing micro/nano-devices with required thermal performance, while, at the same time, also opens the door for designing novel materials and structures with promising thermal properties.

This research explores structures with unique heat transfer properties for thermal management applications. It also seeks to build a more accurate and comprehensive understanding of electron and phonon transport, and the coupling between them, in order to guide the design of strategies to enhance heat dissipation in solid-state devices. Graphene is a unique material with 2D lattice structure and single-atomic-layer thickness, and we explore several mechanisms that can affect thermal transport in it. The thermal conductivity ( $\kappa$ ) of zigzag-edged graphene nanoribbons (GNRs) is found to be higher than that of armchair-edge ones in our molecular dynamics (MD) simulations, and phonon localization at edges is attributed to underlie such edge-chirality dependence. Thermal rectification (TR) is a phenomenon in which heat flows more easily in one direction than in the opposite direction, which is particularly useful for thermal management. Using MD simulations, we find significant TR in asymmetrically defected GNRs and pristine GNRs with asymmetric geometry. However, TR in these two structures arises from different mechanisms. In the former case, GNRs are

pristine on one side while defective on the other, and TR is caused by the different temperature dependence of the thermal conductivity of the two sides. In the latter case, TR can be enabled by phonon lateral confinement when the width of the GNR is smaller than the phonon mean free path. These findings will provide useful guidance to the fabrication of thermal rectifiers from pristine materials including but not limited to graphene.

A two-temperature non-equilibrium MD simulation technique is developed to atomistically model electron-phonon coupled thermal transport across metal/semiconductor interfaces. On the metal side, the lattice part of thermal transport is modeled with MD while the electronic part is simultaneously modeled with the Fourier’s law using the finite difference method. On the semiconductor side, electrons are neglected and only phonons are considered. Our method naturally accounts for the effect of defects, interface, temperature, etc., on thermal properties of phonons and also includes the coupling between electron and phonon. We use this technique to compute the thermal boundary resistance (TBR) of Si/Cu and CNT/Cu interfaces. In a region within a “cooling length” distance to the interface, electron and phonon are revealed to be in thermal non-equilibrium, which considerably impedes heat transfer across the interface. The TBR of CNT/Cu interfaces predicted using our method is in better agreement with experimental results than conventional MD methods.

A two-temperature Boltzmann transport equation method is also built, which considers electron and phonon on both sides of the interface. It was reported that an interlayer with intermediate phonon spectra between two dielectric materials could reduce the phononic interfacial thermal resistance. In this work, we show that an appropriate choice of interlayer materials with relatively strong electron-phonon coupling could significantly enhance interfacial thermal transport across metal-dielectric interfaces. Our Boltzmann transport simulations demonstrate that such enhancement is achieved by the elimination of electron-phonon nonequilibrium near the original metal-dielectric interface. Moreover, we reveal that interlayer can substantially accelerate hot electron cooling in thin films with weak electron-phonon coupling, for

example, Cu, Ag, and Au, supported on a dielectric substrate. At the same time, lattice heating in the thin film is largely reduced.

A Monte-Carlo simulation approach is proposed to solve electron-phonon coupled thermal transport problems in metal-semiconductor heterojunctions. This approach enables us to conduct a spectral electron-phonon simulation considering the selection rules for three-phonon scatterings. We demonstrate the approach using a Au-Si bilayer system under ultrafast laser radiation. Nonequilibrium between electrons and different phonon modes are observed. This approach enables first-principles-based simulation of heat transfer across metal-nonmetal interfaces, which will be useful for designing thermoelectric devices and for thermal management of electronic devices.

The results from this study offer new understandings of nanoscale thermal transport involving multiple types of heat carriers, and the approaches developed have strong predictive capability, which will aid the thermal design of novel micro- or nano-devices. This research also provides new perspectives of atomic- and nano-scale engineering of materials and structures to enhance efficiency of thermal management.



## 1. INTRODUCTION

With the rapid advance in nanotechnology, the size of modern electronic and photonic devices have shrunk to the nanoscale and the resulting high power density starts to impose immense challenges on thermal management. It was recently reported that the Moore's law, which has governed the advancement of semiconductor industry since the 1960s, will end soon. [1] The clock rate, which determines how fast microprocessors execute instructions, has stopped increasing since 2004. The reason is that heat dissipation, which increases as the clock rate increases, has become a fundamental problem limiting further downscaling of chip feature size. In nano-sized devices, the interfacial thermal resistance between different components is usually the bottleneck for heat dissipation. Understanding the mechanism of interfacial thermal transport across various dissimilar materials is thus of fundamental importance to the thermal management of electronic devices and the development of thermal interface materials. Moreover, in electronic devices, multiple types of energy carriers such as electrons and phonons are usually involved. When device size shrinks to the same order of or even below the wavelength or the mean-free-path of heat carriers, the carrier transport and interaction will differ from those in the macroscopic regime, of which the effect on thermal transport is not fully understood. This imposes challenges to thermal design using conventional methods based on the Fourier's law, which cannot model ballistic or ballistic-diffusive thermal transport accurately. On the other hand, it opens the door for designing novel structures with promising thermal properties.

### 1.1 Thermal Issues in Electronic Devices

The aggressive decrease in the size of electronic and photonic devices and the fast increase in their operating frequencies have resulted in extremely high power density,

which is detrimental to the performance, reliability, and lifetime of devices. [2] For example, the silicon-nanowire-based field effect transistor reported in Ref. [3] has a cross-sectional area of  $23 \times 80 \text{ nm}^2$ . [3] In this transistor, an electrical bias generates an electric field that accelerates electrons, which will then scatter with phonons and lose their energy to the lattice. Correspondingly, the lattice, especially that near the drain, will be heated to a higher temperature and thereby reducing the mobility of electrons. Moreover, electron energy is preferably injected into optical phonons rather than acoustic phonons in the Joule heating process. However, optical phonons, in most cases, are less effective in transferring heat than acoustic ones. As a consequence, heat has to be transferred to acoustic phonons first and be dissipated away thereafter. [2] Moreover, the size of the cross-section of the silicon nanowire is smaller than the mean-free-path of many phonon modes in silicon. In this case, phonon transport in the lateral directions is mostly in the ballistic regime and conventional heat diffusion theory based on the Fourier's law is no longer valid.

In the transducer of heat-assisted magnetic recording (HAMR) devices, surface plasmon polaritons are first excited by a laser and then propagate towards the tip. During the above process, the electromagnetic field is amplified by several orders of magnitude, which creates intense local heating to the disk medium and thereby writing a "bit" to the disk. The physical size of a "bit" in the hard disk can be around  $25 \times 150 \text{ nm}^2$  [4] and the I/O speed is limited by how fast the "bit" can be heated or cooled to the threshold temperature. Therefore, thermal design is essential to the performance of this device and a comprehensive understanding of carrier transport and interaction in nanosized structures is important.

Moreover, in micro- and nano-devices, the stacking of metal, semiconductor, and insulator is inevitable and the interface between different components is usually the bottleneck for heat dissipation. Rigorous predictive simulation approaches and schemes that can enhance thermal transport across interfaces are urgently needed for thermal management of modern devices.

## 1.2 Thermal Transport in Graphene

Graphene has been recognized as a potential substitute for silicon in the electronics industry mainly owing to its outstanding electronic properties [5]. The tunable band-gap opening and edge-chirality dependent electronic property of graphene nanoribbon (GNR), a narrow strip of graphene, makes the vast application of graphene-based devices even more promising [5, 6]. The high thermal conductivity ( $\kappa$ ) of graphene and GNR renders them intrinsically advantageous over silicon-based devices in terms of heat dissipation. [7–9] In some applications, graphene is an active component of the device, e.g. graphene transistors. In other cases, graphene is used as a thermal interface material to fill the air gaps at interfaces. In both scenarios, a high  $\kappa$  and low interfacial thermal resistance ( $R_I$ ) are desired. Graphene may be vertically (end-contact) or horizontally (side-contact) aligned with the substrate depending on the application, and the heat transfer mechanism should be different due to the different ways of phonon-phonon coupling across the interface.

### 1.2.1 Horizontal Alignment of Graphene on Substrate

For thermal transport across graphene/dielectric interface, Ong et al. [10] studied the thermal transport across graphene/silica interface with Green-Kubo molecular dynamics simulations and the nonequilibrium Green’s function (NEGF) method, where the coupling between graphene phonons and substrate surface phonons was believed to be the dominant mechanism for interfacial thermal transport. As shown in Fig. 1.1a, NEGF calculation suggests that most of the heat transfer is aided by out-of-plane phonons in graphene, while in-plane ones are much less effective in transporting energy across the interface. Ong et al. also conducted spectral energy density (SED) analysis for graphene, which showed that ZA phonons with moderate wave vectors couples with the substrate most strongly. They attributed such behavior to flexural resonance as described by Persson and Ueba [11], who proposed that  $G_I$  should be

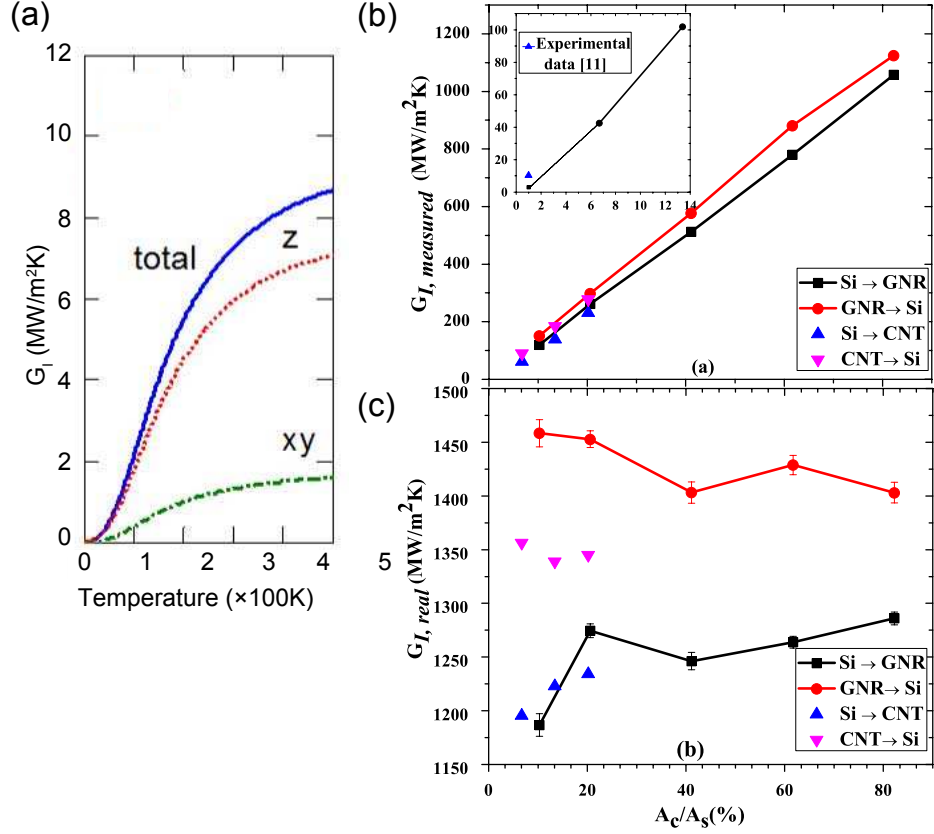


Figure 1.1. (a)  $G_I$  resolved by polarization, i.e., in-plane (xy) and out-of-plane (z), as a function of  $T$ . (b) and (c)  $G_{I,measured}$  and  $G_{I,real}$  as a function of filling fraction. Panels reproduced with permission from: (a) Ref. 10; (b) and (c), Ref. 12.

dominated by the coupling between the flexural mode in graphene and the Rayleigh mode at the substrate surface.

As for graphene/metal interfaces, density-functional theory (DFT) calculations have revealed that the bonding between graphene and various metals can be categorized into two types — chemisorption and physisorption — of which the former is characterized by strong bonding which opens a band gap in graphene while the latter is weak that the Dirac-cone energy band of graphene is preserved [13]. Mao et al. calculated  $R_I$  of the side-contact interface between graphene and different metals (Ni, Cu, Au, Pd) using the first-principles NEGF method [14]. The room-temperature  $R_I$

of those interfaces was found to vary by one order of magnitude, but not monotonically decrease with increasing interfacial bonding strength.

### 1.2.2 Vertical Alignment of Graphene on Substrate

For vertical graphene on substrates, the computationally predicted  $R_I$  is usually orders of magnitude lower than experimental data, and the incomplete filling of graphene or CNT at the interface was believed to account for most of the discrepancies [15, 16]. A parameter, which is often referred to as filling fraction or volume fraction, is defined as the ratio of the contact area to the surface area of the substrate. The contact area is  $w\delta$  and  $\pi d\delta$  for graphene and CNT in end-contact with substrate, respectively. The real  $G_I$  is usually computed from the measured values by  $G_{I,real} = G_{I,measured}/\text{filling fraction}$ , but it is not known whether such linear dependence still holds when there is considerable interlayer coupling between graphene flakes at high filling fractions. Vallabhaneni et al. [12] used NEMD simulations to study the filling fraction dependence of  $G_I$  for graphene/Si interfaces. The Tersoff potential for covalent C-Si bonding was used in their simulations.  $G_{I,real}$  was found to increase linearly with the filling fraction, indicating a negligible effect of interlayer coupling on  $G_I$ . They also computed the effective  $G_I$  considering the highest possible filling fraction for graphene in end-contact with Si, and the values are in the range of 0.2-1.2 GW/m<sup>2</sup>-K, which are still orders of magnitude higher than experimental values [15–17], suggesting much room for improvement in graphene and CNT based thermal management solely by increasing the filling fraction.

In graphene-based nanocomposites, graphene flakes are embedded in an organic matrix so that both the horizontal and vertical alignment of graphene exist in such structures. Graphene flakes may improve the alignment of organic molecules adjacent to their surfaces, which can affect the organic phase thermal conductivity. In addition, the edges of graphene flakes are usually passivated with hydrogen or oxygen atoms and such edge passivation was shown to affect the thermal conductance between

graphene flakes [18]. Hu et al. studied graphene embedded in organic matrix with MD simulations and observed that graphene can enhance the  $\kappa$  of nanocomposites significantly [19, 20].

### 1.2.3 3D Architectures

Pillared graphene architectures (PGA) [21, 22] have been proposed for thermal management applications, where the PGA is built in such a way that phonons can transport easily in the two dimensions of the graphene plane, and can also readily propagate in the third dimension which is parallel to the vertically aligned CNTs. This design may be a solution to the practical problem of using graphene and CNT as TIMs, i.e., the very low  $\kappa$  in the directions perpendicular to the graphene plane or CNT axis, which could seriously degrade heat dissipation performance when they are misaligned. Varshney et al. claimed that phonon scatterings at the CNT/graphene junctions dominate the overall thermal resistance of PGA based on NEMD simulations [21], and phonon transmission across individual CNT/graphene junction was modeled with the phonon WP method by Lee et al. [22].

### 1.2.4 Beyond Phonon-phonon Coupling

In the above, the interfacial thermal transport is contributed solely by phonon-phonon coupling across the interface between graphene and other materials. It should be noted that thermal transport across the interface between graphene and metals not only depends on phonon properties, but also on electron properties as well as electron-phonon coupling [23, 24]. Besides, surface phonon-polariton scattering has also been revealed to account for a significant part of heat dissipation from graphene to polar substrates, e.g.,  $\text{SiO}_2$  and hexagonal boron nitride (h-BN) [25]. Rigorous atomistic modeling of the above processes would benefit the thermal management of graphene-based devices but it is still lacking.

### 1.3 Thermal Rectification

Thermal rectification (TR) is a phenomenon in which heat flow is directional dependent, i.e., heat current changes in magnitude as the temperature bias is reversed. A dimensionless parameter, thermal rectification ratio ( $\eta$ ), is usually used to quantify TR, which is defined as

$$\eta = \frac{\kappa_{forward} - \kappa_{reverse}}{\kappa_{reverse}} \times 100\%, \quad (1.1)$$

where the subscripts *forward* and *reverse* denote the two opposite directions pointing from one end to the other. TR is a thermal analogue of the electrical diode where the current carrying ability of the device under forward bias is much higher than under reverse bias. A perfect thermal rectifier would be one that is highly thermal conductive in one direction while insulating in the other, and it is expected to work as a promising thermal management component of electronics as chip size continues decreasing or as a basic component for thermal computing [26].

Although the earliest proposal of TR in bulk 3D materials dates back to 1930s [27], only since the middle of the last decade has extensive attention been paid to CNT and graphene based systems [9, 12, 28–35]. To date, proposed thermal rectifiers include physically/chemically functionalized GNRs and CNTs, or heterojunctions composed of GNR/CNT and other materials. In all the existing designs, a spatial asymmetry in geometry, defect concentration, isotope concentration, or an interface between two materials is necessary for TR to occur, and  $\eta$  can be tuned by adjusting the magnitude of such asymmetries [29–31]. Many other factors were also found to affect  $\eta$ , for instance, high  $T$  usually reduces  $\eta$ , high  $\Delta T$  enhances  $\eta$ , while  $\eta$  decreases with the length of the system to zero in the bulk limit [35], or saturates when the length increases [31].

Despite that many schemes are possible to be applied to make thermal rectifiers, the fact that  $\eta$  can be reduced by the presence of lattice disorders such as edge roughness [36] and defects [35, 36] may make it difficult for the observation of significant TR

experimentally, considering that  $\eta$  may not be high enough to prevail measurement uncertainties.

## 1.4 Numerical Methods for Thermal Transport

In this section, we review a few numerical methods for modeling thermal transport in solids, in particular, classical molecular dynamics (MD) simulations, the nonequilibrium Green's function (NEGF) method, and Boltzmann transport equation (BTE) methods in conjunction with phonon properties predicted via other tools, e.g., density functional perturbation theory. These methods can either capture the thermal transport behavior from all phonon modes as a whole, or track the contribution from a single phonon mode based on its relaxation time, mean-free-path (MFP) and velocity. They are appropriate for different phonon transport regimes or aspects, since they deal with phonons in different manners, such as wave vs particle nature, time vs frequency domain, different thermodynamic conditions, and different boundary conditions (BC).

### 1.4.1 Classical Molecular Dynamics Simulations

Classical MD simulations model the movements of atoms based on the Newton's second law of motion and a knowledge of the interatomic potentials. They can directly model phonon thermal transport and naturally account for atomic details of the structure such as defects, interface, strain, surface reconstruction, etc., which can provide atomic-level insights to thermal transport. Several MD schemes have been used for modeling heat transfer, for instance, non-equilibrium MD (NEMD) [37], reverse NEMD (RNEMD) [38], equilibrium MD (EMD) [37], thermal relaxation method [19], wave-packet (WP) method [39], and phonon normal mode analysis (NMA) [40, 41]. The accuracy of MD is limited by the quality of empirical interatomic potentials (EIP), and this has stimulated the invention of first-principles MD [42], which has also been applied to thermal modeling recently [43–45]. The heat capacity in classical



MD is the classical Dulong-Petit limit, i.e.,  $C_p = 3N_A k_B$ , which deviates from the quantum  $C_p$  at temperatures below the Debye temperature  $\Theta_D$ . This is a drawback for high  $\Theta_D$  materials like graphene [46].

**Non-equilibrium and reverse non-equilibrium molecular dynamics** NEMD and RNEMD methods [37,38] are commonly used methods in computing the  $\kappa$  of materials. A constant temperature gradient  $\nabla T$  is imposed across the simulation cell to generate a constant heat current  $J$  in the NEMD simulations, and vice versa for RNEMD. Based on the Fourier's law,  $\kappa$  can be computed as  $\kappa = J/(\nabla T \cdot A)$ , where  $A$  is the cross-sectional area of the simulated cell. In either NEMD or RNEMD,  $\nabla T$  or  $J$  has to be maintained by two thermostats. The scattering of phonons by boundaries or thermostats should limit the phonon MFP  $\lambda$  as

$$\lambda^{-1} = \lambda_{\infty}^{-1} + L^{-1}, \quad (1.2)$$

where  $\lambda_{\infty}$  is the intrinsic phonon MFP in the bulk limit and  $L$  was taken as the distance between thermostats in Ref.37. Such size effect is significant for graphene, whose  $\kappa$  has a large contribution from phonons with long  $\lambda$ . An extrapolation method [37,47] based on Eq. (1.2) has been recommended to compute the  $\kappa$  in the bulk limit, i.e., extrapolating the  $\kappa$ 's of several simulation cells of different length to infinite length. These methods are conceptually simple and easy to implement into MD simulations, and reasonable agreement with experiment can be achieved despite the unphysically large temperature gradient across the nanosized simulation domain [37]. A convergence study can be performed to ensure that the system is in the linear response regime where  $\kappa$  does not depend on  $\nabla T$ . It should be noted that the use of Eq. (1.2) implicitly assumes that a finite bulk-limit  $\lambda$  and hence  $\kappa$  must exist, which may not be the case for certain low-dimensional systems of which the  $\kappa$  diverges with length [48–50]. As NEMD and RNEMD are essentially the same despite the reversed cause-and-effect relation between  $J$  and  $\nabla T$ , we will refer to both of them as NEMD in this review.

**Green-Kubo method** The Green-Kubo method is commonly employed in EMD (we will refer to this method as GK-MD), which uses the heat current fluctuations to

calculate  $\kappa$  based on the fluctuation-dissipation theorem [37, 51, 52]. Specifically,  $\kappa$  in the  $x$  direction can be computed as [51]

$$\kappa_x = \frac{1}{k_B V T^2} \int_0^\infty \langle J_x(t) J_x(0) \rangle dt, \quad (1.3)$$

where  $k_B$ ,  $V$ ,  $t$  and  $J_x$  denote the Boltzmann constant, volume of the simulation cell, time and the heat current in the  $x$  direction.  $\langle J_x(t) J_x(0) \rangle$  is the heat current autocorrelation function (HCACF). We present the above formulation of the Green-Kubo method instead of the more frequently cited, isotropic one [37] because graphene, GNR and CNT are anisotropic and hence Eq. (1.3) causes less confusion for the application to these materials. Besides evaluating  $\kappa$  from the direct integral of the HCACF using Eq. (1.3), the HCACF can also be fitted to an exponential decay curve first and then integrated [53]. So far, single [53], double [52] and triple [54] exponential fitting to the HCACF have been used to achieve acceptable fitting qualities. The finite size of the supercells used in EMD simulations can affect  $\kappa$  in GK-MD [55], and Ref. 56 also found that sufficiently long autocorrelation length is needed to accurately predict the  $\kappa$  of GNRs. Therefore, a convergence study on supercell size and autocorrelation length is needed.

**Phonon wave-packet method** The phonon WP method is a straightforward way to capture the dynamic propagation and scattering of phonons by boundary, interface, defect, etc. At the beginning of the simulation, the atoms are displaced from their equilibrium positions according to a formula [39] which corresponds to a wave packet centered at a specific phonon mode  $(k, \omega)$  of the material and standing at a specific position. Then the wave packet propagates towards the scatter at the group velocity of the corresponding phonon mode. By computing the total energy of the wave packet before and after its collision with the scattering center, the transmission coefficient can be evaluated. One limitation of the WP method is that it cannot capture anharmonic phonon scatterings due to the  $\sim 0$ K simulation environment.

**Normal mode analysis** Similar to GK-MD, NMA is also used in EMD simulations. Based on the relaxation time approximation (RTA), NMA can be used to compute  $\kappa$  using the extracted phonon dispersion and spectral phonon relaxation time

$\tau(k, \omega)$  [57]. The prediction of  $\tau$  in NMA can be achieved in both time domain [40, 58] by computing the decay rate of spectral energy and frequency domain [59] by calculating the linewidth of spectral energy, of which the latter is the so-called spectral energy density (SED) analysis. Using the predicted mode-wise  $\tau$  and  $v_g$  (from the phonon dispersion) for each phonon mode  $(k, \nu)$ , where  $\nu$  denotes the index of phonon branches,  $\kappa$  can be evaluated under the RTA as

$$\kappa_x = \sum_k \sum_\nu c(k, \nu) v_{g,x}^2(k, \nu) \tau(k, \nu), \quad (1.4)$$

where the subscript  $x$  indicates the longitudinal direction. An advantage of this method over NEMD and GK-MD is that the spectral  $v_g$ ,  $\tau$ , and  $\lambda$  can be computed, which gives more details of phonons.

#### 1.4.2 Nonequilibrium Green's Function Method

Similar to the phonon WP method discussed above, the NEGF approach, sometimes referred to as atomistic Green's function, also deals with the transmission of phonons. Unlike classical MD simulations, NEGF is valid at sub- $\Theta_D$  temperatures due to the quantum treatment of phonon distribution using the Bose-Einstein statistics. In NEGF, the transmission function  $\Xi(\omega)$  across the system can be computed based on the Green's functions built from the interatomic force constants of the system. Details about the phonon NEGF approach can be found in Refs. 60 and 61. The heat flux and hence the thermal conductance can be computed using  $\Xi(\omega)$  via the Landauer formula [60] as

$$J = \int \frac{\hbar\omega}{2\pi} \Xi(\omega) [n_1(\omega, T_1) - n_2(\omega, T_2)] d\omega, \quad (1.5)$$

and

$$G = \left| \frac{1}{T_1 - T_2} \int \frac{\hbar\omega}{2\pi} \Xi(\omega) [n_1(\omega, T_1) - n_2(\omega, T_2)] d\omega \right|, \quad (1.6)$$

where  $n_1$  and  $n_2$  are the phonon occupation number of the two leads, which are at  $T_1$  and  $T_2$ , respectively. This method can be referred to as “first-principles” if

the force constants are extracted from density-functional theory (DFT) calculations. Force constants predicted from tight-binding calculations were also used in NEGF calculations [62]. For large systems containing hundreds of atoms or more, first-principles calculations of the force constant matrix is computationally forbidden, so the EIPs as those adopted by classical MD simulations have been used [63]. So far in most NEGF studies only the harmonic force constants are used, limiting the credibility of such approach to low temperatures at which the anharmonic phonon-phonon scattering is insignificant. Recently, anharmonic atomistic Green's function calculation has also been attempted [64].

### 1.4.3 Boltzmann Transport Equation

Based on the perturbation theory, the phonon BTE for a phonon mode  $i$  under a temperature gradient  $\vec{\nabla}T$  is given as [51, 65]

$$-v_{g,i} \cdot \vec{\nabla}T \frac{\partial n_i}{\partial T} + \left( \frac{\partial n_i}{\partial t} \right)_{collision} = 0, \quad (1.7)$$

which describes the balance of phonon population  $n$  (occupation number) between the diffusive drift (first term) and collision (second term, also referred to as scattering) of phonons. Several techniques for thermal transport modeling based on Eq. (1.7) have been developed [65, 66]. The most widely used are those based on the single-mode relaxation time approximation (SMRTA), where every mode is assigned a relaxation time ( $\tau_i$ ) accounting for the net effect of different scattering mechanisms, i.e., the collision term in Eq. (1.7) is approximated as

$$\left( \frac{\partial n_i}{\partial t} \right)_{collision} = \frac{n_{i,o} - n_i}{\tau_i}, \quad (1.8)$$

where  $n_{i,o}$  is the occupation number of phonon mode  $i$  under thermal equilibrium, i.e., the Bose-Einstein distribution. The relaxation time  $\tau$  is the time constant for a phonon mode to return to its equilibrium occupation from a nonequilibrium one. SMRTA is only a first-order approximation to the phonon BTE, which neglects the deviation of  $\tau$  from equilibrium values when the system is in non-equilibrium states.

Beyond the SMRTA, Omini and Sparavigna [66] developed an iterative scheme that can solve the linearized Boltzmann equation accurately, which has been adopted by Broido and coworkers on phonon thermal transport in various solids, including graphene and CNTs, in the past few years [67, 68]. This method takes into account the modification to  $\tau$  due to non-equilibrium population of all the phonons undergoing various scattering processes, so it does not suffer from the limitations of the SMRTA. For high- $\kappa$  materials such as graphene and CNTs, the relaxation time of the Umklapp (U) process is strongly modified owing to the shift of equilibrium phonon population by the strong normal (N) process. As a result, the iterative scheme is more accurate than SMRTA, especially for high- $\kappa$  materials with strong N process [69].

It is beneficial to make a comparison between this iterative BTE method with the NMA method discussed in Section 1.4.1 as both methods deal with phonon scatterings spectrally. On one hand, the iterative BTE method is advantageous over the NMA method in that the former gives an accurate solution to the linearized phonon BTE while the latter computes  $\kappa$  based on SMRTA. In addition,  $\tau$  computed from NMA contains contributions from both N and U processes, so directly using the as-predicted  $\tau$  tends to underestimate  $\kappa$  because only the U process directly contributes to thermal resistance. On the other hand, NMA has the advantage that it can capture the lattice anharmonicity to all orders, while the iterative BTE method is usually limited to first-order anharmonicity. Lindsay et al. have suggested that the neglect of higher-order anharmonicities could result in inaccurate prediction of the length-dependence of  $\kappa$  in SWCNTs [69].

## 1.5 Objective

This research explores structures with unique heat transfer properties for thermal management applications. It also seeks to build a more accurate and comprehensive understanding of electron, phonon transport, and the coupling between them, in order to guide the design of strategies to enhance heat dissipation in solid-state devices.

## 1.6 Organization of this thesis

This thesis is organized as follows. In Chapter 2, we study the thermal conductivity of graphene and graphene nanoribbons. In Chapter 3, we investigate the thermal rectification phenomenon in graphene and graphene nanoribbon, and strive to generalize the idea to a broader class of nanostructures. Chapter 4 is on thermal transport in superlattices and random multilayers, in which we investigate coherent and incoherent phonon transport in multi-layered structures and their promise as thermoelectric materials for active on-chip thermal management. In Chapter 5, we introduce a two-temperature nonequilibrium molecular dynamics method to investigate electron-phonon coupled thermal transport across metal-nonmetal interfaces. Chapter 6 deals with first-principles evaluation of phonon-phonon and phonon-electron scattering rate, which allows us to compute the lattice thermal conductivity of materials. In Chapter 7, we introduce a 1D electron-phonon coupled Boltzmann transport equation method and use it to investigate the effect of metallic interlayer on thermal transport across Au/Si interface and on hot electron cooling dynamics in Au thin films. In Chapter 8, we describe a Monte Carlo method to solve 3D electron-phonon coupled Boltzmann transport equations. Finally, we conclude this work in Chapter 9.

## 2. THERMAL CONDUCTIVITY OF GRAPHENE NANORIBBONS

### 2.1 Introduction

Graphene has been recognized as a potential substitute for silicon in the electronics industry, mainly owing to its outstanding electronic and thermal properties [5, 7–9]. The tunable band-gap opening and edge-chirality dependent electronic property of graphene nanoribbon (GNR), a narrow strip of graphene, makes the vast application of graphene-based devices even more promising [5, 6]. GNR has also been predicted to have edge-chirality dependent thermal conductivity ( $\kappa$ ), which was mostly predicted to be higher in zigzag-edged GNRs (zGNR) than armchair-edged ones (aGNR), i.e.,  $\Delta\kappa = \kappa_{zGNR} - \kappa_{aGNR} > 0$ , though the underlying mechanism remains to be an open question [9, 70–73].

The notable difference between the topology of zigzag and armchair edges can lead people to attribute  $\Delta\kappa$  to the surface/edge roughness scattering as usually seen in nanostructures [73–75]. As for thermal transport, the consideration of the surface/edge roughness scattering is usually meaningful only when the RMS height of the surface/edge variation ( $\delta$ ) is comparable to the dominant phonon wavelength ( $\lambda_{dom}$ ) for carrying heat. For narrow GNRs, the thermal conductance ( $G$ ) can be estimated by integrating the Landauer formula over the entire first Brillouin zone (FBZ) as,

$$G(T) = \int_{FBZ} \frac{v_g(k)}{2\pi} \Xi(k) \hbar \omega(k) \frac{\partial f^o(T)}{\partial T} dk, \quad (2.1)$$

where  $v_g$ ,  $\Xi$ ,  $\hbar\omega$  and  $f^o$  are the group velocity, transmission probability, energy and distribution of the phonons. We consider phonons with a sinusoidal dispersion,  $\omega(k) = \omega_{max} \sin(ka/2)$ , with  $a$  denoting the lattice constant of graphene ( $2.46\text{\AA}$ ) and  $\omega_{max} = 250\text{ THz}$  the cutoff angular frequency. The form of  $f^o$  depends on whether the system is quantum or classical and  $\Xi$  is taken to be a constant.

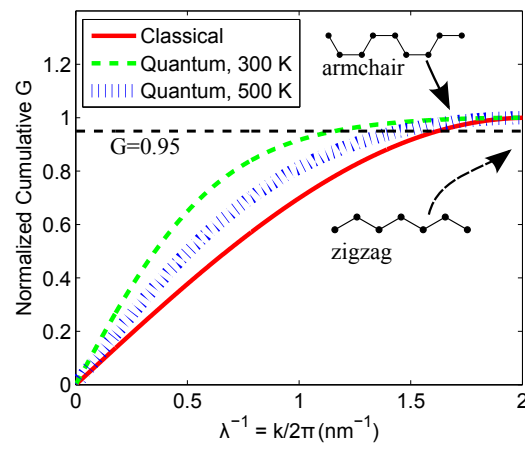


Figure 2.1. Normalized cumulative thermal conductance ( $G$ ) as a function of the reciprocal phonon wavelength,  $\lambda^{-1} = k/2\pi$ . Figure reproduced from Ref. [56].



Figure 2.1 indicates that long wavelength phonons ( $\lambda_{dom} > 1$  nm) dominate thermal transport in GNRs. The wave nature of phonons indicates that it is beyond the resolution of those phonons with a  $\lambda$  much longer than the  $\delta$  of the smooth edges of the GNRs ( $\delta_{zGNR} \approx 0.2\text{\AA}$ ,  $\delta_{aGNR} \approx 0.6\text{\AA}$ ) to distinguish their edge structure, and hence edge roughness scattering should be excluded as the cause for the large  $\Delta\kappa$  observed in previous studies using molecular dynamics (MD) or Green's function method [9, 72]. A mechanism relatively independent to  $\lambda$  will be explored in this work.

## 2.2 Methodology

It should be noted that previous MD studies on  $\Delta\kappa$  mainly used non-equilibrium technique, which might suffer severe size effect due to the strong phonon-thermal bath scattering and the applied temperature bias induces extremely high temperature gradient and hence seriously inhomogeneous thermal strain in the nanosized simulation cells. Unfortunately, the  $\kappa$  of GNR relies greatly on system length and strain, and it is not clear whether these factors will affect the validity of those MD studies qualitatively. Herein we use the LAMMPS package [76] to perform equilibrium MD simulations to calculate the  $\kappa$  of GNRs with the Green-Kubo method. The optimized Tersoff potential parameters [77], which are characterized by more accurate phonon dispersion and anharmonicity than the original set [78], are used to model C-C interactions. The periodic boundary condition (bc) is applied to the length direction and free bc is used for the other two directions.  $\kappa$  is calculated from the longitudinal (subscript  $L$ ) heat current autocorrelation function (HCACF) by

$$\kappa_{LL} = \frac{V}{k_B T^2} \int_0^\tau \langle J_L(\tau) J_L(0) \rangle d\tau \quad (2.2)$$

where  $V$  and  $T$  are the volume and temperature of the GNR, and  $k_B$  is the Boltzmann constant. The full heat current vector  $\vec{J}$  is computed as

$$\vec{J}(t) = \frac{1}{V} \left\{ \sum_i \vec{v}_i \epsilon_i + \frac{1}{2} \sum_{i,j,i \neq j} \vec{r}_{ij} (\vec{F}_{ij} \cdot \vec{v}_i) + \sum_{i,j,k} \vec{r}_{ij} [\vec{F}_j(ijk) \cdot \vec{v}_j] \right\} \quad (2.3)$$

where  $\vec{v}$  and  $\epsilon$  denote the velocity and energy of the atom  $i$ , and  $\vec{r}$  and  $\vec{F}$  are the distance and the two/three-body interaction between different atoms ( $i, j$  or  $k$ ). The GNR is first relaxed at zero pressure and prescribed temperature via the Nosé-Hoover thermostat for 0.8 ns (0.4 fs/step). Then it is switched into the NVE ensemble for another 10.8 ns of which the last 10 ns are used to calculate the HCACF. We have found that an autocorrelation (AC) length shorter than 5 ns can result in largely inaccurate results, thus a sufficiently long AC length is crucial for the validity of this method. We have also checked the length ( $l$ ) dependence of  $\kappa$ , and a saturating trend starts when  $l > 6.0$  nm but longer  $l$  suffers much less statistical fluctuation. A system length of 15 nm is used for all simulations in this work. This method does not need thermal bath during the data production process, resulting in much less phonon-thermal bath scattering and thermal strain inhomogeneity, which is advantageous to previous MD works [9, 79, 80].

### 2.3 Results and Discussions

We compare the  $\kappa$  of aGNRs and zGNRs in Fig. 2.2. As shown in Fig. 2.2a, both  $\kappa_{aGNR}$  and  $\kappa_{zGNR}$  decrease with  $T$  while the latter is always higher. The  $T$  dependence is mainly due to the enhanced Umklapp scattering, and it affects zGNR more strongly than aGNR so that the  $\kappa$  of them eventually becomes the same at temperatures higher than 600 K, when Umklapp scattering dominates. These results agree qualitatively with previous MD simulations [79, 80], though they obtained lower  $\kappa$  due to the size effect or the different interatomic potential used. Figure 2.2b shows that  $\kappa$  increases with width for both types of GNRs. The  $\kappa$  of bulk graphene is also computed by applying the periodic bc to the width direction, and the values are essentially the same for the zigzag and armchair directions ( $\sim 1200$  W/m-K) at 300 K. This indicates that the presence of edges in GNR breaks the isotropy of  $\kappa$  of bulk graphene, endowing it with chirality and width dependence.

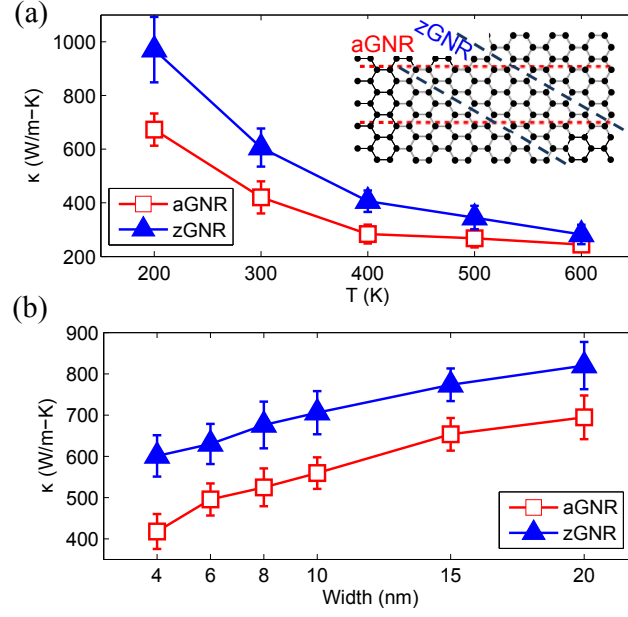


Figure 2.2. (a) and (b): the  $\kappa$  of aGNRs and zGNRs at different  $T$  (width = 4 nm) and for different GNR width ( $T = 300$  K). 15 independent simulations are performed to account for the statistical fluctuation of the MD results. The inset shows how aGNR and zGNR are cut from graphene. Figure reproduced from Ref. [56].

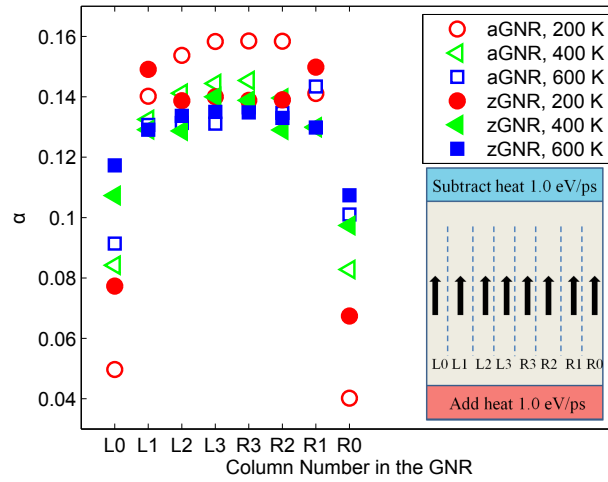


Figure 2.3. Cross-sectional heat flux distribution in aGNRs and zGNRs at various temperatures. The inset shows the simulation domain setup for these calculations. Figure reproduced from Ref. [56].

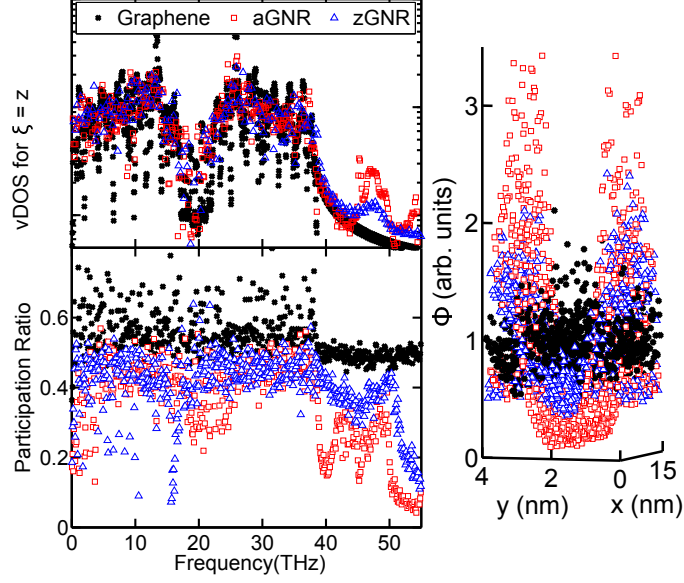


Figure 2.4. (a) and (b): the vDOS and the phonon participation ratio of a bulk graphene, aGNR and zGNR. (c): the spatial distribution ( $\Phi$ ) of modes within  $\Gamma = \{\gamma : p_\gamma < 0.4\}$  for aGNR and zGNRs, and  $\Gamma = \Gamma_{aGNR} \cup \Gamma_{zGNR}$  for graphene. The height in (c) corresponds to the magnitude of localization at that position (x, y). Figure reproduced from Ref. [56].

Noting that Eq. (2.3) can be used to compute the local heat flux vector for a specific group of atoms, we calculate the cross-sectional distribution of the longitudinal heat flux in GNRs, i.e.,  $\alpha = \text{Local } J / \text{Total } J$ . As shown in the inset of Fig. 2.3, the cross-section of a GNR is uniformly divided into eight columns, and a constant heat flux (1.0 eV/ps) is added to or subtracted from either end by directly rescaling the kinetic energy to establish a steady-state heat conduction condition with constant heat flow. The  $\alpha$  for aGNRs and zGNRs are plotted in Fig. 2.3, and we note that the heat flow near edges is significantly suppressed, especially in aGNRs. Similar phenomenon has been reported in Si/Ge core-shell nanowires, Si nanowires and nanotubes, where phonon localization was found to suppress the heat transport near the surface of the nanowire or nanotube greatly [81, 82]. Here our results suggest that smooth edges in nanoscale 2D materials can also play a crucial role in thermal transport.

To further explore the underlying mechanism, we calculate the phonon vibrational density of states (vDOS) and the phonon participation ratio ( $p$ ) [83]. The former is calculated from the Fourier transform of the velocity-velocity AC functions, and the latter, defined for each eigen-mode ( $\gamma$ ), is computed as

$$p_{\gamma}^{-1} = N \sum_i \left( \sum_{\xi} \epsilon_{i\xi,\gamma}^* \epsilon_{i\xi,\gamma} \right)^2 \quad (2.4)$$

where  $\epsilon_{i\xi,\gamma}$  is the eigen-vector component of the  $\gamma$ th normal mode of the lattice vibration in polarization  $\xi$  ( $x$ ,  $y$  or  $z$ ), and  $i$  sums over all the atoms of interest. We use the superposed  $*$  symbol to denote complex conjugate in this work. By definition,  $p_{\gamma} = 1$  if the  $\gamma$ th mode is completely delocalized and  $p_{\gamma} = 1/N$  for complete localization. As shown in Fig. 2.4a, the vDOS is almost the same for bulk graphene, aGNR and zGNR at most frequencies except strong peaks or valleys present in both aGNR and zGNR while absent in bulk graphene near the center and the tail of the vDOS. Figure. 2.4b shows that these modes are localized, which cannot transport thermal energy as efficiently as the delocalized ones [81, 83].

Based on Eq. (2.4), we can evaluate the spatial distribution of eigen-modes in a specific range,  $\Gamma = \{\gamma : p_{\gamma} < p_c\}$ , by

$$\Phi_{\xi,\Gamma}(i) = \frac{\sum_{\gamma \in \Gamma} \epsilon_{i\xi,\gamma}^* \epsilon_{i\xi,\gamma}}{\sum_j \sum_{\gamma \in \Gamma} \epsilon_{j\xi,\gamma}^* \epsilon_{j\xi,\gamma}} \quad (2.5)$$

where  $p_c$  denotes a criteria for localization. In Fig. 2.4c, we plot the  $\Phi_{\xi=z}$  for the modes within  $\Gamma = \{\gamma : p_{\gamma} < 0.4\}$  for aGNR and zGNRs, and  $\Gamma = \Gamma_{aGNR} \cup \Gamma_{zGNR}$  for graphene, where a large value of  $\Phi$  indicates a high concentration of the corresponding set of eigen-modes at atom  $i$ . It is obvious that the localized modes indicated by Fig. 2.4b are localized on the edges of GNRs, and is stronger in aGNR than in zGNR. Moreover, the magnitude of  $\Phi$  decreases exponentially with the distance to edges, which results in less suppression of thermal transport in the central region of GNRs. These phonon spectra analyses combined with the non-uniform heat flux distribution shown in Fig. 2.3 indicate that the strong edge localization of phonons suppresses

thermal transport in GNRs greatly and is responsible for the  $\Delta\kappa$  between aGNR and zGNR. Besides, localized modes can induce inelastic phonon scatterings at the boundary, which reduces  $\kappa$  if the interaction is anharmonic.

## 2.4 Summary

To summarize, we conducted equilibrium MD simulations with the optimized Tersoff potential, and confirmed that  $\kappa$  of zGNRs is higher than that of aGNRs with the same width at a wide range of temperature, though  $\kappa$  was found to be the same for the zigzag and armchair directions in bulk graphene. Edge roughness scattering should be excluded as the reason for such phenomenon, since the dominant phonon wavelength estimated from the Landauer formula can be orders of magnitude longer than the difference between the  $\delta$  of smooth zigzag and armchair edges, and hence it lacks the resolving power to distinguish between them. By decomposing the heat flux along the width direction of a GNR, we observed strong suppression of thermal transport at edges. Analyses on the vDOS and the participation ratio revealed strong localization of phonons in regions near and at the edges of GNRs, especially aGNRs, which suppresses thermal transport. Besides, the enhanced phonon scattering by those localized modes can further reduce  $\kappa$ . Our work revealed the importance of edges to thermal transport in GNRs, and indicates an efficient way to tune the thermal property of 2D materials by engineering the edges.

### 3. THERMAL RECTIFICATION

#### 3.1 Introduction

Inspired by the impact of electric diodes on the electronics industry, extensive attention has been given to the search of rectification of various other transport processes [26, 28, 84]. Thermal rectification (TR) is a diode-like behavior where the heat current changes in magnitude when the applied temperature ( $T$ ) bias is reversed in direction. A perfect thermal rectifier would be one that is highly thermal conductive in one direction while insulating in the other, and it is expected to work as a promising thermal management component of electronics as chip size continues decreasing, or as a stand-alone thermally driven computing system replacing the electronic ones in certain conditions.

Numerous studies have predicted or demonstrated the existence of TR in bulk or nanosized systems, most of which are heterojunctions (HJ) or graded systems [28, 34, 35, 85–89]. For two-segment systems, TR was usually attributed to the different  $T$ -dependence of the thermal conductivity ( $\kappa$ ) [86, 87], and for interfaces TR has been interpreted as the different phonon spectra mismatch before and after reversing the applied  $T$  bias [85]. Phonon localization was suggested to play a role as well [90, 91]. Recently, TR was also predicted to occur in asymmetric pristine carbon nanostructures [9, 31, 34], which are composed of a single material and are attractive for their simple structure and high thermal conductance. Here by “single material” we mean a single and homogeneous material, hence for instance a system composed of both pristine and defected segments is not qualified as a “single material”. However, the origin of TR in such homogeneous nanostructures remains unclear. In this work, we use molecular dynamics and analytical derivations, that phonon confinement in the lateral dimension is required for TR to occur in asymmetric homogeneous struc-

tures made of a single material. We further show that phonon lateral confinement can enable several possible mechanisms which lead to TR, and when the system lateral size becomes large, all these mechanisms do not hold any more, hence TR disappears. This work reveals the key role played by phonon lateral confinement due to edge/surface effects of phonons in TR in asymmetric homogeneous structures, and will provide rational guidance for both theoreticians and experimentalists for the design and application of this new type of thermal rectifier.

### 3.2 Homogeneous Nanoribbon

Non-equilibrium molecular dynamics (NEMD) simulations are performed for graphene nanoribbons (GNR) using the LAMMPS package [76]. The optimized Tersoff potential [77] is adopted for modeling C-C interactions. Schematics of the supercells are shown in Fig. 3.1a, where the atoms at the two ends are fixed to make a suspended structure, and the free boundary condition is applied to the Y and Z directions. The GNRs are first relaxed in the NVT ensemble for  $5 \times 10^6$  time steps (0.4 fs/step) with the Nosé-Hoover thermostat. Then NEMD is performed for another  $8 \times 10^6$  steps. We use the Berendsen thermostat as heat baths, and maintain the same number of atoms adjacent to the two ends of the GNR at different  $T$  (300 K for the hot end and 300 K $-\Delta T$  the cold). The net heat current due to the bias  $\Delta T$  is computed as  $J = (\partial E_{hot}/\partial t + \partial E_{cold}/\partial t)/2$ , where  $E_{hot}$  and  $E_{cold}$  are the total energy that has been added to or subtracted from the atoms in the hot and cold thermostats, respectively.

The TR ratio ( $\eta$ ) is defined as

$$\eta = \frac{\kappa_{forward}}{\kappa_{backward}} - 1 = \frac{J_{forward}}{J_{backward}} - 1 \quad (3.1)$$

where the subscripts indicate whether the rectifier is operated at *forward* (heat flows left-to-right or wider-to-narrower) or *backward* bias. Figure 3.1b shows  $J$  as a function of the imposed  $|\Delta T|$  in a trapezoidal-GNR. Sufficiently high  $\Delta T$  is needed to initiate TR and the direction of decreasing width ( $\eta > 0$ ) is favored, which is consistent with



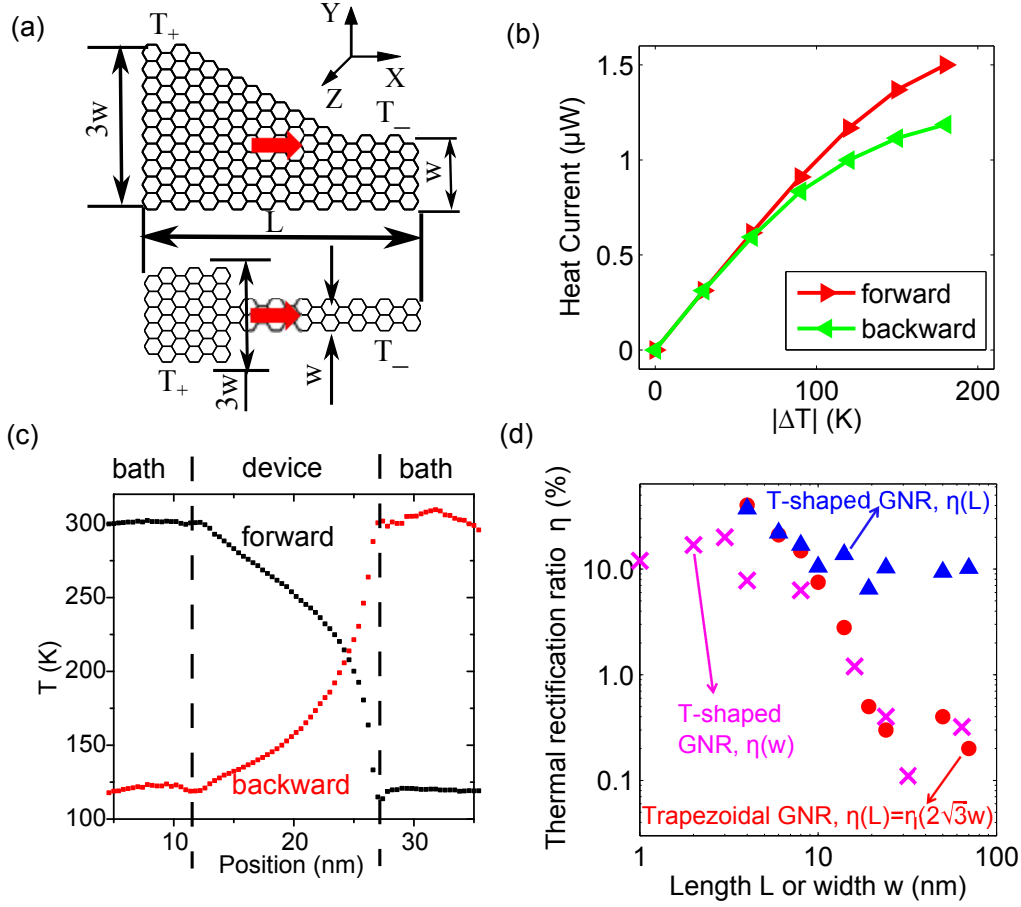


Figure 3.1. (a) geometrical definition of the length ( $L$ ) and width ( $w$ ) of the trapezoidal-GNRs and T-shaped GNRs; the width ratio of the GNRs is maintained at 3:1; the *forward* direction is indicated by the arrows. (b) heat current in a trapezoidal-GNR as a function of  $|\Delta T|$ . (c) temperature profiles in the trapezoidal-GNRs. (d)  $\eta$  as a function of the length or width of GNRs.  $w = 2$  nm when  $L$  varies and  $L = 6$  nm when  $w$  varies for the T-shaped GNRs, and  $L = 2\sqrt{3}w$  for the trapezoidal-GNRs. Figure reproduced from Ref. [92].

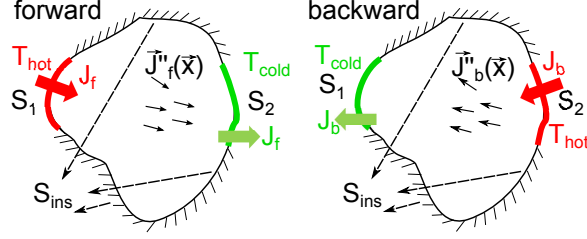


Figure 3.2. Schematic of the structure of an arbitrary shape applied with *forward* (left) and *backward* (right) temperature bias.  $S_1$  and  $S_2$  denote two surfaces maintained at  $T_{hot}$  and  $T_{cold}$  respectively for the *forward* direction and reversed for the *backward* direction.  $S_{ins}$  denotes insulating (adiabatic) thermal boundaries.  $J_f$  and  $J_b$  are the total heat transfer rates, and  $\vec{J}_f''(\vec{x})$  and  $\vec{J}_b''(\vec{x})$  are the local heat fluxes. Figure reproduced from Ref. [92].

previous studies on triangular ones [9,31]. The temperature profiles for the *forward* and *backward* cases are plotted in Fig. 3.1c, which demonstrates higher temperature gradient and hence lower  $\kappa$  at narrower region. As the length ( $L$ ) and width ( $w$ ) of the trapezoidal-GNR change by the same scale ( $L = 2\sqrt{3}w$ ) when its size changes, we also study T-shaped GNRs (the lower structure in Fig. 3.1a) to evaluate which dimension has a more profound effect on TR. As shown in Fig. 3.1d,  $\eta$  of T-shaped GNRs decreases quickly with increasing  $w$ , but much more slowly with  $L$ , indicating that a sufficiently small lateral dimension is crucial for TR. In such narrow GNRs, phonons propagating in or close to the length direction are the predominant heat carriers, and the upper and lower edges are the dominant phonon scattering centers.

The strong lateral size dependence of TR motivates us to formally check if TR can exist in asymmetric structures of bulk size. We consider an asymmetric geometry with arbitrary dimension and shape as shown in Fig. 3.2, of which the surfaces  $S_1$  and  $S_2$  are maintained at  $T_{hot}$  and  $T_{cold}$  respectively for the case of *forward* bias and vice versa for *backward*, and the remaining surfaces are insulated. For the insulated

(adiabatic) surfaces  $S_{ins}$ 's shown in Fig. 3.2, we have  $\frac{\partial T}{\partial \vec{\nu}}|_{S_{ins}} = 0$ , where  $\vec{\nu}$  is the surface normal vector. Heat conduction is governed by the heat diffusion equation,

$$\vec{\nabla} \cdot \left\{ \kappa [T(\vec{x})] \cdot \vec{\nabla} T(\vec{x}) \right\} = 0, \quad (3.2)$$

where  $\kappa$  is the thermal conductivity tensor which only depends on temperature in the bulk regime, but it is not necessarily isotropic. If we set the axes of the coordinate system along the principal directions, i.e.,  $\kappa$  is diagonal, we can linearize Eq. (3.2) through the Kirchhoff transformation by defining a new quantity,  $K_i(T) = \int_{\epsilon}^T \kappa_{i,i}(T) dT + \kappa_{i,i}(\epsilon)$ , where  $\kappa_{ii}$  is the  $i$ th component of the diagonal of the thermal conductivity tensor. It is evident that  $\kappa_{i,i}(T) = \frac{\partial K_i(T)}{\partial T}$ . Physically,  $\epsilon$  can be of any non-negative value as long as it is lower than any phase-change temperature. Therefore,

$$\kappa_{i,i}[T(\vec{x})] \cdot \frac{\partial T(\vec{x})}{\partial x_i} = \frac{\partial K_i[T(\vec{x})]}{\partial x_i}, \quad (3.3)$$

and Eq. (3.2) becomes

$$\sum_i \frac{\partial^2 K_i}{\partial x_i^2} = 0. \quad (3.4)$$

For the *forward* and *backward* cases, the only difference regarding Eq. (3.4) is the boundary conditions at the two surfaces  $S_1$  and  $S_2$ . We now have a complete set of partial differential equations together with boundary conditions for the two cases, which are

$$\left\{ \begin{array}{l} \sum_{i=1}^N \frac{\partial^2 K_{i,f}}{\partial x_i^2} = 0, \\ \frac{\partial K_f}{\partial \vec{\nu}}|_{S_{ins}} = 0, \\ K_{i,f}|_{S_1} = K_i(T_{hot}), \\ K_{i,f}|_{S_2} = K_i(T_{cold}), \end{array} \right. \quad (3.5)$$

for the *forward* case, and

$$\begin{cases} \sum_{i=1}^N \frac{\partial^2 K_{i,b}}{\partial x_i^2} = 0, \\ \frac{\partial K_b}{\partial \vec{v}}|_{S_{ins}} = 0, \\ K_{i,b}|_{S_1} = K_i(T_{cold}), \\ K_{i,b}|_{S_2} = K_i(T_{hot}), \end{cases} \quad (3.6)$$

for the *backward* case, respectively. Summing up Eqs. 3.5 and 3.6 generates

$$\begin{cases} \sum_{i=1}^N \frac{\partial^2 K_{i,t}}{\partial x_i^2} = 0 \\ \frac{\partial K_t}{\partial \vec{v}}|_{S_{ins}} = 0, \\ K_{i,t}|_{S_1} = K_i(T_{hot}) + K_i(T_{cold}), \\ K_{i,t}|_{S_2} = K_i(T_{cold}) + K_i(T_{hot}). \end{cases} \quad (3.7)$$

where we have defined  $K_{i,t}[T(\vec{x})] = K_{i,f}[T(\vec{x})] + K_{i,b}[T(\vec{x})]$ . The subscripts  $f$ ,  $b$ , and  $t$  stand for "forward", "backward", and "total", respectively.

The solution to Eq. (3.7) is unique and must be a constant

$$K_{i,t} = K_i(T_{hot}) + K_i(T_{cold}) = \text{const.} \quad (3.8)$$

Therefore,

$$\frac{\partial K_{i,t}}{\partial x_i} = \frac{\partial K_{i,f}}{\partial x_i} + \frac{\partial K_{i,b}}{\partial x_i} = 0. \quad (3.9)$$

Plugging in Eq. (3.3) leads to

$$\kappa(T_f) \cdot \frac{\partial T_f}{\partial \vec{x}} + \kappa(T_b) \cdot \frac{\partial T_b}{\partial \vec{x}} = 0, \text{ or } \vec{J}''_f(\vec{x}) + \vec{J}''_b(\vec{x}) = 0, \quad (3.10)$$

which means that **for any N-dimensional structure with anisotropic and temperature-dependent  $\kappa$ , at any position  $x$ , the local heat flux vectors ( $\vec{J}''_b$  and  $\vec{J}''_f$ ) in the *forward* and *backward* cases are of the same magnitude but in opposite directions.** As an immediate result, the heat transfer rates for the two cases must be equal, i.e.,  $J_f = J_b$ . This is a strong conclusion of the absence of TR in bulk-size single-material homogeneous structures. To verify

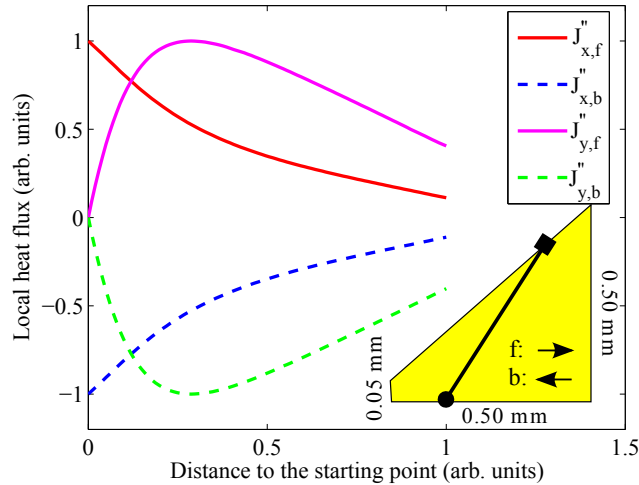


Figure 3.3. Numerical verification for isotropic  $\kappa$ . The inset is the structure used for the numerical calculations. The heat flux, which has  $x$  and the  $y$  components, is measured along an arbitrary path (from the filled circle to the filled square) as a function of the distance to the starting point.  $f$  and  $b$  represent *forward* and *backward* cases, respectively. Figure reproduced from Ref. [92].

Eq. (3.10), we have also solved the heat transfer problem for the systems in Fig. 3.2 using the finite element method. The structure is a right trapezoid, as shown in the inset of Fig. 3.3. For the *forward* case, the temperature is maintained at 600 K on the left end, and 10 K on the right end, and vice versa for *backward*. We consider both isotropic  $\kappa$  and anisotropic  $\kappa$  cases, and the results are plotted in Fig. 3.3 and Fig. 3.4, respectively, with the  $\kappa$ - $T$  curves in Fig. 3.5.

We select an arbitrary path across the structure, and measure the the heat flux vector  $\vec{J}''$  as a function of position on this path. In both Fig. 3.3 and Fig. 3.4, the heat flux vectors at any position are same in magnitude but opposite in direction for *forward* and *backward* cases. The results verifies our analytical proof of the absence of thermal rectification in asymmetric bulk-size single material.

It should be noted that for bulk-size heterojunctions,  $\kappa$  not only depends on temperature, but also on space, leading to the possibility of TR [88,89,93]. This is a different behavior from that of bulk-sized homogeneous structures of a single material.

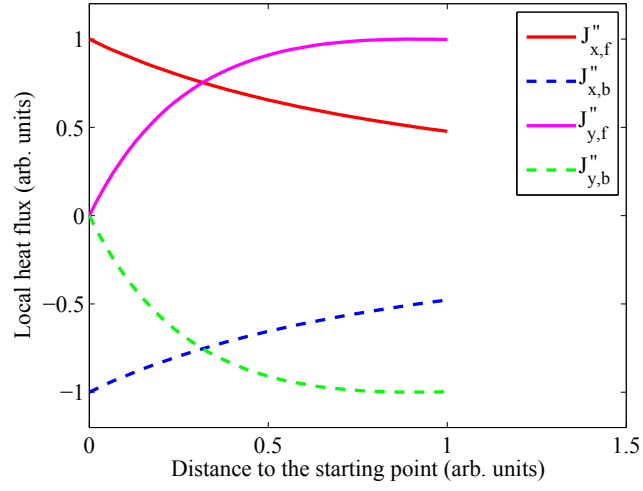


Figure 3.4. Numerical verification for anisotropic  $\kappa$ , i.e.,  $\kappa_{xx} \neq \kappa_{yy}$ . Figure reproduced from Ref. [92].

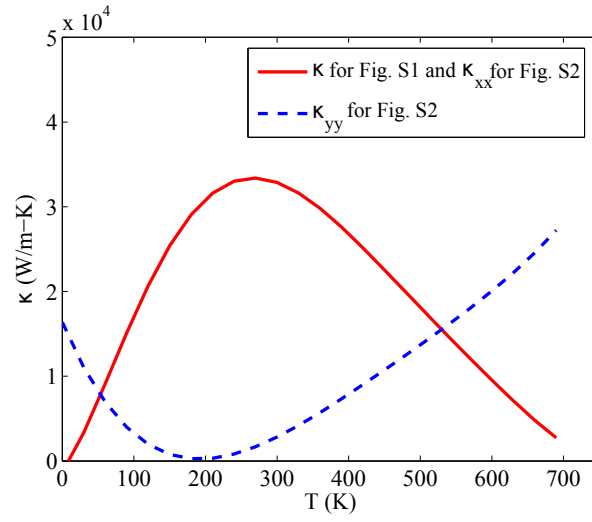


Figure 3.5.  $\kappa$ 's used for the isotropic case in Fig. 3.3 and the anisotropic case in Fig. 3.4. Figure reproduced from Ref. [92].

The fact that single materials with a bulk lateral dimension cannot generate TR indicates that the phonon lateral confinement is necessary for TR to occur. This is a key finding of this work. In the phonon lateral confinement regime, the effects of lateral boundary on phonon properties are important. To explore why phonon lateral confinement is necessary, we examine several mechanisms that are known to be relevant in other TR systems.

We first examine the phonon spectra mechanism [31], i.e., the amount of overlap ( $\Psi$ ) between the phonon spectra of the two sides of the structure changes after switching the thermostats. It has been commonly used to explain TR across interfaces between two dissimilar materials [35,85,94,95]. The vibrational density of states (vDOS) in Fig. 3.6a is computed as the Fourier transform of the out-of-plane component of the atomic velocity-velocity autocorrelation function. The vDOS is broadened when cutting a bulk graphene into a nanoribbon where edges are present. In parallel with Eq. (3.1), we define  $H = \Psi_{forward}/\Psi_{backward} - 1$  to quantify the phonon spectra overlap. Figure 3.6b shows that the spectra overlaps are indeed different before and after switching the thermostats for both in-plane ( $p = X - Y$ ) and out-of-plane ( $p = Z$ ) polarizations. We note that such difference is enabled by the small ribbon width, so that the local phonon spectra not only depends on temperature, but also on the width. The dependence of phonon spectra on the lateral size of nanostructures was observed previously [96]. TR due to phonon spectra mismatch resulted from device-thermostat interactions was reported in a diamond nano-pyramid [90]. If the width increases to macroscopic size, the local phonon spectra will only depend on the temperature, and the phonon spectra overlap will be the same before and after switching the thermostats, thus TR vanishes. In contrast, the difference in phonon spectra overlap across interface in heterojunctions [35,85,94,95] is enabled by two different materials, not by the confined lateral dimension. Hence, increasing the lateral dimension for an interface will not affect its TR.

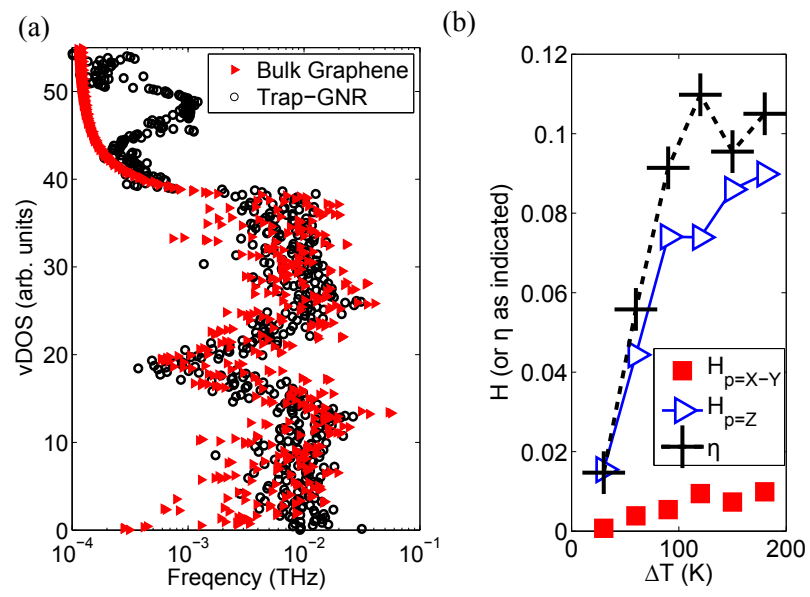


Figure 3.6. (a) out-of-plane vibrational density of states. (b)  $H$  and  $\eta$  as a function of  $\Delta T$ . Figure reproduced from Ref. [92].



The second possible mechanism is the inseparable dependence of  $\kappa$  on  $T$  and space, which has usually been used to explain TR in bulk materials, such as two-segment bars of different materials [86, 87, 93]. Note that  $\kappa$  is given as

$$\kappa \propto \int d\omega v_g(\omega) \lambda(\omega) \hbar \omega D(\omega) \partial[n(\omega, T)] / \partial T, \quad (3.11)$$

where  $\omega$ ,  $v_g$ ,  $\lambda$ ,  $D$  and  $n$  are the angular frequency, group velocity, mean free path, density of states and the distribution function of phonons, respectively, and  $\hbar$  is the reduced Planck constant. For our GNR, the phonon lateral confinement effect can make both  $\lambda$  and  $D$  dependent on the width, so that the local  $\kappa$  becomes space-dependent. Such width-dependent  $\kappa$  of GNR has been previously reported [56, 70, 80, 97]. Under this condition, heat conduction does not follow Eq. (3.10), and TR can occur. Here we note that the inseparability in asymmetric GNRs is enabled by the phonon lateral confinement effect [56], not by using two different materials in the two-segment bars. As the width of the asymmetric GNR increases to bulk size,  $\kappa$  only depends on  $T$ , thereby no TR can occur. Also, it is apparent that the inseparable thermal conductivity mechanism and the phonon spectra mechanism are not independent, since  $\kappa$  depends partially on  $D(\omega)$ .

To explicitly show the role played by the small width on  $\lambda(\omega)$ , we explore the third possible mechanism — phonon localization, which has been suggested as a mechanism of TR in Ref. 34 for carbon nanocones and also reported in Ref. 90 for diamond nano-pyramid.

We use the participation ratio defined in Eq. (2.4) to quantify phonon localization, where we refer to  $p < 0.4$  as phonon localization, which ensures that all phonons in the bulk graphene are delocalized under this criteria. We can also picture the spatial distribution of a specific range ( $\Lambda$ ) of normal modes using Eq. (2.5). A larger value of  $\phi_{i\alpha, \Lambda}$  indicates stronger localization of modes  $\Lambda$  on the  $i$ th atom.

Figure 3.7a shows  $p_\lambda$  for the bulk graphene and a T-shaped GNR. As we can see,  $p_\lambda$  of the GNR is usually less than that of the bulk graphene, indicating stronger phonon localization in the former. The spatial distribution of the localized modes (LM) shown in Figs. 3.7b and c reveals that localized modes prefer edges. When heat flows in the

direction of increasing width (Fig. 3.7c), more LMs can be found on the narrower end, which acts as the bottleneck of thermal transport channel in such narrow GNRs. Therefore, delocalized modes have a narrower channel of propagation, and hence the effective  $\kappa$  is reduced. Phonon localization can also be enhanced on the wider side when heat flows in the decreasing width direction (Fig. 3.7b), but has less effect on thermal transport since the channel bottleneck is usually still the narrower end. Besides, LMs on edges can act as collision centers for other phonons, which alters  $\lambda(\omega)$  and makes it space-dependent. In this sense, the phonon edge localization mechanism is correlated to the inseparable thermal conductivity mechanism through the space-dependent  $\lambda(\omega)$ . The above mechanism selects the direction of decreasing width as the favored direction of thermal rectifiers. When the GNR width increases to bulk size, three-phonon scattering dominates while edge scattering becomes unimportant, hence, TR disappears as depicted in Fig. 3.1d.

To explore the origin of edge localization, we examine the spring constant spectra of the edge atoms and the interior ones in T-shaped GNRs. By calculating the restoring force  $\Delta F$  after a small displacement  $\Delta r$  of an atom, we can obtain the spring constant spectra of C atoms in different regions of a GNR with  $\Gamma = -\Delta F/\Delta r$ . The results are plotted in Fig. 3.8. Compared with the interior atoms, the spring constant spectra of the edge atoms are broadened into higher and lower strength regions. The interior atoms have a much better translational symmetry than edge atoms that lose neighbors on one side. The low frequency tail results from the loss of neighbor atoms, which makes the environment softer; on the other hand, the high frequency tail is caused by reconstructions of the edge C-C bonds [91], which shortens the bonding length and makes the bonds harder. The distorted spring constant spectra place edge atoms in a quite different force environment from interior ones, which facilitates the generation of LMs. Moreover, since temperature affects the mean square displacement of C atoms directly, the spring constant disorder can be amplified by higher  $T$ . Consequently, higher  $\Delta T$  and asymmetric geometry are needed to generate LMs asymmetrically and hence rectify heat flow, which can be confirmed

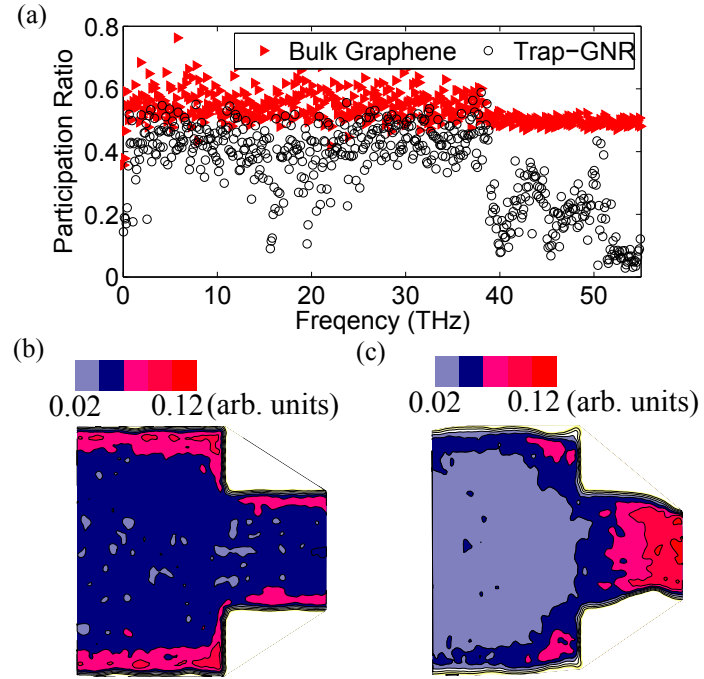


Figure 3.7. (a) participation ratio of bulk graphene and T-shaped GNRs. Spatial distribution of localized modes when heat flows in the direction of (b) decreasing width (*forward*), and (c) increasing width (*backward*). Figure reproduced from Ref. [92].

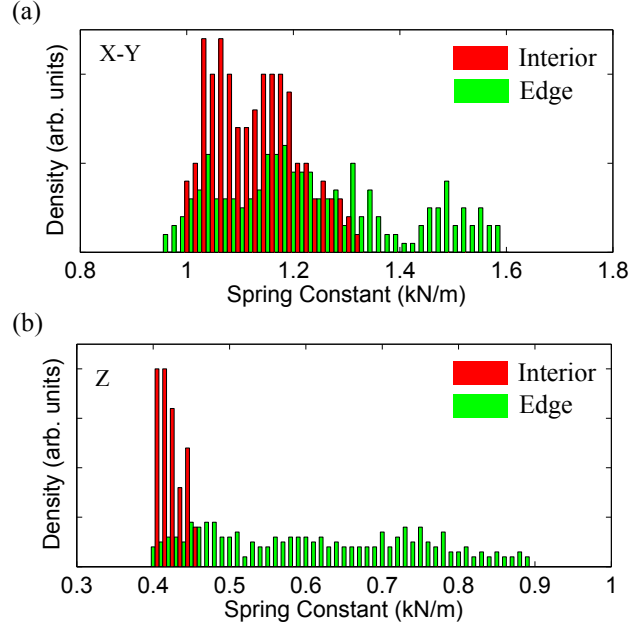


Figure 3.8. Spring constant spectra of (a): in-plane motion and (b): out-of-plane motion of atoms. Figure reproduced from Ref. [92].

by Fig. 3.1b and d. As the non-equilibrium Green's function (NEGF) method uses constant spring constants due to the high computational cost requested by a T-dependent and anharmonic one, the previous NEGF study predicts no TR for two-terminal GNRs since no asymmetric phonon spectra like Fig. 3.7b and c can be generated, and multiple-terminal devices are needed which produces TR owing to a different mechanism [98].

Phonon spectra of materials are usually broad, but the localization of phonons are selective to only certain modes. The broad spectra of phonons limits the efficiency of TR significantly below its electric counterpart which benefits from the fact that only a narrow spectra of electrons around the Fermi level contribute to conductance. In view of this analogy, TR can be potentially enhanced by narrowing the phonon spectra, such that all modes are localized in one direction of heat transport but delocalized in the opposite.

In the above, we have shown that TR in asymmetric GNRs can be explained by three possible mechanisms: phonon spectra overlap, inseparable dependence of  $\kappa$  on  $T$  and space, and phonon edge localization. All mechanisms require small GNR width so that phonons are confined. Therefore, phonon lateral confinement is the fundamental origin of TR in such asymmetric homogeneous materials. Based on these findings, we have also checked other asymmetric nanostructures such as non-uniform nanowires, thin films, and quantum dots, as shown in Fig. 3.9, which may also exhibit TR if they are in the phonon confinement regime, i.e., the lateral dimension is small enough compared to  $\lambda$ . It should be noted that Fig. 3.9e shows a structure similar to that proposed in Ref. 99, but in our case the edges of both sides of the teeth are smooth, while in Ref. 99 the specularities of the two sides are different. In addition, our mechanism is significantly different from Lee et al.'s mechanism of phonon confinement. [90] Our phonon edge confinement is in the device itself, while Lee et al.'s confinement focuses on the interaction between the device and contacts. These mechanisms can possibly be combined to achieve higher  $\eta$ . We note that a recent experimental study reported TR in large-size reduced graphene oxide [100], and the TR was attributed to the asymmetric geometry. Based on our findings, we argue that the asymmetric geometry is not sufficient and their TR is probably due to other mechanisms or experimental uncertainty. For example, graphene with both pristine and defected segments can sustain TR at large size. [35]

### 3.3 Asymmetrically Defected Graphene Nanoribbon

Defect engineering is also a promising approach for making thermal rectifiers. Here we propose the pristine-defected GNR as a promising thermal rectifier and systematically study the effects of design parameters. Compared with other materials, the 2D nature of graphene and GNR allows for much easier artificial introduction of defects, which is essential for tailoring the thermal and electrical properties of pristine materials for various applications including TR.

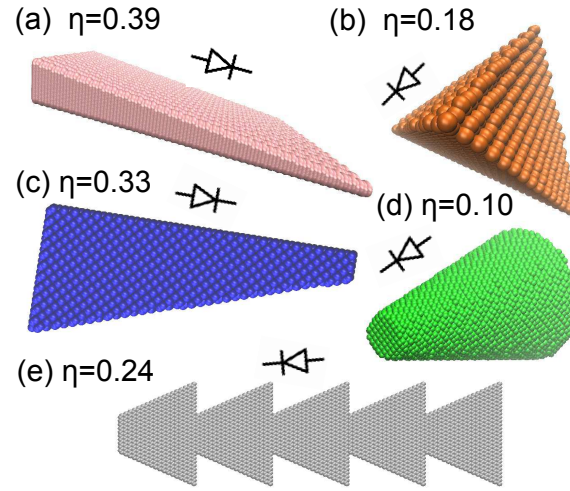


Figure 3.9. Homogeneous nanostructures as potential thermal rectifiers: (a) nano thin films with non-uniform thickness, (b) asymmetric quantum dots, (c) nano thin films with non-uniform width, (d) non-uniform nanowires, and (e) thermal rectifier series as proposed in literature [99], but with atomic smoothness for all edges. Directions of higher  $\kappa$  and the value of  $\eta$  are indicated. (a)-(d) have diamond lattice while (e) is cut from graphene, and all  $\eta$ 's are calculated using the optimized Tersoff potential at  $T = 300$  K and  $\Delta T = 90$  K. Figure reproduced from Ref. [92].

As shown in Fig. 3.10a, single-vacancy (SV) and di-vacancy (DV) can be created by removing a single C atom or two neighboring atoms. If a C-C bond is rotated by  $90^\circ$ , four hexagons in the graphene lattice are transformed into two pentagons and two heptagons, which forms the Stone-Wales defect [SW(55-77)]. These types of point defects were found to reduce the  $\kappa$  of pristine GNRs significantly ( $> 65\%$ ) with a concentration of one defect per thousand atoms [101]. Substitutional silicon defect (Si) was also predicted to be stable in GNRs and correlated with a drastic reduction of  $\kappa$  in a first-principles study [102]. In our work, defects are created randomly, based on a prescribed concentration ( $\alpha$ ), in the right side of the GNR, as indicated by the dashed line in Fig. 3.10b.  $\alpha$  is defined as the ratio of the number of defected nodes to the total number of the nodes in the right side of the hexagon network. Non-equilibrium molecular dynamics is performed using LAMMPS [76]. Periodic boundary condition is applied to the width (Y) direction to eliminate the edge effects, as the dangling edges are also defects (extended defect) in a broad sense [101]. We have checked that the width has minor effect on simulation results for GNRs wider than 3.3 nm, and hence the 4.0 nm wide GNRs used here suffer negligible size effects in the Y direction. The outermost columns of atoms at the two ends of the GNR in the X direction are fixed to avoid the sublimation of atoms, and free boundary condition is applied to the cross-plane direction. The C-Si and C-C interactions are modeled with the original [78] and the optimized [77] Tersoff potential, respectively. The GNR is first relaxed at zero pressure and constant temperature,  $\bar{T}$ , for  $3 \times 10^6$  time steps (0.25 fs per step) using the Nosé-Hoover thermostat. Then, two different temperatures, i.e.,  $\bar{T} + \Delta T/2$  and  $\bar{T} - \Delta T/2$ , are applied to regions adjacent to the ends of the GNR using two Nosé-Hoover thermostats, and steady state is achieved after 0.5 ns. The simulation is then continued for another 2 ns for data collection. The heat current resulting from the temperature bias,  $\Delta T$ , is computed as  $J = \left( \frac{dE_{hot}}{dt} + \frac{dE_{cold}}{dt} \right) / 2$ , where  $E_{hot}$  and  $E_{cold}$  are the total energy that has been added to or subtracted from the atoms in the hot and cold thermostats, respectively.

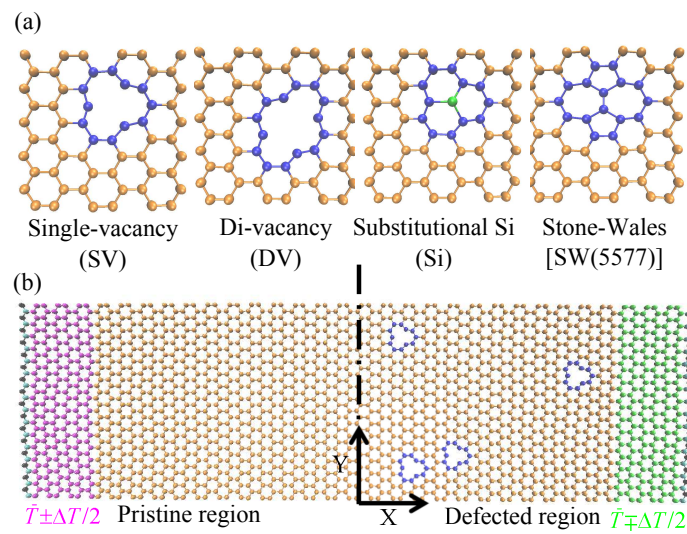


Figure 3.10. (a) Types of point defect studied in this work. (b) Simulation domain setup for pdGNRs. The dashed line divides the GNR into pristine region and defected region, where defects are randomly created inside the latter. Figure reproduced from Ref. [35].



We herein study the effect of  $\bar{T}$ ,  $\Delta T$ ,  $\alpha$ , type of defect, length of the GNR, and the ratio of the length of the pristine region to that of the defected region ( $R_L = L_{pristine}/L_{defected}$ ), thus covering most of the factors that may affect thermal properties of defected GNRs greatly. To account for the randomness of defects, twelve independent simulations are run on independently generated GNRs with random defects for each data point.

First, we evaluate  $\eta$  in GNRs composed of a 7 nm long pristine region and a 7 nm long defected region. GNRs with four types of defect, i.e., SV, DV, Si and SW(55-77), are studied in separate simulations with  $\alpha = 1.5\%$ . We vary the average temperature  $\bar{T}$  and use  $\Delta T = 90$  K for all cases. As shown in Fig. 3.11, TR is significant ( $\eta \approx 0.7$  for SV and Si, and  $\eta \approx 0.3$  for DV and SW(55-77)) at 200 K, but weakens at higher temperatures. Similar trend was also found in other types of thermal rectifiers [9, 31, 34], and is usually attributed to the mismatch of the phonon spectra between the two sides of a rectifier. When the average temperature increases, such difference becomes weaker with respect to the total vibrational energy, and hence TR is suppressed. Comparing  $\eta$  of different types of defect at the same  $\bar{T}$ , we find GNRs with SV and Si defects rectify heat flow more strongly than those with DV and SW(55-77) defects. Note that each DV or SW(55-77) defect contributes two defected nodes to the carbon network of graphene, i.e., two defected nodes per defect. Accordingly, with the same  $\alpha$  (same number of defected nodes), SV and Si defects are more scattered than DV and SW(55-77), and hence the formers tune the phonon transport more strongly than the latters. Ref. [101] revealed that with  $\alpha = 0.1\%$ , SV defects reduce the  $\kappa$  of GNRs by 81%, while DV and SW(55-77) only reduce it by 61%, in consistency with our work.

We plot  $\eta$  of pdGNRs as a function of length (L) for different  $\Delta T$  in Fig. 3.12a, and observe that  $|\eta|$  increases as  $\Delta T$  increases, consistent with previous studies [62]. Notably,  $|\eta|$  decreases as the GNR length increases up to 100 nm as predicted by MD, indicating that this type of thermal rectifier has the best rectifying power at small size. This observation inspires us to check whether thermal rectification should

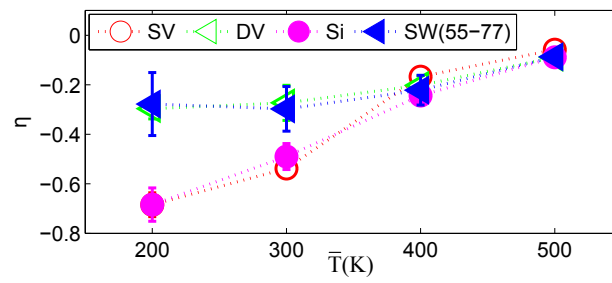


Figure 3.11. Temperature dependence of  $\eta$  for pdGNRs with different types of point defect. Figure reproduced from Ref. [35].

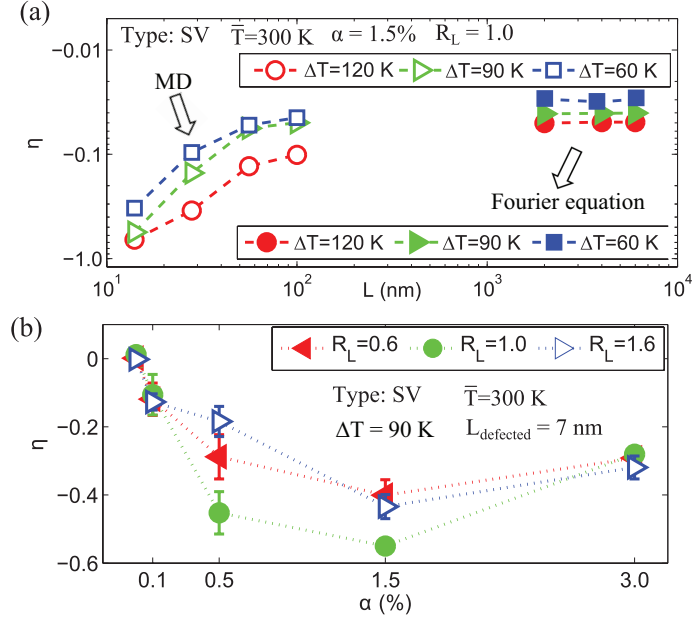


Figure 3.12. (a)  $\eta$  as a function of  $L$  of the pdGNRs for different  $\Delta T$ . Data points denoted by unfilled and filled markers are computed by MD simulation and by solving the 1D, steady-state Fourier heat conduction equation, respectively. (b)  $\eta$  as a function of  $\alpha$  for pdGNRs with different  $R_L$ . Figure reproduced from Ref. [35].

diminish at macroscopic size. Here we consider ( $L \geq 2 \mu m$ ) where heat conduction transits to the diffusive regime, and we use the conventional Fourier equation to evaluate TR. We fit the  $\kappa$  of pristine and defected GNRs [101] as a function of temperature, and numerically solve the 1D, steady-state heat conduction equation  $\nabla_x \{ \kappa[x, T(x)] \nabla_x T \} = 0$  with the temperature at the two ends maintained at  $300 \text{ K} + \Delta T/2$  and  $300 \text{ K} - \Delta T/2$ , respectively. In this regime, pdGNRs show a length-independent TR of 3-5% for the different  $\Delta T$  considered here. The TR mechanism becomes the same as the bulk thermal rectifier proposed in Ref. [89], i.e., the  $\kappa(x, T)$  is not a separable function of  $x$  and  $T$ . This non-diminishing, length-independent TR in macroscopic defected GNR is distinct from that of rectifiers using asymmetric shapes [9, 31], which completely lose TR at macroscopic length, as explained in the last section.

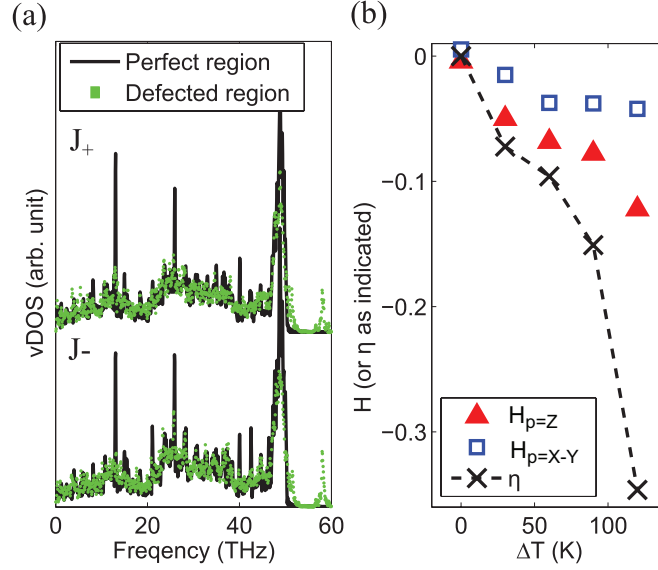


Figure 3.13. (a) vDOS of the perfect region and defected region for opposite heat flow directions. (b)  $H$  and  $\eta$  for various  $\Delta T$ . Figure reproduced from Ref. [35].

We then consider the effect of  $R_L$ .  $R_L \rightarrow \infty$  means a pristine GNR, while  $R_L \rightarrow 0$  means a homogeneously defected GNR. Both extremes reduce to a symmetric structure and thus cannot rectify heat flow. Figure 3.12b shows that a moderate partition ( $R_L \approx 1.0$ ) of the pristine and defected region usually generates higher  $|\eta|$  than biased cases. Similarly, a medium  $\alpha$  (0.5%  $\sim$  1.5%) is also preferable to the extremes, since very low  $\alpha$  corresponds to pristine GNR and very high  $\alpha$  reduces  $\kappa$  too much for both directions. Thus, as for defect engineering, we conclude that an  $\alpha$  on the order of 1% is needed for TR, compared with 0.1% for notably reducing  $\kappa$  and 0.0001% for tailoring electronic properties.

Figure 3.13 shows the vibrational density of states (vDOS), which is the summation of the Fourier transform of the autocorrelation function of atomic velocities in each polarization ( $p = X, Y, Z$ ) [62]. For both forward ( $J_+$ ) and reversed ( $J_-$ ) heat flow, we calculate the overlap ( $S$ ) between the acoustic region of the vDOS of the pristine and defected region using the method in Ref. [62]. In parallel with Eq. (1.1), we compute  $H = (S_+ - S_-)/S_-$  for both in-plane (X-Y) and out-of-plane (Z) po-

larizations to show the change of  $S$  when the sign of  $\Delta T$  reverses. Consistent with previous studies [62, 103],  $\eta$  and  $H$  have the same sign and show quite strong positive correlation, which confirms the suitability of the spectra overlap theory [62] as a qualitative explanation to TR.

As a final remark, note that in contrast to other GNR-based thermal rectifiers [9, 31] of asymmetric shape that induces asymmetric boundary scattering of phonons [28], the asymmetrically defected GNRs proposed here favor large width, thus saving the need for complicated patterning process in making the narrow and regular shapes. For very narrow GNRs, there is very high concentration of *edge* defects [101], and they dominate the thermal transport instead of the asymmetrically introduced point defects, and hence TR is greatly reduced.

### 3.4 Summary

To summarize, we have found that phonon confinement is the origin for TR in asymmetric homogeneous materials, and that TR diminishes in bulk-sized ones. We have shown three possible mechanisms for TR in asymmetric GNRs: phonon spectra overlap, inseparable dependence of  $\kappa$  on temperature and space, and phonon edge localization. These mechanisms are related to each other in a complicated manner. The width-dependent phonon spectra  $D(\omega)$  can contribute to the space-dependence of  $\kappa$ . Also, the phonon edge localization can make  $\lambda(\omega)$  space-dependent, which also contributes to the space-dependence of  $\kappa$ . The third mechanism explicitly shows the role played by the edges in the phonon confinement regime. When the lateral size of the device approaches the bulk limit, such edge effect is smeared out by three-phonon scatterings and TR disappears. We also show that other asymmetric nanostructures, such as asymmetric nanowires, thin films and quantum dots, of a single material are potential thermal rectifiers.

We have also studied the TR effect in asymmetrically defected GNRs using classical molecular dynamics simulations. Low  $\bar{T}$ , high  $\Delta T$ , moderate  $\alpha$  ( $\sim 1\%$ ) and  $R_L$ ,

and short system length were found to be optimum for high thermal rectifying efficiency of the thermal rectifier proposed in this work. We also revealed that SV and Si defects tune thermal transport more strongly than DV and SW(55-77) defects with the same concentration, and are thus preferable in making thermal rectifiers. The thermal rectification decreases as the GNR length increases and eventually stabilizes at a length-independent value for macroscopic length when heat conduction transits to the diffusive regime. This work extends defect engineering to the field of thermal management and thermal signal manipulation with 2D thermal rectifiers.

## 4. THERMAL TRANSPORT IN MULTILAYER STRUCTURES

### 4.1 Introduction

Thermoelectric effect is a phenomenon in which a temperature bias generates electrical voltage (Seebeck effect) or an electrical current generates temperature bias (Peltier effect). The Peltier effect can be used for on-chip cooling of electronic devices, in which a thermoelectric component is attached to the hot spot and an electrical current is used to remove the heat actively from it.

The energy conversion efficiency of a thermoelectric material is related to the dimensionless figure of merit ( $ZT$ ) as

$$ZT = \frac{S^2 \sigma T}{\kappa_e + \kappa_L}, \quad (4.1)$$

where  $S$  is the Seebeck coefficient,  $\sigma$  is the electrical conductivity,  $\kappa_e$  is the electronic thermal conductivity, and  $\kappa_L$  is the lattice thermal conductivity. As  $\sigma$  is directly coupled to  $\kappa_e$  by the Wiedemann-Franz law as

$$\frac{\kappa_e}{\sigma} = L_{W-F} T, \quad (4.2)$$

where  $L_{W-F}$  is the Lorentz number, Eq. (4.1) can be transformed into

$$ZT = \frac{S^2}{L_{W-F} + \frac{\kappa_L}{\sigma T}}. \quad (4.3)$$

Equation (4.3) suggests that increasing  $S$  or  $\sigma$ , or reducing  $\kappa_L$  can increase  $ZT$ .

Extensive efforts have been made to develop SLs for thermoelectric applications owing to their low  $\kappa_L$ . [104–107] One benefit of the SL structure is the feasibility to tune its  $\kappa$  by controlling  $L_p$  or the interface conditions, e.g., roughness and species mixing.

Phonon transport in the cross-plane direction of a superlattice (SL) may manifest particle-like or wave-like characteristics depending on how far a phonon can transport coherently without losing its phase information. [108] If phase breaking happens

quickly, for instance, before a phonon travels through one period ( $L_p$ ) of the SL, both the phonon propagation in each layer and the transmission/reflection at each individual interfaces will be similar to those in a single-interface heterojunction regardless of the SL structure. In this case, phonons are incoherent and can be treated as particles. In contrast, if a phonon can transport coherently over a distance of several  $L_p$ 's, phonon interference due to multiple reflections at the periodic interfaces leads to new phonon spectra. In such case, the wave nature of phonons should be considered. In the particle-like regime,  $\kappa$  increases with increasing  $L_p$  due to the reduction in the density of interfaces that hinder phonon transport. In contrast,  $\kappa$  decreases with increasing  $L_p$  due to reduced group velocities and enlarged band gaps when the wave-like behavior dominates. [109,110] The coexistence of these two opposite trends, i.e.,  $\kappa$  first decreases and then increases with increasing  $L_p$  in a single  $\kappa$ - $L_p$  curve, has been observed in experiments and numerical studies, [111–117] and the minimum  $\kappa$  was proposed as a signature of the transition between the wave-regime and the particle-regime. [111] However,  $\kappa$  was found to increase monotonically with increasing  $L_p$  in most experiments, [118–120] implying a predominance of incoherent phonon transport. The presence of interface roughness or species mixing was proposed to cause the disappearance of coherent phonon heat transfer characteristics, [113,121,122] and these defects were also seen as opportunities for reducing the  $\kappa$  of SLs. [113,123] The properties of specific coherent phonon modes have been measured experimentally, [124] while the importance of coherent phonons to the overall thermal transport has only recently been addressed by Luckyanova et al.'s experiment. [125] In their work,  $\kappa$  was found to increase almost linearly with the total length of AlGaAs/GaAs SLs at 30-297 K, which was attributed to coherent phonon conduction. The trend that  $\kappa$  increases with increasing SL length has been observed in previous molecular dynamics simulations, [115,121,122,126,127] but little attention was paid to the role played by coherent phonons. It is reasonable to expect that coherent phonons are the dominant heat carriers in long SLs as those in Luckyanova et al.'s experiment, and mechanisms that suppress the transport of coherent phonons should be effec-



tive in reducing  $\kappa$ . The transport of various other types of waves, e.g., electron and photon, can be substantially suppressed in disordered systems due to Anderson localization. [128–131] The localization of phonons in low-dimensional disordered media was also studied, [132–135] however, inadequate attention was paid to the overall thermal transport properties of 3D systems. [136]

In previous computational studies on SL, phonons were either treated incoherently [137,138] or coherently [109,111,114,116]. Taking a binary SL composed of alternating layers of material A and B as an example, the incoherent treatment assumes that all phonons propagate across distinct A and B layers successively and transmit/reflect at the A/B or B/A interfaces in a similar way as a single interface between A and B. In contrast, the coherent approach acquires phonon properties from the superlattice phonon spectra corresponding to a large unit cell (UC) composed of one layer of A and one layer of B. However, both methods have their own drawbacks. The incoherent approach cannot explain the trend that  $\kappa$  may decrease with increasing  $L_p$  as observed in MD simulations, while the coherent treatment contradicts the fact that the phase-breaking length, or the coherence length ( $L_\phi$ ) of some phonons may be comparable to or shorter than  $L_p$ . Accordingly, we argue that a more accurate discription of phonons in SL should consider the coexistence of incoherent phonons that retain the properties of A and B materials and have short  $L_\phi$  in terms of  $L_p$ , and coherent ones possessing properties arising from the new large UC of the SL and can travel without phase breaking over a distance of several  $L_p$ 's.

In this work, we investigate the thermal transport in binary SLs and random multilayers (RML), i.e., alternating A and B layers of random thickness, using nonequilibrium molecular dynamics (NEMD) simulations. We build a model considering the coexistence of coherent phonons and incoherent phonons in SL or RML to intreprete our NEMD results, and explore the properties of coherent and incoherent phonons in these multi-layer structures. Perfect SL and RML are an ideal pair of systems for isolating the contribution of coherent phonons and incoherent ones to heat transfer. With the same total length and average layer thickness, SL and RML should have ap-

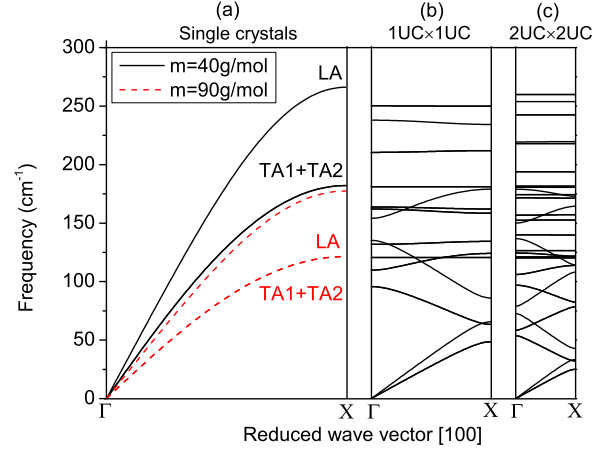


Figure 4.1. Phonon dispersions along the [100] direction. (a) LJ crystals ( $\epsilon = 16\epsilon_{Ar}$ ) with atomic masses of  $m = 40$  g/mol (m40) and  $m = 90$  g/mol (m90). (b) A SL built from repetitions of 1 UC thick of m40 layer and 1 UC thick of m90 layer (1UC $\times$ 1UC) along the [100] direction. (c) A 2UC $\times$ 2UC SL.

proximately the same scattering rate of incoherent phonons due to the same interface density, while coherent phonons are localized in long RMLs and thereby their contribution to  $\kappa$  can be neglected. As a consequence, the difference in thermal transport properties between a SL and the corresponding RML gives a good estimation of the contribution by coherent phonons in the SL.

This chapter is organized as follows. Section 4.2 describes the setup of our MD simulations and model structures. In Section 4.3, we propose a two-phonon model considering the coexistence of coherent and incoherent phonons in SL and RML. In Section 4.4, we present our simulation results and interpret them with our two-phonon model. Finally, we conclude this chapter in Section 4.5.

## 4.2 Methodology

### 4.2.1 Simulation Setup

We conduct NEMD simulations on conceptual atomic systems in which the interatomic interactions are modeled by the Lennard-Jones (LJ) potential,

$$\phi_{ij}(r_{ij}) = 4\epsilon \left[ \left( \frac{\sigma}{r_{ij}} \right)^{12} - \left( \frac{\sigma}{r_{ij}} \right)^6 \right], \quad (4.4)$$

where  $\phi_{ij}$  and  $r_{ij}$  are the pairwise interaction potential energy and the distance between atoms  $i$  and  $j$ , and  $\sigma$  and  $\epsilon$  are the zero-potential-energy pair separation and the potential well depth, respectively. LJ systems have been widely used in conceptual studies owing to their lower computational cost than many other potential forms, as well as the simplicity in independently controlling the lattice constant (by  $\sigma$ ) and the interatomic interaction strength (by  $\epsilon$ ). The parameter set of  $\sigma_{Ar} = 0.34$  nm,  $\epsilon_{Ar} = 0.0104$  eV and a cutoff radius of  $2.5\sigma_{Ar}$  have been adopted in previous studies on solid argon. [139, 140] A higher  $\epsilon$  in LJ systems corresponds to a longer phonon mean free path (MFP), thus enabling us to study the effect of MFP on thermal properties. We will study two types of LJ systems, i.e., one with  $\epsilon = 4\epsilon_{Ar}$  and the other with  $\epsilon = 16\epsilon_{Ar}$  for the interaction between all atoms, which will be referred to as LJ04 $\epsilon_{Ar}$  and LJ16 $\epsilon_{Ar}$ , respectively. The zero-potential-energy pair separation and the cutoff radius are  $\sigma_{Ar}$  and  $2.5\sigma_{Ar}$  for all LJ systems studied in this work.

The binary LJ systems studied in this work have two types of atomic masses, i.e.,  $m_A = 40.0$  g/mol and  $m_B = 90.0$  g/mol, which will be referred to as m40 and m90. Figure 4.1a shows the phonon dispersions of the LJ16 $\epsilon_{Ar}$ -m40 and LJ16 $\epsilon_{Ar}$ -m90 crystals, and Figs. 4.1b and c show those of a LJ16 $\epsilon_{Ar}$ -m40-m90 SL which is built from alternating layers of 1 UC thick m40 and 1 UC thick m90 (1UC $\times$ 1UC) and those of a 2UC $\times$ 2UC SL, respectively. As we can see, the phonon bands are flatter in the SL than in m40 and m90 crystals, and SL with thicker layers (2UC $\times$ 2UC) has flatter bands than that with thinner layers (1UC $\times$ 1UC).

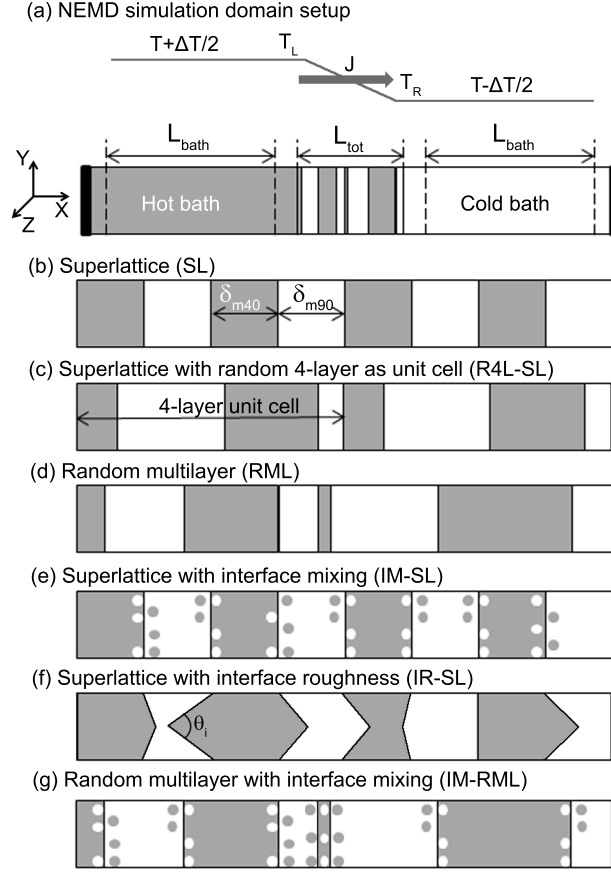


Figure 4.2. (a) Schematic of the simulation domain setup in this work.  $L_{bath}$  is the length of the heat bath and  $L_{tot}$  is the total length of the device. The hot (cold) bath is maintained at  $T + \Delta T/2$  ( $T - \Delta T/2$ ).  $T_L$  and  $T_R$  are the steady-state local temperature at the buffer regions next to the two ends of the device.  $J$  is the steady-state heat current. (b) Superlattice made of alternating layers of m40 and m90 with layer thickness  $\delta_{m40}$  and  $\delta_{m90}$ , respectively. (c) Superlattice of which the UC is a random 4-layer (R4L-SL). (d) Random multilayer (RML). (e) Superlattice with interface mixing (IM-SL). (f) Superlattice with interface roughness (IR-SL). (g) Random multilayer with interface mixing (IM-RML).

The simulation domain setup is shown in Fig. 4.2a. The device of length  $L_{tot}$  is sandwiched between two heat baths of length  $L_{bath}$ , and  $\sim 1$  nm thick of atoms (the dark regions) at the two ends are frozen to work as the fixed boundary condition (bc). We leave two 8.4 nm long buffer regions between the device and each of the two heat baths to extract the temperature at the two ends of the device, i.e.,  $T_L$  and  $T_R$ , as shown in Fig. 4.2a. The thermal conductance  $G$  of the system is computed as  $G = J/[A(T_L - T_R)]$ , where  $A$  is the cross-sectional area of the device and  $J$  is the steady-state heat current, i.e., the amount of kinetic energy artificially injected into (extracted from) the hot (cold) heat bath per unit time. Then  $\kappa$  can be calculated as  $\kappa = GL_{tot}$ . We use  $\Delta t = 2$  fs and  $\Delta t = 1$  fs for the LJ04 $\epsilon_{Ar}$  and LJ16 $\epsilon_{Ar}$  systems as the simulation time step size based on the criteria given in Ref. 139, i.e.,  $\Delta t \approx 0.002\sqrt{\sigma^2 m/\epsilon}$ .

Our NEMD simulations (at temperature  $T$ ) are conducted in the following process. (1) the periodic bc is applied to all three directions ( $X$  as the length direction,  $Y$  and  $Z$  as the lateral directions) and each atom is given a random velocity vector based on the Gaussian distribution function with a mean of 0 and a variance corresponding to a temperature of 5 K. (2) the entire supercell is relaxed in the NPT ensemble targeted at zero pressure and temperature  $T$  for 200 ps. (3) the entire supercell is relaxed in the NPT ensemble at zero pressure and temperature  $T$  for 300 ps. (4)  $\sim 1$  nm layer of atoms at both ends of the supercell are frozen and kept so, which is equivalent to applying the fixed bc to the  $X$  direction. (5) the simulation is switched to NVE integrations except that the velocities of the atoms in the two heat bath regions are rescaled to a temperature of  $T + \Delta T/2$  or  $T - \Delta T/2$  every simulation step and the atoms in the fixed boundary regions are frozen. Step (5) lasts 10-40 ns depending on the length of the supercell to ensure that the NEMD simulation reaches steady state. Longer supercells need longer time to reach steady state.

### 4.2.2 Model Structures

Figures 1b-g show the model structures composed of 50% m40 atoms and 50% m90 atoms. The model structures are constructed by the stacking of face-centered-cubic UCs along the [100] direction. The SL is created from periodic repetition of m40 and m90 layers of constant thickness  $\delta_{m40}$  and  $\delta_{m90}$ , i.e.,  $\delta_{m40/m90,i} = \delta_{m40/m90,j}$ . Accordingly,  $L_p = 2\delta_{m40} = 2\delta_{m90}$  in this work. However, if the repetition happens every four layers, i.e.,  $\delta_{m40/m90,i} \neq \delta_{m40/m90,i+1}$  but  $\delta_{m40/m90,i} = \delta_{m40/m90,i+2}$ , then it is a SL with a random 4-layer as UC (R4L-SL), similar to the SLs with complex UCs in Ref. 139. If the thicknesses of m40 and m90 layers are totally randomized, a SL becomes a random multilayer (RML). The order of randomness in RML can be controlled by setting an upper limit to the deviation ( $|\Delta\delta|$ ) of  $\delta_i$  from the average thickness  $\delta$ . Take an RML with  $\delta = 8$  UC for example,  $\delta_i$  can only be 7, 8 and 9 UC if we enforce  $|\Delta\delta| \leq 1$  UC, but it can be 6-10 UC (more randomized) when  $|\Delta\delta| \leq 2$  UC. In this work, RMLs without an upper limit of  $|\Delta\delta|$ , which is the totally randomized case, will be referred to as RML and those with an upper limit will be denoted as “RML,  $|\Delta\delta| \leq N$  UC”. A comparison between SL, R4L-SL and RMLs with different degrees of randomness in  $\delta$  can reveal the effect of randomness in  $\delta$  on thermal transport properties of multi-layer structures.

As a comparison with RMLs, we will also study SLs with interface mixing (IM-SL) and those with interface roughness (IR-SL), of which the schematic structures are shown in Fig. 4.2e and 4.2f, respectively. Interface mixing, sometimes called interface alloying, can happen at different levels: the weakest case is that only one atomic layer at the end of the m40 layer is mixed with the adjacent one atomic layer of m90; while the strongest case is when the whole SL becomes a homogeneous alloy. Interface roughness is characterized by the angle  $\theta$ 's shown in Fig. 4.2f. If the  $\theta$ 's of all interfaces are the same, the structure is still periodic and hence remain as a SL. If the  $\theta$ 's are different and random, the wavy interfaces are more like realistic roughness despite that there are usually voids at the interface.

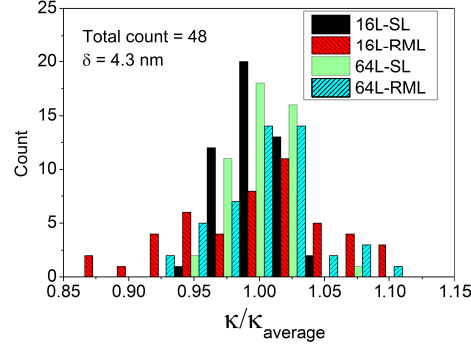


Figure 4.3. Histogram of  $\kappa$  normalized by the corresponding average for 48 individual samples for SLs with 16 layers (16L-SL), RMLs with 16 layers (16L-RML), SLs with 64 layers (64L-SL) and RMLs with 64 layers (64L-RML), of which the average layer thickness  $\delta = 4.3$  nm.

### 4.2.3 Convergence Study

Table 7.1 lists the effect of heat bath length  $L_{\text{bath}}$ , temperature bias  $\Delta T$  and cross-sectional area  $A$  on the thermal conductivity prediction for LJ04 $\epsilon_{Ar}$  and LJ16 $\epsilon_{Ar}$  SLs. The SL has a total length  $L_{\text{tot}} = 137$  nm and a uniform layer thickness  $\delta = 4.3$  nm. Notably, the predicted  $\kappa$  increases with  $L_{\text{bath}}$  and saturates when  $L_{\text{bath}} = 33.8$  nm for LJ04 $\epsilon_{Ar}$  and when  $L_{\text{bath}} = 270.2$  nm for LJ16 $\epsilon_{Ar}$ . Beyond these lengths,  $\kappa$  does not depend on the length of the heat bath, which can be viewed as semi-infinite in terms of heat transfer and they are used in our simulations. Based on Table 7.1, we use  $A = 6 \text{ UC} \times 6 \text{ UC}$  and  $\Delta T = 6$  K. Another scheme for NEMD calculation of  $\kappa$  is by applying a constant heat current and measure the resulting  $\Delta T$ , which has been used in previous studies on SLs. [122, 127, 139, 141]. The  $\kappa$  predicted from this method is  $\kappa = 5.43 \text{ W/m-K}$  when  $L_{\text{bath}} = 270.2$  nm,  $\epsilon = 16\epsilon_{Ar}$ ,  $A = 6 \text{ UC} \times 6 \text{ UC}$ , and the measured  $\Delta T$  is approximately 5.4 K, which is in good agreement with the constant  $\Delta T$  scheme used by us.

Table 4.1. The effect of heat bath length  $L_{bath}$ , temperature bias  $\Delta T$  and cross-sectional area  $A$  on the prediction of the thermal conductivity  $\kappa$  of LJ04 $\epsilon_{Ar}$  and LJ16 $\epsilon_{Ar}$  SLs with layer thickness  $\delta = 4.3$  nm and total device length  $L_{tot} = 137$  nm at  $T = 30$  K.

$\epsilon$ ( $\epsilon_{Ar}$ )	$\Delta T$ (K)	$L_{bath}$ (nm)	$A$ (UC $\times$ UC)	$\kappa$ (W/m-K)
4	6.0	16.9	$6 \times 6$	1.29
4	6.0	33.8	$6 \times 6$	1.37
4	6.0	67.6	$6 \times 6$	1.34
4	6.0	33.8	$9 \times 9$	1.34
4	10.0	33.8	$6 \times 6$	1.38
16	6.0	67.6	$6 \times 6$	4.52
16	6.0	135.1	$6 \times 6$	5.24
16	6.0	270.2	$6 \times 6$	5.54
16	6.0	405.3	$6 \times 6$	5.50
16	6.0	270.2	$4 \times 4$	5.75
16	6.0	270.2	$9 \times 9$	5.62
16	10.0	270.2	$6 \times 6$	5.79



#### 4.2.4 Simulation Uncertainty

To quantify the uncertainty associated with our NEMD simulations, we conduct 48 individual simulations for SLs with 16 layers (16L-SL), RMLs with 16 layers (16L-RML), SLs with 64 layers (64L-SL) and RMLs with 64 layers (64L-RML), of which the average layer thickness  $\delta = 4.3$  nm. The histogram of the computed  $\kappa$ 's normalized by their average are shown in Fig. 4.3. The uncertainty is defined as the standard deviation of  $\kappa$  normalized by the average  $\kappa$ , which are 2.2%, 5.7%, 2.3% and 3.8% for 16L-SL, 16L-RML, 64L-SL and 64L-RML, respectively. There are several sources of uncertainty in our NEMD simulations. For SLs, the uncertainty comes from the statistical nature of molecular dynamics, where the difference in initial conditions and process can lead to slightly different results. However, a RML can have different configurations due to the many possible arrangements of  $\delta_i$ 's for given  $L_{tot}$  and  $\delta$ . Such variation in  $\delta_i$ 's may add to the uncertainty. As we can see in Fig. 4.3 as well as the normalized standard deviations mentioned above, the simulated  $\kappa$ 's of RMLs are more dispersed than those of SLs. The uncertainty is even larger for RMLs with less layers (16L-RML) than those with more layers (64L-RML). The reason is that there is a higher chance that 64L-RML is fully randomized than 16L-RML, and  $\kappa$  depends considerably on the degree of randomness in  $\delta$  when  $\delta$  is not fully randomized, which will be demonstrated later.

#### 4.3 Two-phonon Model

Previous studies on SLs either treat all phonons as incoherent particles possessing properties of individual layers or as coherent waves with properties determined by the superlattice phonon spectra. Herein we will demonstrate that both approaches are special cases of a more general model, which accounts for the coexistence of coherent and incoherent phonons in one system. In such two-phonon model, we divide phonons in a SL into two groups, i.e., incoherent ones with the phonon spectra of individual

m40 and m90 layers as shown in Fig. 4.1a, and coherent ones with the superlattice phonon spectra as those in Fig. 4.1b and c.

Thermal conductance is related to MFP  $\lambda$  by [142]

$$G = G_0 \frac{\lambda}{\lambda + L_{tot}}, \quad (4.5)$$

where the subscript 0 indicates ballistic-limit quantity. Correspondingly, thermal conductivity  $\kappa$  is

$$\kappa = GL_{tot} = G_0 \frac{\lambda L_{tot}}{\lambda + L_{tot}}, \quad (4.6)$$

which indicates that  $\kappa$  increases almost linearly with the total length when  $L_{tot} \ll \lambda$  (ballistic regime) while it saturates at a constant value when  $L_{tot} \gg \lambda$  (diffusive regime). Such relation has been employed for phonon transport to compute the  $\kappa$  of silicon and  $\text{Bi}_2\text{Te}_3$  and good agreement with experiment was achieved. [143, 144]

By treating the coherent phonons and incoherent phonons as gray media, the thermal conductance  $G$  of SL can be expressed as

$$\begin{aligned} G_{SL} &= G_{coh} + G_{inc} \\ &= G_{coh,0} \frac{\lambda_{coh}}{\lambda_{coh} + L_{tot}} + G_{inc,0} \frac{\lambda_{inc}}{\lambda_{inc} + L_{tot}}, \end{aligned} \quad (4.7)$$

where the subscripts *coh* and *inc* denote coherent and incoherent phonon, respectively. In a random medium, e.g., RML, the Anderson localization of carriers would lead to exponential decay of  $G$  when  $L_{tot}$  increases. Noting that such localization works on coherent phonons only, we modify the first term in Eq. (4.7) to include an exponential,

$$\begin{aligned} G_{RML} &= G_{coh} + G_{inc} \\ &= G_{coh,0} \frac{\lambda_{coh}}{\lambda_{coh} + L_{tot}} \exp\left(-\frac{L_{tot}}{L_{loc}}\right) + G_{inc,0} \frac{\lambda_{inc}}{\lambda_{inc} + L_{tot}}, \end{aligned} \quad (4.8)$$

where  $L_{loc}$  is the localization length which describes how fast  $G$  decays in random media. As for the first term on the right hand side, the exponential decays much faster than  $\lambda_{inc}/(\lambda_{inc} + L_{tot})$  especially if  $\lambda_{coh} > L_{loc}$ . Therefore, the latter can be approximated as unity and Eq. (4.8) becomes

$$\begin{aligned} G_{RML} &= G_{coh} + G_{inc} \\ &= G_{coh,0} \exp\left(-\frac{L_{tot}}{L_{loc}}\right) + G_{inc,0} \frac{\lambda_{inc}}{\lambda_{inc} + L_{tot}}. \end{aligned} \quad (4.9)$$

When  $L_{tot}$  is large, the exponential term in Eq. (4.9) can be neglected as it decays much faster than the second term on the right hand side, i.e., coherent phonon contribution is negligible. Therefore,

$$G_{RML, L_{tot} \gg L_{loc}} \approx G_{inc} = G_{inc,0} \frac{\lambda_{inc}}{\lambda_{inc} + L_{tot}}. \quad (4.10)$$

For short RMLs, there may still be noticeable contribution of  $G$  from coherent phonons, which can be obtained by subtracting Eq. (4.10) from Eq. (4.9),

$$G_{coh, RML} = G_{coh,0} \exp\left(-\frac{L_{tot}}{L_{loc}}\right). \quad (4.11)$$

With the same  $L_{tot}$  and  $\delta$ , SL and RML have the same interface density; therefore, the scattering rates of incoherent phonons should be approximately the same in SL and RML. This is different from IM-SL and IR-SL in which mass difference or roughness scatters both coherent and incoherent phonons. Subtracting Eq. (4.10) ( $G$  of RML) from Eq. (4.7) ( $G$  of SL), we can get the  $G$  contributed solely by coherent phonons in SL, which is

$$G_{coh, SL} = G_{SL} - G_{inc} = G_{coh,0} \frac{\lambda_{coh}}{\lambda_{coh} + L_{tot}}. \quad (4.12)$$

It is worth mentioning that as Eq. (4.12) is deducted from Eq. (4.10), the validity of Eq. (4.12) only holds when  $L_{tot} \gg L_{loc}$  ( $L_{tot} = 3L_{loc}$  ensures more than 95% reduction in  $G_{coh}$  in RMLs).

## 4.4 Results and Discussions

### 4.4.1 Effect of Random Layer Thickness

Figures 4.4a and 4.4b show the fitting of our simulation data in the  $L_{tot} \gg L_{loc}$  regime (the values of  $L_{loc}$  will be presented later) with the two-phonon model depicted by Eqs. 4.7-4.12. Through the model fitting, we obtain  $G_{inc,0} = 225.7 \text{ MW/m}^2\text{-K}$ ,  $\lambda_{inc} = 13.1 \text{ nm}$ ,  $G_{coh,0} = 26.9 \text{ MW/m}^2\text{-K}$  and  $\lambda_{coh} = 327.3 \text{ nm}$  for LJ16 $\epsilon_{Ar}$  systems, and  $G_{inc,0} = 104.8 \text{ MW/m}^2\text{-K}$ ,  $\lambda_{inc} = 13.1 \text{ nm}$  for LJ04 $\epsilon_{Ar}$  ones. It is difficult to

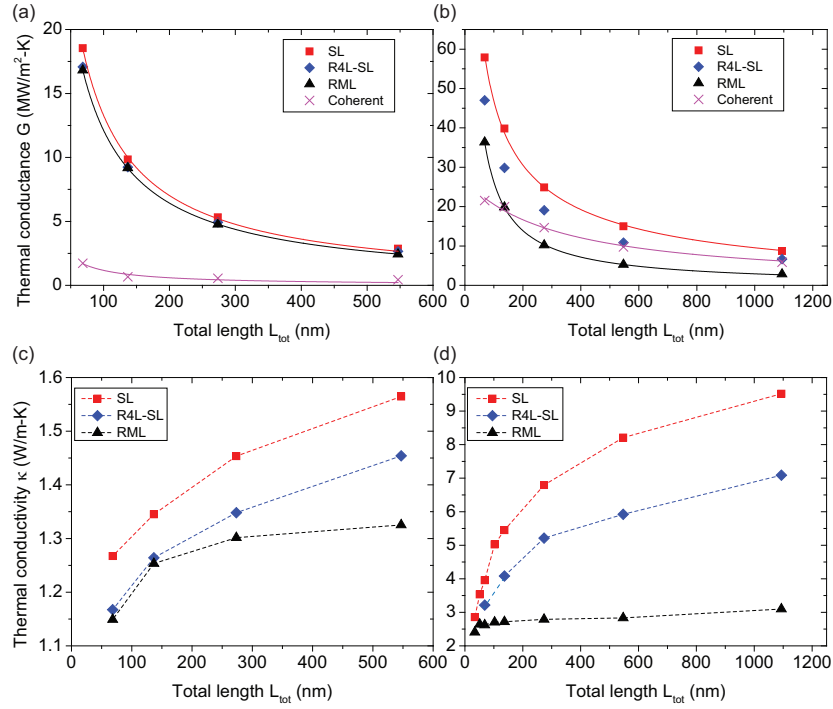


Figure 4.4. (a) and (b):  $G$  of SL, R4L-SL and RML as a function of  $L_{tot}$  for LJ04 $\epsilon_{Ar}$  systems (a) and LJ16 $\epsilon_{Ar}$  ones (b), and the solid lines are fitting curves based on Eq. (4.7) and Eq. (4.10). (c) and (d):  $\kappa$  of SL, R4L-SL and RML as a function of  $L_{tot}$  for LJ04 $\epsilon_{Ar}$  systems (c) and LJ16 $\epsilon_{Ar}$  ones (d), respectively, and the dashed lines are guides for the eyes. For all cases, The average layer thickness  $\delta = 4.3$  nm.

extract credible  $G_{coh,0}$  and  $\lambda_{coh}$  for LJ04 $\epsilon_{Ar}$  systems due to the considerably large fluctuation in the data for  $G_{coh}$ . The above values are physically reasonable in the following aspects. First,  $G_{inc,0} \gg G_{coh,0}$ . This is because a phonon must satisfy at least two conditions to be coherent, that is, satisfying the phonon dispersion of the SL and the coherence length  $L_\phi$  extends several layers, while it just needs to satisfy the dispersion of the material of the layer it stands in to be incoherent. Consequently, there should be more incoherent phonons than coherent ones in a SL. Besides, the group velocities of coherent phonons (slope of the dispersion curves in Fig. 4.1b and c) are generally lower than those of incoherent phonons (slope of the dispersion curves in Fig. 4.1a). As the ballistic conductance is proportional to the number of phonons and their group velocity, it is reasonable to find a lower  $G_{coh,0}$  than  $G_{inc,0}$ . Second,  $\lambda_{coh} \gg \lambda_{inc}$ . This is reasonable considering that incoherent phonons suffer a lot of interface scatterings owing to the high interface density, while coherent phonons barely see the interfaces and are only scattered by intrinsic processes such as mini-band Umklapp scatterings. [145]

Figures 4.4c and 4.4d show the  $\kappa$  of SL, R4L-SL and RML as a function of  $L_{tot}$ . As we can see, the  $\kappa$  of all these structures increases with the total length. Such trend has been observed experimentally by Luckyanova et al. in GaAs/AlAs SLs and was attributed to coherent phonons which see the SL as a new crystalline material. [125] In particular,  $\kappa$  increases almost linearly with  $L_{tot}$  when  $L_{tot} < 100$  nm in Fig. 4.4d, and similarly in Luckyanova et al.'s experiment. Similar size effect has been observed in NEMD simulations on single crystals [37] and SLs, [115, 121, 122, 126, 127] and the analytical model  $\kappa^{-1} \propto (\lambda_\infty^{-1} + L_{tot}^{-1})$  was usually adopted to rationalize it, where  $\lambda_\infty$  is the bulk-limit intrinsic phonon MFP of the material. Comparing Figs. 4.4c and 4.4d, the increase in  $\kappa_{SL}$  is much slower in LJ04 $\epsilon_{Ar}$  SLs than in LJ16 $\epsilon_{Ar}$  ones, indicating larger  $\lambda_\infty$  in the latter. If we compare the  $\kappa$  of SL, R4L-SL and RML, it is apparent that  $\kappa$  decreases as the randomness in layer thickness  $\delta$  increases, which agrees with previous studies. [139, 146] Specifically, Landry et al. [139] showed that SLs with complex UCs of more than two layers have lower  $\kappa$  than those with simple UCs of

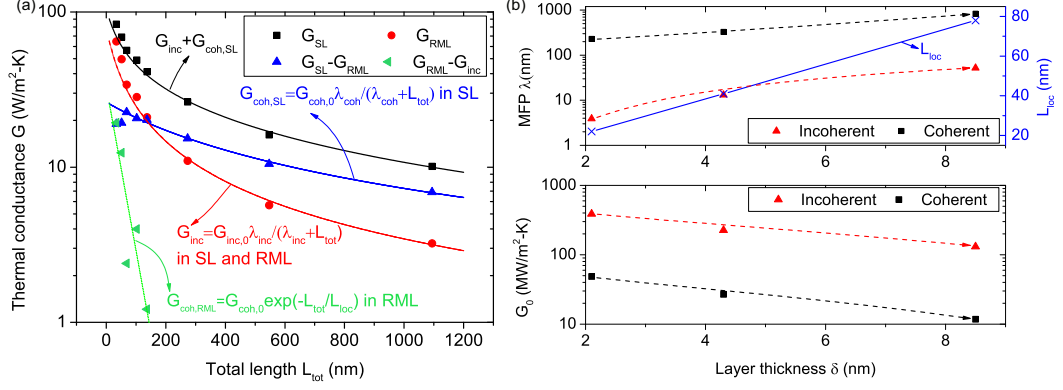


Figure 4.5. (a) Fitting of simulation data using the two-phonon model depicted by Eqs. 4.7-4.12. (b) Top panel: MFP  $\lambda$  of coherent phonons and incoherent phonons in SLs and the localization length  $L_{loc}$  of coherent phonons in RMLs; bottom panel: ballistic-limit thermal conductance  $G_0$  of coherent phonons and incoherent ones in SLs.

only two layers; Frachioni and White [146] reported lower  $\kappa$  of silicon-based RMLs than SLs. In Figs. 4.4c and 4.4d,  $\kappa$  of RML increases much more slowly than that of SLs and almost levels off, which results from the localization of coherent phonons in RMLs and will be discussed in detail later. We should also note that the randomness in  $\delta$  is more effective in reducing  $\kappa_{SL}$  for LJ16 $\epsilon_{Ar}$  systems than LJ04 $\epsilon_{Ar}$  ones, implying more prominent coherent phonon contribution to heat conduction in SLs composed of materials with longer phonon MFP. The underlying mechanism will be discussed in the following section.

In Fig. 4.5a, we fit our simulation data with Eqs. 4.7-4.12 in the following manner. (1) Eq. (4.10) and Eq. (4.12) are used to fit the data for  $G_{RML}$  and  $G_{SL} - G_{RML}$  in the range of  $L_{tot} > 200$  nm to get  $G_{coh,0}$ ,  $G_{inc,0}$ ,  $\lambda_{coh}$  and  $\lambda_{inc}$ . We enforce  $L_{tot} > 200$  nm since the utility of Eq. (4.12) requires the coherent phonon contribution to  $G_{RML}$  to be negligible ( $L_{tot} > 3L_{loc}$ ). In this step, the lines indicated as  $G_{coh,SL}$  and  $G_{inc}$  can be obtained. (2) Subtracting the  $G_{inc}$ 's obtained in step (1) from the data for  $G_{RML}$ 's, we can obtain a series of data  $G_{coh,RML}$  decaying exponentially (green left-pointing triangles in Fig. 4.5a). We can get  $L_{loc}$  by fitting the data for  $G_{coh,RML}$  with

Eq. (4.11). (3) The summation of  $G_{coh,SL}$  and  $G_{inc}$  gives  $G_{SL}$  according to Eq. (4.7), and the result (the dark line indicated as  $G_{inc} + G_{coh}$  in Fig. 4.5a) agrees well with the  $G_{SL}$ 's predicted from our simulations (dark squares), again demonstrating the applicability of our two-phonon model to multi-layer structures.

The top panel of Fig. 4.5b shows  $\lambda_{coh}$  and  $\lambda_{inc}$  in SLs (left Y-axis) or  $L_{loc}$  of coherent phonons in RMLs (right Y-axis) extracted using the fitting procedures illustrated above. We can see that  $\lambda_{inc}$  increases significantly with increasing  $\delta$ , which arises from decreased density of interfaces that hinder the forward propagation of incoherent phonons. Also,  $\lambda_{coh}$  is always larger than  $\lambda_{inc}$ . This is because the interfaces are lattice discontinuities for incoherent phonons while they are merely an essential part of the SL UC for coherent phonons.  $L_{loc}$  also increases with  $\delta$ , but it is shorter than 80 nm for all the  $\delta$ 's we studied. Therefore, the contribution of coherent phonons to  $G_{RML}$  is negligible in RMLs with  $L_{tot} > 200$  nm, and the validity of the step (1) of the above fitting procedures is confirmed. We need to point out that the wide spectrum of phonons implies that  $L_{loc}$  may not be the same for all phonon modes, so  $G_{RML} - G_{inc}$  do not necessarily decay exactly exponentially.

The bottom panel of Fig. 4.5b shows the ballistic-limit thermal conductance  $G_0$  as a function of  $\delta$  for coherent phonons in SL, and incoherent phonons in SL and RML. Notably,  $G_{coh}$  decreases quickly with increasing  $\delta$ . This is because the phonon group velocity decreases with increasing  $\delta$  due to zone folding, which has been illustrated in previous lattice dynamics studies. [109, 147]

#### 4.4.2 Transition between Coherent and Incoherent Behavior

In Section 4.3, we claimed that the coherence length  $L_\phi$  of phonons must extends several  $\delta$ 's so that enough phonon interferences can occur to form the superlattice phonon spectra for coherent phonons; otherwise the phonons primarily manifest themselves as incoherent particles. To provide evidence for this argument, we explore the correlation between  $\kappa_{SL} - \kappa_{RML}$  and  $L_\phi/\delta$  in this section.  $\kappa_{SL} - \kappa_{RML}$  quanti-

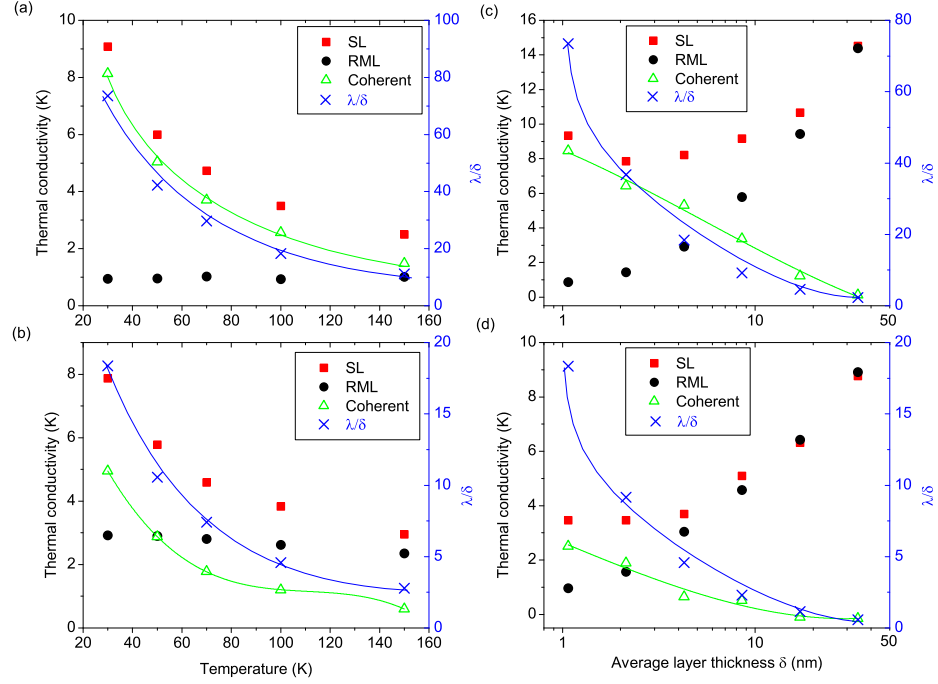


Figure 4.6. (a) and (b): Left Y-axis is for the thermal conductivity of SL, RML and the difference between them as a function of temperature; right Y-axis is for the ratio of MFP to average layer thickness as a function of  $T$ . (a) is for  $\delta = 1.1$  nm and (b) is for  $\delta = 4.3$  nm. (c) and (d): Left Y-axis is for the  $\kappa$  of SL, RML and the difference between them as a function of  $\delta$ ; right Y-axis is for  $\lambda/\delta$  as a function of  $T$ . (c) and (d) are for  $T = 30$  K and  $T = 100$  K, respectively. The solid lines are guides for the eyes.



fies coherent phonon contribution to heat conduction, while  $L_\phi/\delta$  specifies how many layers a phonon can transport through coherently. Our argument can be justified if a positive correlation can be found.

In pristine bulk crystalline materials, both the normal process and Umklapp process are inelastic and thereby can break the phase of phonons, while only the Umklapp process causes thermal resistance (momentum-breaking). But when there is roughness or other types of defect, which are usually more momentum-breaking than phase-breaking,  $L_\phi$  can be comparable to or longer than the MFP  $\lambda$ . [108] Herein we use  $\lambda$  to interpret the phase-breaking related phenomenon, i.e., the transition between coherent and incoherent behavior of phonons, based on the notion that  $L_\phi$  and  $\lambda$  should be positively correlated in SLs and RMLs with atomically smooth and planar interfaces.

We estimate the average group velocity as

$$\bar{v}^{-1} = \frac{v_{LA}^{-1} + 2v_{TA}^{-1}}{3}, \quad (4.13)$$

which considers the longitudinal acoustic branch (subscript LA) and the two degenerate transverse acoustic branches (TA).  $\lambda$  can be estimated from  $\lambda = 3\kappa/(c\bar{v})$ . Here  $c$  is the classical heat capacity of the LJ crystal, which is  $c = 3k_B n$  with  $k_B$  denoting the Boltzmann constant and  $n$  the atom number density. The lattice constant  $a$  of the LJ16 $\epsilon_{Ar}$  crystal is  $(5.278 \pm 0.008) \text{ \AA}$  in the temperature range studied here (30 K-150 K), so  $n = 4/a^3 \approx 2.72 \times 10^{28} \text{ m}^{-3}$  and hence  $c = 1.13 \times 10^6 \text{ J/m}^3\text{-K}$ .  $v_{LA}$  and  $v_{TA}$  are estimated as the Brillouin zone center group velocity of the corresponding branches in Fig. 4.1a, and we get  $v_{LA,m40} = 4135 \text{ m/s}$ ,  $v_{TA,m40} = 3053 \text{ m/s}$ ,  $v_{LA,m90} = 2748 \text{ m/s}$  and  $v_{TA,m90} = 2039 \text{ m/s}$ . Finally, the average  $\lambda$  of m40 and m90 crystals are taken as  $\lambda^{-1} = \lambda_{m40}^{-1} + \lambda_{m90}^{-1}$ .

Figures 4.6a and 4.6b show  $\kappa$  (left Y axis) and  $\lambda/\delta$  (right Y axis) as a function of temperature for  $\delta = 1.1 \text{ nm}$  and  $\delta = 4.3 \text{ nm}$ , respectively.  $\lambda$  decreases with increasing  $T$  due to enhanced Umklapp scatterings, and hence the ratio  $\lambda/\delta$  decreases. In each panel, the difference between the  $\kappa$  of SL and that of RML, which is attributed to coherent phonons, decreases as  $T$  rises. The reason is that the phase of

phonons breaks more quickly with enhanced inelastic scatterings at higher  $T$ , and, as a consequence, more coherent phonons transform into incoherent ones. As there are less coherent phonons than incoherent ones, and incoherent phonons have much shorter MFP (Fig. 4.5b), the above transformation cannot cause significant increase in  $\kappa_{inc}$  (or  $\kappa_{RML}$ ). As a result, there is no notable increase in the  $\kappa$  of RMLs when  $T$  increases even though coherent phonons are transforming into incoherent ones.

In Figs. 4.6c and d,  $\kappa$  is plotted as a function of  $\delta$ . It is clear that the difference between  $\kappa_{SL}$  and  $\kappa_{RML}$  decreases with increasing  $\delta$ . Larger  $\delta$  means more phase-breaking scatterings before a phonon propagates from one interface to the next, which transforms coherent phonons into incoherent ones. The extreme case is when  $\delta$  is so large that all phonons behave incoherently and thereby  $\kappa_{SL} = \kappa_{RML}$ . In addition,  $\kappa_{RML}$  increases substantially with increasing  $\delta$  owing to decreased interface density. Similar trend was also reported for SLs with interface mixing or roughness, indicating a predominance of incoherent phonons. [122, 137] In Figs. 4.6a-d, the  $\kappa$  contributed by coherent phonons (unfilled triangles) is positively correlated with the ratio  $\lambda/\delta$  (crosses), supporting our argument mentioned at the beginning of this section.

Recall that in Section 4.4.1 and Fig. 4.5b, we estimated the ballistic-limit thermal conductance  $G_0$  and the intrinsic MFP  $\lambda$  of coherent and incoherent phonons in SLs, and found  $G_{0,coh} \ll G_{0,inc}$  and  $\lambda_{coh} \gg \lambda_{inc}$ . Accordingly, the  $\kappa$ - $\delta$  relation in SLs as shown in Figs. 4.6c and d can be understood in this way — the decreasing trend for small  $\delta$ 's is caused by the fast decrease in  $G_{0,coh}$  owing to the quickly reduced  $v_g$ , while the increasing trend for large  $\delta$ 's is caused by the increase in  $\lambda_{inc}$  owing to the reduced interface density.

#### 4.4.3 Thermal Boundary Resistance of Individual Interfaces in SL and RML

In Section 4.4.1, we have considered the SL or RML as a homogeneous device and studied the overall  $\kappa$  or  $G$  of the device. In this section, we will evaluate how the

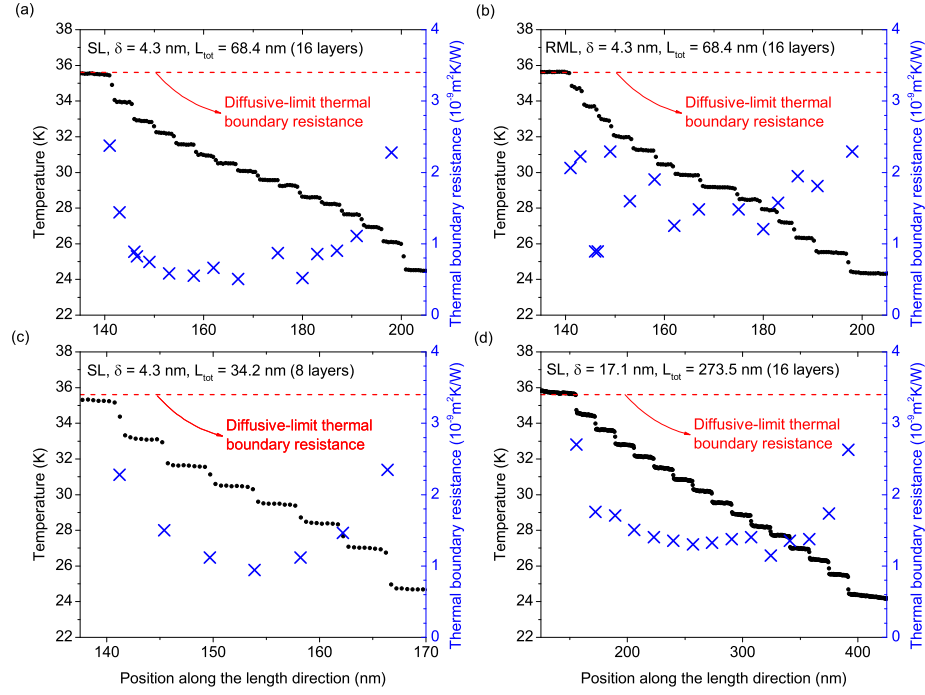


Figure 4.7. Temperature profiles (left Y-axis) and the thermal boundary resistances of each individual interface (right Y-axis) for: (a) a SL with  $\delta = 4.3 \text{ nm}$  and  $L_{\text{tot}} = 68.4 \text{ nm}$ ; (b) a RML with  $\delta = 4.3 \text{ nm}$  and  $L_{\text{tot}} = 68.4 \text{ nm}$ ; (c) a SL with  $\delta = 4.3 \text{ nm}$  and  $L_{\text{tot}} = 34.2 \text{ nm}$ ; (d) a SL with  $\delta = 17.1 \text{ nm}$  and  $L_{\text{tot}} = 273.5 \text{ nm}$ . The red dashed lines show the diffusive limit of the thermal boundary resistance, i.e.,  $3.4 \times 10^{-9} \text{ m}^2 \text{ K/W}$ .

thermal boundary resistance,  $R_i = 1/G_i$ , of each individual interface  $i$  varies with the position of interfaces as well as structural parameters such as  $\delta$  and  $L_{tot}$ .

Figures 4.7a-d show the temperature profiles (dots) and thermal boundary resistance  $R_i$  (crosses) of individual interfaces obtained from our NEMD simulations.  $R_i$  is computed as  $R_i = A\Delta T_i/J$  and plotted with respect to the right Y-axis, where  $\Delta T_i$  is the temperature drop at the  $i$ th interface.

Comparing Fig. 4.7a and Fig. 4.7b, which are for a SL and a RML respectively, we can see that  $R$ 's of the interfaces in the RML are generally higher than those in the corresponding SL. This is because both coherent and incoherent phonons transfer heat in the SL while coherent ones are localized in the RML. In Fig. 4.7a, we can see that  $R_i$  is almost constant ( $R_i \approx 0.7 \times 10^{-9} \text{ m}^2\text{K/W}$ ) in the central region of the SL, but  $R_i \approx 2.4 \times 10^{-9} \text{ m}^2\text{K/W}$  for the interfaces at the end of the SL (closest to the heat baths). Similar observations have been made by Samvedi and Tomar on Si/Ge SLs, and the higher  $R$  of the interfaces closest to the heat baths was attributed to the filtering of phonons that originate from the heat bath but are not coherent in the SL, i.e., not following the phonon dispersion of the SL. [126] The nearly uniform  $R$ 's shown in Fig. 4.7b support such explanation, as coherent phonons are negligible in RMLs. In SLs, we expect phonons to show stronger incoherent characteristics, manifested as a higher  $R$ , near the ends of the SL than near the center. In SLs with many periods,  $R$  will decrease from the ends to the center and level off as shown in Fig. 4.7a and d; while in short SLs,  $R$  may keep decreasing till the center of the SL, as shown in Fig. 4.7c. Therefore, we expect stronger coherent phonon characteristics in longer SLs than in shorter ones. The nonuniform  $R$ 's in SLs indicate that our homogeneous treatment of SLs, especially short ones, may induce certain amount of errors.

The diffusive-limit thermal boundary resistance  $R_s$  is obtained from NEMD simulations on single-interface heterojunctions of m40 and m90 crystals, where long enough m40 and m90 sides are used so that  $R$  does not change with increasing system length. Figures 4.7a-d show that the  $R$ 's of individual interfaces are lower than the bulk limit

$R_s$  of  $3.4 \times 10^{-9}$  m<sup>2</sup>K/W. Figure 4.7c (for a SL with  $\delta = 4.3$  nm) and Fig. 4.7d (for a SL with  $\delta = 17.1$  nm) reveal that  $R_i$ 's are generally higher in SLs with thicker layers. Similar behaviors were observed in Si/Ge systems, where a thin Si (or Ge) film was sandwiched between two Ge (or Si) substrates. [110] The total thermal resistance of the thin film plus the two interfaces was found to increase with the film thickness until it reaches the diffusive limit in Ref. 110.

One may think that the  $\kappa$ - $L_{tot}$  relation in Figs. 4.4c and 4.4d contradicts the temperature profiles in Figs. 4.7a, 4.7c and 4.7d for SLs: on one hand, the notable increase in  $\kappa$  with  $L_{tot}$  seems to indicate a ballistic thermal transport regime; on the other hand, there is no temperature discontinuity at the interface between the heat baths and the device, exhibiting diffusive thermal transport feature. To understand such “contradiction”, we should note that as there are more incoherent phonon modes in the device as explained in Section 4.4.1, incoherent phonons dominate the heat capacity and hence the temperature profile. As they have short MFP ( $\lambda_{inc} \ll L_{tot}$ ), the temperature profile thus shows a diffusive feature. On the other hand, coherent phonons dominate thermal transport and they have long MFP, therefore  $\kappa$  keeps increasing with  $L_{tot}$ , showing a ballistic feature.

#### 4.4.4 Comparison between the Effect of Random Layer Thickness, Interface Mixing, and Interface Roughness

The scattering and localization of phonons in SL and RML with perfect interfaces or with interface defects can be qualitatively described by the phase diagrams plotted in Figs. 4.8a-d. As shown in Fig. 4.8a, we categorize phonons in a SL into four groups. (I) lw-coh: coherent phonons (coh) of which the coherence length extends several layers, and the wavelength is longer than the characteristic size of interface defects (lw) so that they can propagate through the defects without being scattered. (II) sw-coh: coherent phonons with wavelength shorter than the interface defects (sw) and therefore can be scattered diffusely at the interfaces into all directions. (III) lw-

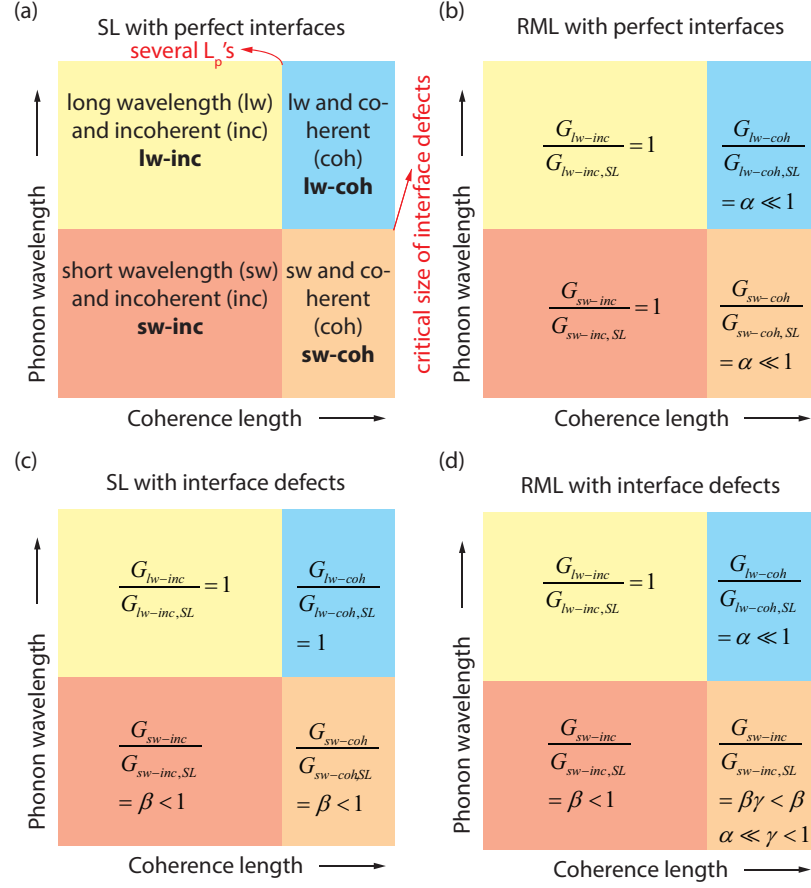


Figure 4.8. (a) Phase-diagram of the thermal conductance contributed by phonons characterized by different length scales, i.e., long-wavelength (lw), short-wavelength (sw), coherent (coh) or incoherent (inc). (b), (c) and (d) are the phase diagrams for RML with perfect interfaces, SL with interface defects and RML with interface defects, respectively.

inc: incoherent phonons (inc) of which the coherence length is shorter or comparable to  $\delta$  but the wavelength is longer than the interface defects so they are not scattered at the interfaces. (IV) sw-inc: incoherent phonons with wavelength shorter than the interface defects and hence can be scattered at interfaces.

As illustrated in Fig. 4.8b, coherent phonons (lw-coh and sw-coh) in perfect RMLs can be localized and hence their contribution to  $G$  is suppressed significantly to  $G_{coh} = \alpha G_{coh,SL}$ , where  $\alpha$  is much less than unity as localization in RMLs is effective in suppressing coherent phonon transport. Figure 4.8c demonstrates that in SLs with interface defects such as roughness or species mixing, short wavelength phonons (sw-coh and sw-inc) can be scattered diffusely by these defects and their contribution to  $G$  is thus reduced to  $G_{sw} = \beta G_{sw,SL}$ , where  $0 < \beta < 1$ . Figure 4.8d shows that in a RML with interface defects, long wavelength phonons cannot be affected by the defects; nonetheless, lw-coh can be localized to  $\alpha G_{lw-coh,SL}$  due to the RML structure. Typically, lattice defects do not break the phase of phonons, so sw-coh can still be localized in RML. However, as sw-coh phonons are scattered into all directions at the interface, it becomes more difficult to localize these 3D phonons [108]. So the localization mechanism will only suppress  $G_{sw-coh}$  to  $\gamma G_{sw-coh,SL}$  ( $\alpha < \gamma < 1$ ). The above phase-diagram analysis of scattering and localization mechanisms in SL and RML is only qualitative and certain details are also missing. For example, interface defects can also introduce disorder to the lattice, and thereby coherent phonons can be localized to some extent in SLs. Despite the rough grouping of phonons, the above phase diagrams show that coherent and incoherent phonons in IM-SL, IR-SL and IM-RML behave in much more complicated ways than those in RMLs and we shall leave detailed analysis of phonon properties in those complicated structures to our future work.

Figure 4.9a shows the  $\kappa$  of SLs and RMLs with different degrees of randomness in  $\delta$ . The meaning of  $\Delta\delta$  has been described in Section 4.2.2. As we can see,  $\kappa$  is greatly reduced by randomizing the  $\delta$  of a SL with  $\delta = 4.3$  nm (8 UC) by only 1 UC, and a 2-UC randomness in  $\delta$  can almost reduce its  $\kappa$  to the RML limit. This finding

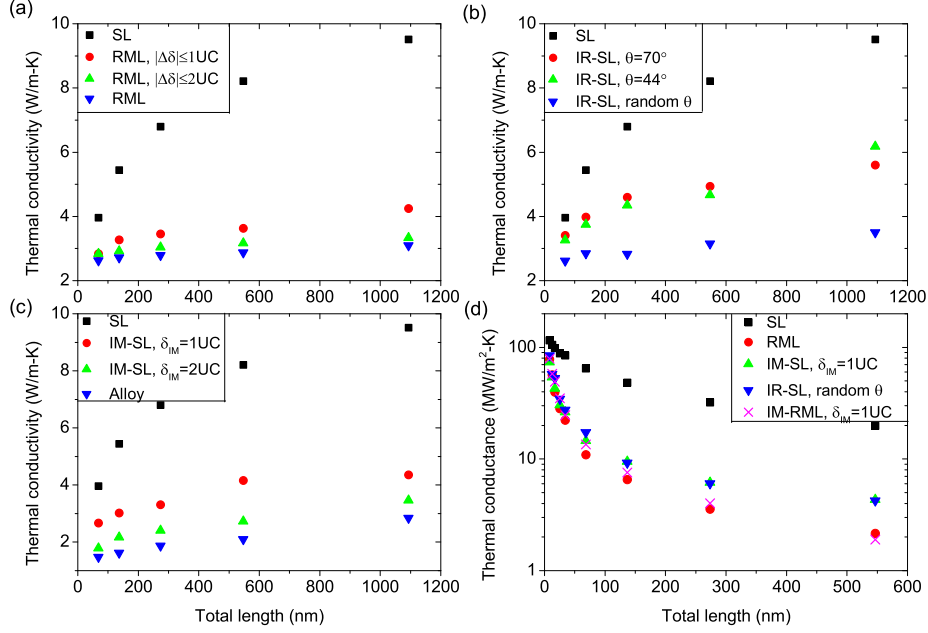


Figure 4.9. (a) Comparison of the thermal conductivity of SL and RMLs with different degree of randomness in layer thickness  $\delta$  as a function of the total length. (b) Comparison of the thermal conductivity of perfect SLs and those with different types of interface roughness. (c) Comparison of the thermal conductivity of perfect SLs and those with different degrees of interface mixing. (d) Thermal conductance of SL, RML, IM-SL, IR-SL and IM-RML as a function of the total length. All structures have  $\delta = 4.3$  nm, or 8 UC.



has important implication for experiments — if  $\delta$  cannot be controlled precisely, significant reduction in  $\kappa$  can occur for SLs with small  $\delta$  and incoherent phonon conduction will dominate.

Figure 4.2f is the schematic of a SL with IR. The periodicity of the SL is preserved if the angles and directions of the roughness at each interface are the same (periodic roughness), i.e., it is still a SL; otherwise the periodicity will be destroyed. As shown in Fig. 4.9b, the  $\kappa$ 's of SLs with periodic roughness are lower than the corresponding SLs with atomically smooth planar interfaces. If the angles are totally randomized,  $\kappa$  can be further reduced. The above observations can be explained qualitatively in this way. Coherent phonons can still transport without localization in SLs with periodic roughness, since they are still periodic and have a UC. However, the roughness can scatter incoherent phonons, thus making the  $\kappa$  lower than that of SLs with planar interfaces. In SLs with random roughness, coherent phonons can be localized by the randomness and incoherent phonons can be scattered by the interfaces, and thereby more reduction in  $\kappa$  is expected.

As shown in Fig. 4.9c, 1 UC thick of interface mixing can reduce  $\kappa$  substantially, and 2 UC can almost reduce the  $\kappa$  of SLs to the alloy limit. Besides, both the  $\kappa$  of SLs and that of alloys depend on  $L_{tot}$ , which agrees with the experiments by Luckyanova et al. [125] and Cheaito et al. [148] showing length-dependent  $\kappa$  of SLs and alloys. Therefore, the comparison between the  $\kappa$  of SLs and alloys is meaningful only when they are of the same length.

Figure 4.9d shows the thermal conductance  $G$  as a function of device length for SL, RML, IM-SL and IR-SL, and RMLs with 1UC thick of interface mixing (IM-RML).  $G$  drops quickly with  $L_{tot}$  in RML, IM-SL, IR-SL and IM-RML but much more slowly in SL. As we have seen in Fig. 4.5a, the  $G$  of SL drops at a speed of  $\sim \lambda/(\lambda + L_{tot})$  while  $G$  of RML drops almost exponentially when  $L_{tot}$  is small. The speed of reduction in  $G$  of IM-SL and IR-SL is between that of SL and RMLs, while that of IM-RML is similar to RML. Even though the interfaces in RML are atomically smooth and planar, just by randomizing the layer thickness we can reduce the  $\kappa$  of SLs to the level

of reduction that can be achieved by interface mixing or roughness. We should note that in RMLs, the reduction is only caused by localization of coherent phonons, while in IM-SL and IR-SL, the imperfect interfaces also cause diffuse scattering to phonons. However, the periodic structure of SL is mostly preserved in IM-SL and IR-SL, even though the interface mixing or roughness can scatter phonons. Thus, we believe that coherent phonons can still transport heat in IM-SLs and IR-SLs, but are suppressed by the weak localization due to disorders and scattered by the mass-difference or the roughnesses at the interfaces.

#### 4.5 Summary

To summarize, we have conducted NEMD simulations on conceptual binary Lennard-Jones systems and proposed a two-phonon model to interpret the simulation results for SLs and RMLs. Our model considers the coexistence of coherent and incoherent phonon contribution to heat conduction in SLs and RMLs, and can fit the simulation data very well.  $\kappa_{SL}$  and  $\kappa_{RML}$  were found to increase with the total length of the structure, while  $\kappa_{RML} < \kappa_{SL}$  and  $\kappa_{RML}$  saturates at a finite value much sooner than  $\kappa_{SL}$ . We attribute the increasing  $\kappa$  with total length in SLs to coherent phonon transport, and the lower  $\kappa$  of RML than SL to the localization of coherent phonons due to the random layer thickness. Using the two-phonon model, we also extracted the phonon MFP and ballistic-limit thermal conductance of coherent phonons and incoherent phonons. The  $\kappa$  of RMLs can be as low as that of SLs with interface mixing or roughness, even though RMLs have atomically smooth and planar interfaces. Nonetheless, the reduction of  $\kappa$  in these structures may result from different mechanisms, e.g. localization and scattering, and display different  $G$ - $L_{tot}$  relations. Based on our findings, we propose RMLs as low- $\kappa$  materials that may be used for thermoelectric applications.

As a final remark, we note that as the current model considers all coherent phonons and incoherent ones as two grey media, the fact that different phonon modes can

have different MFP and wavelength is significantly neglected, and the nonequilibrium between phonons [149] are not considered. A possible extension of our model would be a spectral treatment of phonon modes. Besides, when metal layers are involved, electron-phonon scattering can also considerably destroy the phase of phonons and electron-phonon nonequilibrium near the interface can also play a role in determining the thermal transport properties [24].

## 5. TWO-TEMPERATURE MOLECULAR DYNAMICS SIMULATION OF THERMAL TRANSPORT ACROSS METAL-NONMETAL INTERFACES

### 5.1 Introduction

Theoretical approaches such as acoustic mismatch model (AMM) and diffuse mismatch model (DMM) correspond to the lower and upper bounds of interfacial thermal resistance  $R_I$  between materials and can achieve reasonable agreement with experiments [150]. Atomic level methods such as non-equilibrium Green's function (NEGF) method [151, 152] and equilibrium/non-equilibrium molecular dynamics (MD) simulations [153, 154] have also been extensively used to calculate  $R_I$  for various interfaces. Both NEGF and MD simulations only need equilibrium lattice structure and interatomic potential as inputs, and phonon properties such as density of states, dispersion relations and phonon transmittance exist naturally. In modeling inelastic phonon scattering, NEGF method is usually limited to low dimensional systems due to its high computational cost. MD simulations can model such effect as well as other complicated conditions such as the atomic reconstruction at the interface straightforwardly, which is not as easily and accurately accessible by other methods. However, MD has its own drawbacks, such as finite size effect [37] and its inability to capture quantum effect [155], which can usually be circumvented or minimized with proper simulation domain design and quantum correction to the simulation results. Obviously, all the above methods only account for phononic thermal transport, while the contribution of electrons is neglected. Such simplification is restricted to be valid only for interfaces between nonmetals, where electrons contribute much less than phonons to heat transfer. When metals, semi-metals, or heavily-doped semiconductors are involved, the electronic contribution to heat conduction has to be included.

One approach to conveniently include electron-phonon coupling is the two temperature model (TTM), which designates electron and phonon as two separate subsystems and assigns a temperature for each channel [23]. It was shown using this model that electron-phonon coupling could have notable effect on thermal transport across metal-nonmetal interfaces. [23] Compared to those phononic methods mentioned above, more energy transport channels such as electronic thermal transport and electron-phonon interactions are added, leading to better approximation [23] to realistic energy transport events in materials where electrons are important. To date, TTM, combined with MD, has been used to study non-equilibrium, transient processes such as short pulse laser melting [156], cascade radiation induced defects and displacement [157], etc., which demonstrated that the incorporation of electrons could often generate significant deviations from what was predicted by MD alone. For the purpose of modeling interfacial thermal transport, TTM has so far been used qualitatively to analyze the contribution of electrons [23], while TTM alone cannot model thermal interface resistance due to phonons. An approach that can quantitatively include electron and phonon is needed for modeling interfacial thermal transport across metal-nonmetal interfaces.

In this chapter, we use a two-temperature non-equilibrium molecular dynamics method, through a combination of TTM and MD, to effectively simulate thermal transport across metal-nonmetal interfaces. We first derive an analytical solution to 1D steady-state heat conduction across metal-nonmetal system, of which the two ends are maintained at different prescribed temperatures (Dirichlet boundary condition). An exact expression of thermal resistances is obtained. Then, we describe the two-temperature molecular dynamics approach, in which phonon transport is modeled using MD and electron transport is modeled using the finite difference method. This approach achieves simultaneous modeling of phonons and electrons in a single simulation, and captures electron-phonon non-equilibrium successfully. This approach is then demonstrated via two case studies: Si-Cu and CNT-Cu interfaces. Our work demonstrate the importance of electron-phonon coupling to the accurate prediction of

thermal transport across metal-nonmetal interfaces, which leads to better agreement with experimental data than phononic MD alone.

## 5.2 Theory

### 5.2.1 Two-temperature Model

As mentioned above, TTM depicts the coupled electronic and phononic thermal transport in a quite simple picture, through separated temperature fields and a shared coupling term [158, 159]. The temporal and spatial evolution of temperature fields in this model can be generalized to two coupled heat diffusion equations as

$$\rho_e c_e \frac{\partial T_e}{\partial t} = \nabla \cdot (\kappa_e \nabla T_e) - g_{ep}(T_e - T_p) + \rho_e r_e, \quad (5.1a)$$

$$\rho_p c_p \frac{\partial T_p}{\partial t} = \nabla \cdot (\kappa_p \nabla T_p) + g_{ep}(T_e - T_p) + \rho_p r_p, \quad (5.1b)$$

where  $\rho$ ,  $c$ ,  $T$ , and  $\kappa$  denote the density, specific heat, temperature field, and thermal conductivity of electrons (subscript  $e$ ) or phonons (subscript  $p$ ).  $g_{ep}$  is the electron-phonon coupling parameter, which will be discussed in the following section.  $r$  is a mass normalized source term, including all the external sources of energy exchange/transition events such as the effects of electronic stopping, laser cooling/heating, Peltier cooling/heating and Joule heating, etc.

Equation (7.3)a and b have been used extensively to describe transient processes such as laser melting or radiation damage, or to capture the strength of electron-phonon coupling in metals [160]. A few attempts [23, 161] have been made to utilize the TTM scheme to determine the electronic contribution to the interface resistance. In order to gain a both qualitative and quantitative insight into the importance of TTM to this topic, we will also start with an analytical derivation of a 1D interfacial thermal transport problem with Dirichlet boundary condition (prescribed boundary temperatures).

The representative temperature profiles for thermal transport across a metal-nonmetal interface are shown in Fig. 5.1.  $l$  denotes the length of the left side (sub-

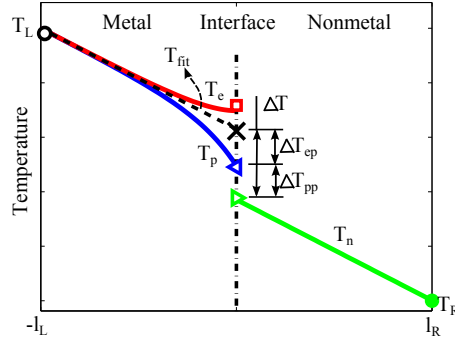


Figure 5.1. Representative temperature profiles in TTM for a metal-nonmetal interface.  $T_n$ ,  $T_p$  and  $T_e$  are temperature profiles for phonons in the nonmetal side, phonons in the metal side and electrons in the metal side.  $T_{fit}$  is a linear fit of the temperature profile of the electron-phonon equilibrium region. In the metal side near the interface, electrons and phonons have different temperature, which indicates electron-phonon non-equilibrium.  $\Delta T_{ep}$  and  $\Delta T_{pp}$  denote the temperature continuity related to the electron-phonon coupling in the metal side and the phonon-phonon coupling across the interface, respectively.  $\Delta T = \Delta T_{ep} + \Delta T_{pp}$  is the total temperature jump at the interface. Figure reproduced from Ref. [24].

script  $L$ ) or right side (subscript  $R$ ), which are metal and nonmetal, respectively.  $T_L$  and  $T_R$  are prescribed temperatures at the left and right end, which form the Dirichlet boundary conditions for this heat transfer problem.  $T$  with subscripts  $n$  (phonons in the nonmetal side),  $p$  (phonons in the metal side),  $e$  (electrons in the metal side) and  $fit$  (the linear fit of the temperature profile of the electron-phonon equilibrium region) denote corresponding temperature field as a function of position,  $x$ . Herein we assume that electrons in the nonmetal side does not contribute to heat conduction, so that electronic heat transfer is confined in the metal side only. This assumption is reasonable considering that electrons only account for  $\sim 0.02\%$  of the overall thermal transport in Si, and less than  $\sim 10\%$  even in metallic single-walled CNTs at room temperature. We are not addressing the term,  $r$ , in Eq. (7.3), which accounts for electronic stopping effects, laser heating/cooling, etc., since they are not in the scope of this work but can be easily implemented in this TTM-MD method if accurate models for these processes are available. Consequently, for 1D steady state heat transport with constant values of  $\kappa_e$ ,  $\kappa_p$ , we obtain the electron/phonon energy diffusion equations coupled via the electron-phonon coupling term,  $g_{ep}$ .

$$\frac{d^2 T_e}{dx^2} - \frac{g_{ep}(T_e - T_p)}{\kappa_e} = 0 \quad (5.2a)$$

$$\frac{d^2 T_p}{dx^2} + \frac{g_{ep}(T_e - T_p)}{\kappa_p} = 0 \quad (5.2b)$$

Equations 5.2a and 5.2b are essentially the same as the starting equations in Ref. [23]. Subtracting Eq. (5.2a) from Eq. (5.2b),

$$\frac{d^2 \theta}{dx^2} - \gamma^2 \theta = 0 \quad (5.3)$$

where  $\theta = T_p - T_e$  and

$$\gamma = \sqrt{g_{ep} \left( \frac{1}{\kappa_e} + \frac{1}{\kappa_p} \right)} \quad (5.4)$$

Note that the boundary condition at the far end of the metal is  $\theta|_{x \rightarrow -\infty} = 0$ . The solution to Eq. (5.3) is thus  $\theta = c \cdot \exp(\gamma x)$ , where  $c$  is a constant of integration to be determined. Accordingly,  $\nabla \theta|_{x=0} = \gamma \cdot c$ .



Let us denote the steady-state heat current resulting from the temperature bias,  $T_L - T_R$ , as  $J$ , which is positive for left-to-right direction and vice versa. Recall that  $J$  is assumed to be carried by both electrons and phonons in the metal side and only by phonons in the nonmetal side, thereby we have another set of boundary conditions at the interface, which are  $-J = \kappa_n \nabla T_n|_{x=0} = \kappa_p \nabla T_p|_{x=0}$  and  $\nabla T_e|_{x=0} = 0$ , and hence

$$\nabla \theta|_{x=0} = \nabla T_p|_{x=0} - \nabla T_e|_{x=0} = \nabla T_p|_{x=0} = -\frac{J}{\kappa_p} \quad (5.5)$$

We combine  $\nabla \theta|_{x=0} = \gamma \cdot c$  with Eq. (5.5) and get  $c = -\frac{J}{\gamma \kappa_p}$ , so

$$\theta = -\frac{J}{\gamma \kappa_p} \exp(-\gamma|x|) \quad (5.6)$$

Equation (5.6) enables us to define a non-equilibrium length, or cooling length [161], which quantifies the electron-phonon non-equilibrium distance. Specifically, if we define such a characteristic length as the distance between the position of  $\theta_{max}$  and  $5\% \theta_{max}$ , then

$$l_{NE} \approx \frac{3}{\gamma} = \frac{3}{\sqrt{g_{ep}(\frac{1}{\kappa_e} + \frac{1}{\kappa_p})}} \quad (5.7)$$

In metal, the overall Fourier's law considering both electrons and phonons is

$$-J = \kappa_p \nabla T_p + \kappa_e \nabla T_e \quad (5.8)$$

and from Eq. (5.6), we know

$$\nabla \theta = \nabla T_p - \nabla T_e = -\frac{J}{\kappa_p} \exp(\gamma x) \quad (5.9)$$

Combining Eq. (5.8) and Eq. (5.9), it is easy to solve for  $\nabla T_p$  and  $\nabla T_e$ . Integrating the results with the Dirichlet boundary conditions, we obtain the exact temperature field in the metal side,

$$T_e = \frac{J}{\kappa_e + \kappa_p} \left[ \frac{1}{\gamma} \exp(\gamma x) - \frac{1}{\gamma} \exp(-\gamma l_L) - x - l_L \right] + T_L \quad (5.10a)$$

$$T_p = \frac{J}{\kappa_e + \kappa_p} \left[ \frac{1}{\gamma} \exp(\gamma x) - \frac{1}{\gamma} \exp(-\gamma l_L) - x - l_L \right] + T_L - \frac{J}{\gamma \kappa_p} \exp(\gamma x) \quad (5.10b)$$

As a first approximation, we assume that thermal transport across metal-nonmetal interface is only contributed by phonon-phonon coupling, i.e., phonon-mediated. Such

assumption is commonly adopted in theoretical methods such as DMM and AMM. However, a refined model would consider the penetration of electrons into the non-metal side, which will be considered in our future work. We define the interfacial thermal conductance caused by such phonon-phonon coupling as  $h_{pp}$ , and correspondingly,

$$\frac{J}{(T_p - T_n)|_{x=0}} = h_{pp} \quad (5.11)$$

On the nonmetal side, the Fourier's law is

$$\kappa_n \nabla T_n = -J \quad (5.12)$$

With one boundary condition as  $T_n|_{x=l_R} = T_R$ , Eq. (5.12) leads to

$$T_n|_{x=0} = T_R + \frac{J \cdot l_R}{\kappa_n} \quad (5.13)$$

Combining Eqs.5.10, 5.11 and 5.13, we finally get

$$R_{tot} = \frac{T_L - T_R}{J} = \frac{l_L}{\kappa_e + \kappa_p} + \frac{1}{h_{pp}} + \left(\frac{\kappa_e}{\kappa_e + \kappa_p}\right)^{\frac{3}{2}} \left(\frac{1}{g_{ep}\kappa_p}\right)^{\frac{1}{2}} + \frac{l_R}{\kappa_n} \quad (5.14)$$

Evidently, Eq. (5.14) indicates that the metal-nonmetal system can be described as a series thermal circuit. More specifically, the first and the last term on the right hand side of Eq. (5.14) are the formal Fourier thermal resistance of the metal and nonmetal segments, respectively. The second and third terms are the interfacial thermal resistances associated with phonon-phonon coupling ( $R_{pp}$ ) and electron-phonon coupling ( $R_{ep}$ ), respectively. Our result is essentially the same as [23]'s work [23] though for different boundary conditions. Subtracting the two bulk thermal resistances, it is evident that the interfacial thermal resistance can be written as

$$R_I = \frac{\Delta T}{J} = R_{pp} + R_{ep} = \frac{1}{h_{pp}} + \left(\frac{\kappa_e}{\kappa_e + \kappa_p}\right)^{\frac{3}{2}} \left(\frac{1}{g_{ep}\kappa_p}\right)^{\frac{1}{2}}. \quad (5.15)$$

where  $\Delta T = (T_n - T_{fit})|_{x=0}$ , and is indicated in Fig. 5.1 as the summation of  $\Delta T_{ep}$  and  $\Delta T_{pp}$ , corresponding to the interfacial temperature noncontinuity related to electron-phonon coupling in the metal side and phonon-phonon coupling across the interface, respectively.

Table 5.1.  $g_{ep}$  for Cu obtained via various methods.

Reference	Method	$g_{ep}$ ( $10^{16}$ W/m <sup>3</sup> -K)
[162]	<i>ab initio</i>	$\sim 5.5$ <sup>1</sup> .
[163]	pump-probe experiment through time-resolved transmissivity	$\sim 10$
[164]	<i>ab initio</i>	8.43
[160]	pump-probe experiment through transient thermorefectance spec- troscopy	$26$ <sup>2</sup>

### 5.2.2 Input Parameters

In practice, the utilization of TTM is usually quite cumbersome due to its input parameters, i.e.,  $c_e$ ,  $\kappa_e$  and  $g_{ep}$ . Lin et al. conducted comprehensive studies on the temperature dependence of  $c_e$  for eight representative metals from first principle [162], and a linear relation between  $c_e$  and  $T_e$  is usually valid for a temperature below 1,000 K, a regime for most thermal interface applications.  $\kappa_e$  can be approximated via the Wiedemann-Franz law based on a knowledge of the Lorenz number and electrical conductivity, given that most electron-electron collisions are elastic, which has been adopted in previous TTM works [157]. Another way to calculate  $\kappa_e$ , as stated in Ref. [162], is through the Drude model, which does not guarantee better approximations due to the complicated temperature dependence of  $c_e$  and electron-phonon and electron-electron scattering rates [162]. Tremendous efforts have been made in search of an accurate model of electron-phonon interactions in various materials [160, 162, 163, 165, 166]. [165] divide electron-phonon interactions, through a cutoff ion velocity [165, 166], into two distinct regimes, i.e., electronic stopping and electron-phonon coupling. The former regime is characterized by ballistic movement of ions with extremely high energy, e.g., 8.6 eV for Fe [165], which is not present in most interfacial thermal transport problems. On the other hand, electron-phonon cou-

pling dominates the overall electron-phonon interactions in a solid-state crystal, where atoms vibrate around their equilibrium positions. Various methods [160, 162–164] have been applied to calculate the electron-phonon coupling coefficient,  $g_{ep}$ , as a linear approximation of electron-phonon energy exchange through the  $g_{ep}(T_e - T_p)$  term in TTM. However, the obtained  $g_{ep}$ 's can vary by an order of magnitude for the same material (see Table. 5.1 for a list of measured  $g_{ep}$  for Cu), which suggests the inaccuracy, to a certain extent, of the linear approximation.

For the purpose of thermal transport modeling, MD simulation is advantageous with respect to other theoretical approaches, e.g., AMM and DMM, in modeling thermal transport processes in that it naturally includes the effects of interface bonding and topography, without sophisticated assumptions on those properties. The only inputs needed by MD simulation are the atomic structure and empirical inter-atomic potentials. MD simulations have been used extensively to compute thermal boundary conductance (resistance) across solid-solid interfaces [110], however, mainly limited to nonmetals. To incorporate electronic effects into the modeling of radiation damage simulations, [165] introduced a TTM-MD simulation scheme capable of accounting for electron-phonon coupling, electronic stopping and both the temporal and spatial evolution of the phononic and electronic subsystems [165, 166]. Subsequently, [159] modified [165]'s design to an energy-conserving version by adding a communication process between the electronic and atomic subsystems [159]. Herein we adopt [159]'s version, using the LAMMPS package [76] (we have modified its *ttm* module to support non-periodic boundary conditions), to perform non-equilibrium MD simulation for phonon degree of freedom, which is coupled with finite difference (FD) calculation for the electron degree of freedom.

In parallel with Eqs. 7.3a and 7.3b, the TTM-MD simulation models coupled electronic subsystem and phononic subsystem simultaneously, as illustrated in Fig. 5.2. Phononic heat diffusion (Eq. (7.3b) except the last term) is still modeled by the usual MD technique.  $\kappa_p$  is thus calculated implicitly by MD, where its dependence on temperature, interface atomic reconstruction [167] and mixing [168] are included.

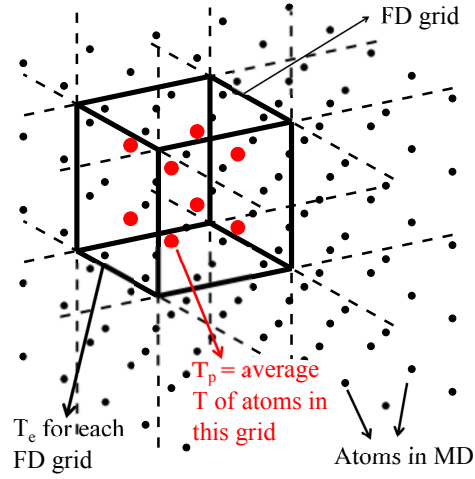


Figure 5.2. Illustration of the coupled electronic and phononic subsystems using FD and MD in TTM-MD simulations. Lines represent FD grids, with solid ones denoting the grid of interest. Dots are atoms in MD simulations, with enlarged ones denoting the atoms inside the FD grid of interest. Thermal transport in the electronic subsystem is modeled by solving Eq. (7.3a) using FD method, where each grid has its own  $T_e$ , and  $T_p$  is the average temperature of the MD atoms inside this grid. Phononic subsystem is modeled by the MD simulation, with each atom subject to a Langevin force, which equilibrates their temperatures to the  $T_e$  of the overlapping FD grid. Figure reproduced from Ref. [24].

In addition, in the TTM-MD approach, electron-phonon non-equilibrium near the interface leads to phonon generation, which can disturb the original phonon scattering, and hence affects phonon transport. This feature is neglected in [23]’s analytical treatment [23], where  $\kappa_p$  was calculated elsewhere. The electronic subsystem is modeled by solving Eq. (7.3a) iteratively with the FD method. Phonons and electrons are coupled via the  $g_{ep}(T_e - T_p)$  term in Eq. (7.3), where  $T_e$  is the electron temperature of each FD grid, and  $T_p$  is the average temperature of the MD atoms inside that grid.

In practice, the equation of motion for an atom  $i$  in the MD part is in the form of a Langevin thermostat [157, 165, 166]:

$$m_i \frac{\partial \mathbf{v}_i}{\partial t} = \mathbf{F}_i(t) - \gamma_i \mathbf{v}_i + \tilde{\mathbf{F}}_i(t) \quad (5.16)$$

where  $m$  and  $\mathbf{v}$  are merely the atomic mass and velocity.  $\mathbf{F}_i$  is the total force exerted on atom  $i$ , evaluated via empirical inter-atomic potentials.  $\gamma_i$  is a friction term representing the energy loss by electron-ion interactions, and is directly related to  $g_{ep}$  as [165]

$$\gamma_i = \frac{m_i g_{ep}}{3n_i k_B} \quad (5.17)$$

with  $n$  denoting the atom number density and  $k_B$  the Boltzmann constant.  $\tilde{\mathbf{F}}_i(t)$  is a random force term commonly seen in Langevin dynamics, and for this specific case,

$$\tilde{\mathbf{F}}_i(t) = \sqrt{\frac{24k_B T_e \gamma_i}{\Delta t}} \tilde{\mathbf{R}}_i \quad (5.18)$$

where  $\Delta t$  is the temporal interval of the simulation and  $\tilde{\mathbf{R}}$  is a random vector  $[R_1, R_2, R_3]$  with  $R_j \in [-0.5, 0.5]$ . The summation of the last two terms of Eq. (5.16), i.e.,  $-\gamma_i \mathbf{v}_i + \tilde{\mathbf{F}}_i(t)$ , equilibrates the electronic and phononic subsystems to a shared temperature [159, 165].

So far, we have gone through a complete process of the evolution of the phononic subsystem in the MD part. The total energy transferred from the electronic subsystem to the phononic one through the Langevin force,  $-\gamma_i \mathbf{v}_i + \tilde{\mathbf{F}}_i(t)$  in Eq. (5.16), is thus [157, 159]

$$\tilde{E}_{ep} = \left[ -\gamma_i \mathbf{v}_i + \tilde{\mathbf{F}}_i(t) \right] \mathbf{v}_i \Delta t \quad (5.19)$$

Finally, we replace  $g_{ep}(T_e - T_p)$  with  $\tilde{E}_{ep}$  in Eq. (7.3a), establishing a complete electronic thermal diffusion process, and the total energy of the whole system is also conserved. It should be noted that the validity of both the MD simulation and the FD calculation of electronic heat diffusion is based on the assumption of local equilibrium. To satisfy this criteria, the number of atoms accounted for by each grid should be larger than a critical value to make sure the fluctuation of temperature is small enough, which is in contrast to the discrete nature of FD which prefers finer grids. We have checked our simulations on Si-Cu and CNT-Cu systems, and the temporal local temperature fluctuation is usually below 15% when each grid contains more than 1,000 atoms. To successfully model interfacial thermal transport processes, where electron-phonon non-equilibrium adjacent to the interface is crucial, we should also make sure that the FD grids should be sufficiently shorter than  $l_{NE}$  in the heat flow direction, as defined by Eq. (5.7).

### 5.3 Case Studies

#### 5.3.1 Pure Copper

To verify that this TTM-MD method is capable of modeling coupled electronic and phononic thermal transport in metals, we first calculate the thermal conductivity of a homogeneous Cu ( $m_{Cu} = 63.55$  g/mol, and  $\sim 72$  nm  $\times$  4 nm  $\times$  4 nm) in the [100] direction, as shown in Fig. 5.3a. We do not consider its natural abundance (69.15%  $^{63}\text{Cu}$  and 30.85%  $^{65}\text{Cu}$ ) here since the corresponding mass-disorder is negligible in terms of thermal transport. In the MD domain, the outermost layer of atoms on both ends of the Cu are fixed, while the periodic boundary condition is applied to the lateral directions. The FD calculation contains  $100 \times 1 \times 1$  grids, which corresponds to 600 atoms/grid. This ensures a temperature fluctuation in each FD grid less than 10%, which is well compatible with the local equilibrium requirement. Adiabatic thermal boundary condition is used at the two ends of the FD domain, which allows for the establishment of a steady temperature gradient. The embedded-atom method

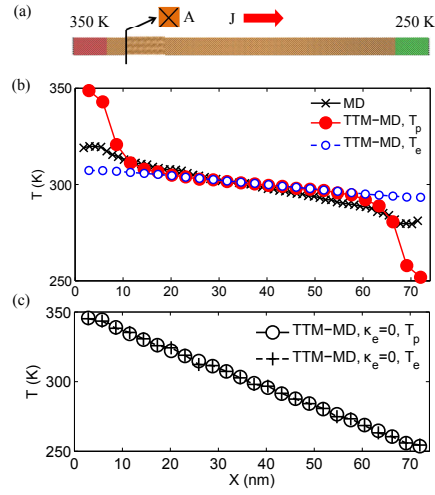


Figure 5.3. (a): the simulation setup. (b) and (c): the steady-state temperature profiles obtained in conventional MD and TTM-MD simulations on pure Cu. Electron-phonon non-equilibrium can be seen at and near the thermostat region in (b). Electron and phonon are always in equilibrium in (c) since we use  $\kappa_e = 0$ . Figure reproduced from Ref. [24].



(EAM) [169] is adopted for Cu-Cu interactions. The system is first relaxed in the NVT ensemble (300 K) via the Nosé-Hoover thermostat for 0.5 ns with a time step of 0.5 fs. After that, the system is switched to non-equilibrium MD, where atomic temperatures at the two ends are maintained at 350 K and 250 K, respectively, through a direct velocity scaling algorithm implemented in LAMMPS. The resulting heat current  $J$  is calculated by  $J = (J_L - J_R)/2$ , where  $J_L$  and  $J_R$  are the amount of kinetic energy injected into the left and right thermostat per unit time. Such non-equilibrium MD simulation is continued for  $9 \times 10^6$  steps, of which the last  $4.5 \times 10^6$  steps are used for data production and post-processing.

We conduct both conventional MD and TTM-MD, and in the latter case we use  $\kappa_e = 401$  W/m-K, which is actually the total  $\kappa$  of Cu at room temperature. Since the lattice contribution to thermal transport in Cu is rather small compared with the electronic part, previous studies [160] usually used the total  $\kappa$  as a first approximation for  $\kappa_e$ . Besides, we use the value of  $2.6 \times 10^{17}$  W/m<sup>3</sup>-K, as obtained from [160]'s experiment, for  $g_{ep}$ . The corresponding steady-state temperature profiles are plotted in Fig. 5.3b. The temperature gradient  $\partial T/\partial x$  can be extracted from the central part of the temperature profiles, where they are linear for both methods and  $T_e = T_p$  for TTM-MD. The two electron-phonon non-equilibrium regions near the thermostats are due to the fact that we only apply thermostats to phonons in the TTM-MD simulation, which does not violate the validity of this method as long as we calculate  $\kappa$  with the linear temperature profile in electron-phonon equilibrium region (central part of the structure). As a verification for this method, we also perform TTM-MD with  $\kappa_e = 0$ , corresponding to  $l_{NE} = 0$  from Eq. (5.7). In the resulting temperature profile, Fig. 5.3c, electrons and phonons have the same temperature all the way from the hot thermostat to the cold one, indicating excellent agreement between our TTM-MD simulation and the analytical solution. Thermal conductivity,  $\kappa$ , is obtained according to the Fourier's law of heat conduction:

$$\kappa = -\frac{J/A}{\partial T/\partial x} \quad (5.20)$$

where  $A$  is the cross-sectional area of the Cu.

Table 5.2.  $\kappa$  of Cu obtained via different methods. Table reproduced from Ref. [24].

Source	Method	$\kappa$ (W/m-K)
Ref. [170]	Experiment	$\sim 401$
Ref. [171]	Equilibrium MD	$\sim 15$
Ref. [172]	Non-equilibrium MD	$\sim 10.4$
This work	Non-equilibrium MD	$13.6 \pm 1.4$
This work	TTM-MD	$415 \pm 11$

Table. 5.2 lists the experimental value [170] of  $\kappa$ , and those calculated in previous theoretical studies [171,172] and in this work, using conventional MD and TTM-MD. As can be seen,  $\kappa$ 's from conventional MD are below 15 W/m-K, which only accounts for the phononic thermal transport. TTM-MD predicts  $\kappa = 415 \pm 11$  W/m-K, where the electronic contribution is set to be 401 W/m-K, and the phonon contribution accounts for the rest, suggesting the capability of this TTM-MD method in accounting for the electronic contribution to  $\kappa$ .

### 5.3.2 Si-Cu Interface

Modern integrated circuit (IC) industry relies significantly on Si and Cu as wafers (substrates) or interconnects. The presence of Si-Cu interface is inevitable and plays an increasingly important role in determining the thermal and electrical performance as the dimension of the devices drops to micro- and nano-scale. Herein we perform MD as well as TTM-MD simulations on thermal transport across a system composed of Si ( $\sim 35 \text{ nm} \times 5.4 \text{ nm} \times 5.4 \text{ nm}$ ) and Cu ( $\sim 100 \text{ nm} \times 5.4 \text{ nm} \times 5.4 \text{ nm}$ ) in contact via their (100) faces, which are initially separated by 3.15 Å. In the MD part for both methods, we apply the periodic boundary condition to all directions, i.e., x, y and z. The many-body Tersoff potential [78] and EAM [169] are used for Si-Si and Cu-Cu interactions, respectively. Interfacial interactions between Si and Cu atoms are modeled via a Morse-type potential function [173],

$$U = D_e [e^{-2\alpha(r-r_0)} - 2e^{-\alpha(r-r_0)}] \quad (5.21)$$

where  $D_e = 0.9 \text{ eV}$ ,  $\alpha = 1.11 \text{ Å}^{-1}$  and  $r_0 = 3.15 \text{ Å}$ , with a cutoff radius of 3.5 Å. Such pair potential function has been adopted previously to study Cu nanocluster diffusion [174] and deposition [173] associated with CNT or Si. The accuracy of this potential in thermal transport prediction has not been validated yet, and here we use it in the purpose of demonstrating the TTM-MD approach. Potential refinement may be needed in the future for accurate prediction for the Si-Cu interface. The system is first relaxed at zero pressure and constant temperature via the Nosé-Hoover

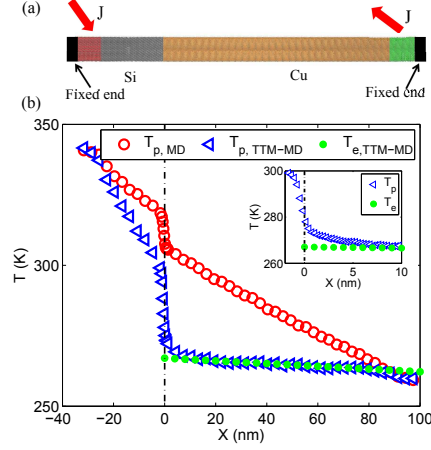


Figure 5.4. (a) illustrates the simulation domain setup, where the segments denoted by different colors are fixed end, hot thermostat, Si system, Cu system, cold thermostat and fixed end from left to right. (b) shows the steady-state temperature profiles obtained in conventional MD and TTM-MD simulations on a Si-Cu system. The inset is a zoom-in of  $T_e$  and  $T_p$  adjacent to the interface. Figure reproduced from Ref. [24].

thermostat for 0.5 ns. Then the outermost 20 Å of atoms on both ends are fixed, as shown in Fig. 5.4a, so that phonons cannot transport from one end to the other end of the simulation cell directly across the periodic boundary. In other words, the periodic boundary condition is replaced with the fixed one for the x direction. After that, we designate the regions ( $\sim 10$  nm long) adjacent to the inner boundary of the fixed ends as thermostats, and keep injecting a constant heat flux,  $J = 3.2 \times 10^{-7}$  W, into one thermostat, while subtracting the same amount from the other simultaneously. We only use FD calculation for the Cu part, instead of the whole structure. The FD domain is divided into  $128 \times 1 \times 1$  grids, corresponding to more than 1,800 Cu atoms/grid, thus limiting the local temperature fluctuation within 15%.

The steady-state temperature profiles obtained from both conventional MD and TTM-MD simulations are plotted in Fig. 5.4b. It should be noted that, to clearly compare these two methods, we apply the Dirichlet boundary condition using the direct velocity rescaling method [76] for this case, with a fixed temperature bias of 80

K, instead of the constant heat flux method we use for all the other simulations in this and following sections. On the Si side,  $T_{p,TTM-MD}$  has much larger slope than  $T_{p,MD}$  since the total heat current is much higher in the former case, due to the addition of electronic thermal transport channel that greatly reduces the thermal resistivity of Cu. On the Cu side, the reduced thermal resistivity of Cu leads to much lower slope of  $T_{p,TTM-MD}$  than  $T_{p,MD}$ . The electron-phonon non-equilibrium, of which the analytical form has been shown in Fig. 5.1, can be clearly seen in the inset of Fig. 5.4, where  $T_e$  is almost flat near the interface, consistent with its adiabatic nature. From the temperature profiles, we can obtain the temperature jump at the interface,  $\Delta T$ , in the same way as shown in Fig. 5.1. The interfacial thermal resistance is thus

$$R_I = \frac{A\Delta T}{J} \quad (5.22)$$

As discussed in Section 7.3, great caution should be exercised in choosing appropriate input parameters, i.e.,  $\kappa_e$ ,  $c_e$  and  $g_{ep}$ , from many candidates in TTM-MD. However, many metals such as Cu, Au, Pt and W have fairly constant values of  $\kappa$  in the range of 200 K to 1,000 K [170]. Specifically,  $\kappa$  of Cu decreases gradually from 410 W/m-K at 200 K to 360 W/m-K at 1,000 K, where  $\kappa_p$  is only around 10 W/m-K [171]. Equation (5.14) suggests that when  $\kappa_e \gg \kappa_p$ ,  $R_{ep}$  is independent of  $\kappa_e$  since  $R_{ep} \approx (g_{ep}\kappa_p)^{-0.5}$ . As a test, we calculate  $R_I$  using  $\kappa_e$  ranging from 10 W/m-K to 450 W/m-K, with constant values of  $g_{ep}$  and  $c_e$ . As shown in Fig. 5.5,  $R_I$  increases with  $\kappa_e$  at first, but saturates when  $\kappa_e > 100$  W/m-K. Therefore, in the range of temperature at which we perform TTM-MD simulations on Cu,  $\kappa_e$  has negligible effect on  $R_I$ , and we can safely use  $\kappa_e = 401$  W/m-K for all calculations. Similarly, Eq. (5.14) reveals that  $c_e$  should also be insignificant in steady-state interfacial thermal transport problems. We compare the results using a constant  $c_e$  and a temperature dependent  $c_e$  (its volumetric form is  $C_e = 96.8 \text{ J/m}^3\text{-K}^2 \times T_e$ ) in Fig. 5.6, and evidently, the effect on  $R_I$  is minor, as expected.

[162] has calculated  $g_{ep}$  for various metals including Cu for  $T_e$  ranging from room temperature to  $2 \times 10^4$  K, where  $g_{ep}$  is almost constant below 2,000 K [162]. Subsequently, [175] found better agreement with experimental observation of the temporal

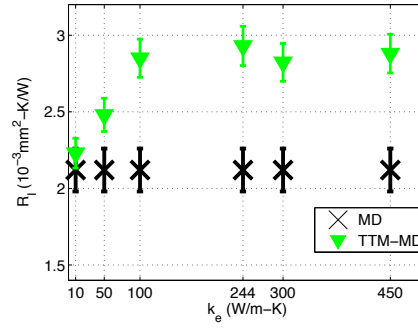


Figure 5.5.  $\kappa_e$  dependence of  $R_I$  predicted by TTM-MD simulations.  $R_I$  saturates when  $\kappa_e > 100$  W/m-K. The data for MD (crosses) are duplicates of the single data obtained from repeated MD simulations at 300 K. Figure reproduced from Ref. [24].

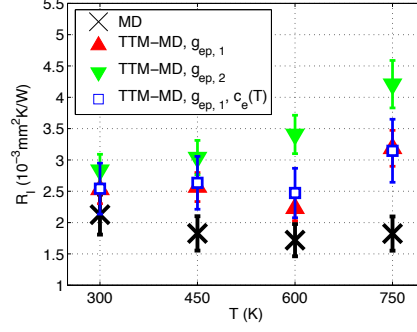


Figure 5.6.  $R_I$  calculated from MD and TTM-MD simulations for Si-Cu interface.  $g_{ep,1} = 2.6 \times 10^{17}$  W/m<sup>3</sup>-K, and  $g_{ep,2} = 5.5 \times 10^{16}$  W/m<sup>3</sup>-K.  $c_e(T)$  means the use of temperature dependent volumetric heat capacity  $C_e$  ( $= 96.8$  J/m<sup>3</sup>-K<sup>2</sup>  $\times T_e$ ) in TTM-MD simulation. Figure reproduced from Ref. [24].

evolution of  $T_e$  using [162]’s data than [163]’s. Herein, for the sake of accurate calculation as well as evaluating the importance of  $g_{ep}$ , we compute  $R_I$  using  $g_{ep,1}$  [160]  $= 2.6 \times 10^{17}$  W/m<sup>3</sup>-K, and  $g_{ep,2}$  [162]  $= 5.5 \times 10^{16}$  W/m<sup>3</sup>-K, respectively. As shown in Fig. 5.6,  $g_{ep,1}$  results in significantly higher (by  $> 25\%$ )  $R_I$  than conventional MD, and  $g_{ep,2}$  predicts even higher  $R_I$ , which agrees with the trend predicted by Eq. (5.14). Using Eq. (5.14) with  $\kappa_e = 401$  W/m-K and  $\kappa_p = 13.6$  W/m-K (Table 5.2), we can calculate  $R_{ep}$  to be  $\sim 0.5 \times 10^{-3}$  mm<sup>2</sup>-K/W and  $\sim 1.1 \times 10^{-3}$  mm<sup>2</sup>-K/W for  $g_{ep,1}$  and  $g_{ep,2}$ , respectively. If we simply add  $R_{ep}$  to  $R_{pp}$  (dark crosses in Fig. 5.6), which is the method used in Ref. [23], the values are  $2.6 \times 10^{-3}$  mm<sup>2</sup>-K/W and  $3.2 \times 10^{-3}$  mm<sup>2</sup>-K/W at 300 K, which overpredicts the TTM-MD results by 6% and 15%, respectively. The neglect of electronic effect on phononic thermal transport, by simple summation of  $R_{pp}$  and  $R_{ep}$  obtained from separate calculations, leads to inherent inaccuracy of previous analytical approaches [23, 161], and hence TTM-MD is preferred in that sense.

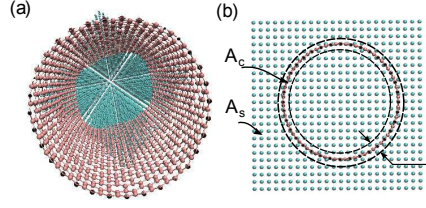


Figure 5.7. (a): perspective view (front) of the CNT-Cu interface; (b): schematic of the definition of the cross-sectional area of the Cu substrate ( $A_s$ ) and the contact ( $A_c$ ) in Eq. (5.23). Figure reproduced from Ref. [24].

### 5.3.3 CNT-Cu Interface

CNT and graphene, of which both intrinsically possess very high  $\kappa$  and elastic modulus, have been proposed as excellent thermal interface materials [176,177] to fill gaps between solid-solid surfaces, e.g., silicon dies, heat sinks, etc. In this section, we conduct TTM-MD simulations on thermal transport across CNT-Cu interface. Similar to Si-Cu, we use the same Morse-type potential function ( $D_e = 2.277$  eV,  $\alpha = 1.7 \text{ \AA}^{-1}$  and  $r_0 = 2.2 \text{ \AA}$ ) [174] for C-Cu interactions, with a cutoff radius of  $2.5 \text{ \AA}$ . The equilibrium structure is shown in Fig. 5.7a, where strong atomic reconstruction of CNT near the interface [167] can be seen due to the rather strong interaction between C and Cu. The zigzag CNT (100.0 nm long and 3.6 nm in diameter) is in end-contact with the (100) face of Cu ( $100 \text{ nm} \times 5.4 \text{ nm} \times 5.4 \text{ nm}$ ), with an initial separation of  $2.2 \text{ \AA}$ . All the other simulation setup details are the same as our Si-Cu simulations in Section 5.3.2.

Special caution should be made to the definition of  $R_I$  for CNT-Cu interfaces due to the hollow geometry of CNTs. Herein we calculate  $R_I$  of CNT-Cu as the thermal resistance per unit cross-sectional area of the substrate ( $A_s$ , see Fig. 5.7b), i.e., Cu in this work, which is

$$R_I = \frac{A_s \Delta T}{J} = \frac{A_c \Delta T}{J} \left( \frac{A_s}{A_c} \right) \quad (5.23)$$



Table 5.3. Comparison of  $R_I$  of CNT-Cu interface from MD, TTM-MD and experiment. Table reproduced from Ref. [24].

Source	Method	$R_I$ (mm <sup>2</sup> -K/W)
Ref. [176]	Experiment <sup>3</sup>	$1 \pm 0.5$
Ref. [176]	Experiment <sup>4</sup>	$0.9 \sim 0.5$
This work	Non-equilibrium MD	$0.18 \pm 0.02$
This work	TTM-MD	$0.23 \pm 0.03$

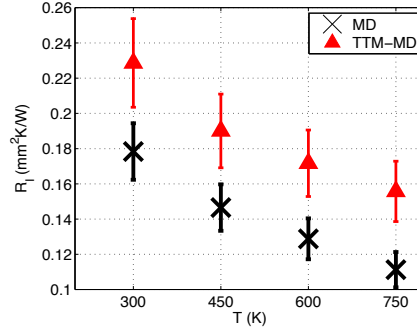


Figure 5.8.  $R_I$  calculated from MD and TTM-MD simulations for the CNT-Cu interface, where  $A_c/A_s = 1.0\%$  is used. Figure reproduced from Ref. [24].

where  $A_c$  is the real contact area between CNT and Cu, i.e., the annular area of CNT for complete contact conditions.  $A_c$  is calculated by  $A_c = \pi D t$ , where  $D$  and  $t$  (0.335 nm) are the diameter and wall thickness of the CNT, respectively.  $A_c/A_s$  is usually referred to as the CNT engagement factor [16]. As pointed out in Ref. [16],  $A_c/A_s$  is usually between 0.5%–0.9%, which leads to a large  $R_I$  of CNT-metal interfaces. In Ref. [176], the scanning electron microscope image implies that  $A_c/A_s \approx 1.89\%$ , if we assume that CNTs and the Cu sheet are in complete contact. We will calculate  $R_I$  for CNT-Cu using a medium value of  $A_c/A_s$ , i.e., 1.0%.

The temperature dependence of  $R_I$  is calculated using both MD and TTM-MD, where  $g_{ep} = 5.5 \times 10^{16}$  W/m<sup>3</sup>-K and  $C_e = 96.8$  J/m<sup>3</sup>-K<sup>2</sup>  $\times T_e$  are used. As shown in Fig. 5.8, the TTM-MD predicts higher  $R_I$  than MD alone by a factor of  $\sim 30\%$

on average. We compare  $R_I$  at 300 K calculated by MD and TTM-MD simulations with experimental data in Table. 5.3. We should note that if we use  $g_{ep} = 2.6 \times 10^{17}$  W/m<sup>3</sup>-K,  $R_I$  will be  $\sim 0.21$  mm<sup>2</sup>-K/W, which indicates that an accurate value of  $g_{ep}$  is crucial to the prediction of  $R_I$ .

## 5.4 Summary

We have used TTM-MD simulation to achieve simultaneous modeling of coupled phononic and electronic thermal transport in metal-nonmetal systems in a single simulation. By incorporating the electron degree of freedom to the phononic MD simulation, we are able to capture the non-equilibrium between electron and phonon in a steady-state heat conduction condition, which plays an important role in thermal transport across metal-nonmetal interfaces. The simulation results obtained using this TTM-MD method are physically more sound and are in better agreement with experimental data compared to those obtained using conventional MD simulations.

## 6. FIRST-PRINCIPLES CALCULATION OF PHONON-ELECTRON AND PHONON-PHONON SCATTERING RATES IN SOLIDS

### 6.1 Introduction

An important implication of the two-temperature model (TTM) is that the thermal conductivity  $\kappa$  of metals affects not only thermal transport inside metallic components, but also heat transfer across metal-dielectric interfaces. [23] Despite that a knowledge of the lattice thermal conductivity  $\kappa_L$  is required to model thermal transport in systems including metallic components, the lattice  $\kappa$  of most metals is yet to be fully understood. One such topic is how the lattice  $\kappa$  of metals is affected by electrons. Even though electron density is not the sole factor to determine the electron-phonon coupling constant  $G_{ep}$ , it could shed some light on a qualitative estimation of the relative magnitude of  $G_{ep}$  in materials. In low-doped semiconductors and insulators, which have very low electron density, phonon scattering by electrons is much rarer than scattering by other phonons at temperatures around or above the Debye temperature. For heavily-doped semiconductors, semimetals, and metals, however, the high electron density might lead to a different story. For example, it was reported that phonon-electron (p-e) scattering could reduce the phonon lifetime significantly in heavily-doped silicon. [178] Moreover, it is well known that there is a wide span of  $G_{ep}$  in metals. [162] For instance,  $G_{ep}$  is on the order of  $1 \times 10^{16}$  W/m<sup>2</sup>-K in copper (Cu), silver (Ag), and gold (Au) at room temperature, while it is on the order of  $1 \times 10^{17} \sim 10^{18}$  W/m<sup>3</sup>-K in aluminum (Al), platinum (Pt), and nickel (Ni). [162] As the magnitude of  $G_{ep}$  characterizes the strength of scattering of electrons by phonons, it is thereby natural to expect that the scattering of phonons by electrons is stronger in Al, Pt, and Ni than in Cu, Ag, and Au. Phonon transport in metals is limited by phonon scattering by various sources, for example, phonons,

electrons, impurities, and defects, etc. At temperatures comparable to or above the Debye temperature, phonon-phonon (p-p) scattering is believed to dominate phonon relaxation in Cu, Ag, and Au while p-e scattering is neglected. [179] However, it is unclear whether p-e scattering is also negligible in metals known to have stronger electron-phonon coupling than Cu, Ag, and Au. Moreover, as illustrated in literature, [23, 24], the effective thermal boundary resistance of a metal-dielectric interface is proportional to  $\kappa_L^{-0.5}$ . Therefore, an accurate knowledge of  $\kappa_L$  is important for thermal modeling of metal-dielectric systems.

In this chapter, we present first-principles calculations of p-p and p-e scattering rates in Cu, Ag, Au, Al, Pt, and Ni. With these quantities, we are able to compute the lattice  $\kappa$  of these metals and evaluate the relative importance of p-p and p-e scattering on lattice  $\kappa$ .

## 6.2 Methodology

A phonon is a quantum of lattice vibration and can be described with a quantum number  $\lambda = (\nu, \mathbf{q})$ , where  $\mathbf{q}$  denotes wave vector and  $\nu$  denotes branch index. A phonon can be scattered through interaction with other phonons, electrons, impurities, etc. The overall scattering rate of a phonon mode can be estimated by the Matthiessen's rule as  $\gamma_\lambda = \gamma_\lambda^{pp} + \gamma_\lambda^{pe} + \dots$ , where  $\gamma_\lambda^{pp}$  and  $\gamma_\lambda^{pe}$  are scattering rates of p-p and p-e scattering, respectively. In this work,  $\gamma^{pp}$  and  $\gamma^{pe}$  will be calculated separately, both from first-principles, of which the details are described below.

### 6.2.1 Phonon-phonon Scattering

The p-p scattering contribution (three-phonon process only) to  $\gamma_\lambda$  is given by the Fermi's golden rule (FGR) as [180, 181]

$$\gamma_\lambda^{pp} = \frac{\hbar\pi}{4N} \sum_{\lambda_1\lambda_2}^+ 2 \frac{n_1 - n_2}{\omega\omega_1\omega_2} |V_{\lambda\lambda_1\lambda_2}^+|^2 \delta(\omega + \omega_1 - \omega_2) + \frac{\hbar\pi}{8N} \sum_{\lambda_1\lambda_2}^- \frac{n_1 + n_2 + 1}{\omega\omega_1\omega_2} |V_{\lambda\lambda_1\lambda_2}^-|^2 \delta(\omega - \omega_1 - \omega_2), \quad (6.1)$$

where the first term on the right hand side is for phonon absorption (two phonons combine into one) while the second term is for phonon emission (one phonon splits into two). In addition,  $N$  is the number of discrete  $\mathbf{q}$  points of the  $\Gamma$ -centered  $\mathbf{q}$  grid for sampling the first Brillouin zone (FBZ),  $\hbar$  is the reduced Planck constant,  $n$  is the Bose-Einstein distribution function, and  $\omega$  is the phonon frequency. The summation  $\sum^{\pm}$  over phonon modes requires conservation of quasimomentum:  $\mathbf{q}_2 = \mathbf{q} \pm \mathbf{q}_1 + \mathbf{Q}$ , in which  $\mathbf{Q}$  is the reciprocal lattice vector with  $\mathbf{Q} = 0$  denoting normal process while  $\mathbf{Q} \neq 0$  denoting Umklapp process.  $\delta$  is the Dirac delta function, which is approximated by a Gaussian or Lorentzian function in practice. The terms  $V_{\lambda\lambda_1\lambda_2}^{\pm}$  are the scattering matrix elements, which are calculated as [181]

$$V_{\lambda\lambda_1\lambda_2}^{\pm} = \sum_{l_1}^{N_b} \sum_{l_2, l_3}^{N, N} \sum_{\alpha_1 \alpha_2 \alpha_3}^{3, 3, 3} \frac{\partial^3 E}{\partial r_{l_1}^{\alpha_1} \partial r_{l_2}^{\alpha_2} \partial r_{l_3}^{\alpha_3}} \frac{e_{\lambda}^{\alpha_1}(l_1) e_{j_1, \pm \mathbf{q}_1}^{\alpha_2}(l_2) e_{j_2, -\mathbf{q}_2}^{\alpha_3}(l_3)}{\sqrt{m_{l_1} m_{l_2} m_{l_3}}}, \quad (6.2)$$

where  $m$  is the atomic mass and  $e_{\nu, \mathbf{q}}$  is the normalized eigenvector of the phonon mode  $\lambda = (\nu, \mathbf{q})$ . In Eq. (6.2),  $l_1$ ,  $l_2$ , and  $l_3$  run over atomic indices ( $l_1$  runs over only the atoms in the center unit cell, which contains  $N_b$  basis atoms), and  $\alpha_1, \alpha_2$ , and  $\alpha_3$  represent Cartesian coordinates. The third-order partial derivative is the anharmonic interatomic force constant (IFC) obtained from first-principles, in which  $E$  is the total energy of the whole system and  $r_{l_1}^{\alpha_1}$  denotes the  $\alpha_1$  component of the displacement of atom  $l_1$ .

In addition to third-order IFCs for Eq. (6.2), one also needs the eigenvalues and eigenvectors of phonon modes to compute  $\gamma_{\lambda}^{pp}$  based on Eqs. 6.1-6.2. The eigenvalues and eigenvectors are obtained from lattice dynamics calculations that require second-order IFCs. In this work, the second-order IFCs are obtained through Fourier transforming reciprocal-space dynamical matrices calculated from the linear-response theory, which is implemented in Quantum ESPRESSO [182, 183]. Force constants obtained in this way suffers less error due to long-range interactions than another widely used method, the small-displacement method. [184] The third-order IFCs are obtained through a finite-difference supercell approach, in which Quantum Espresso is used to compute the forces for a minimal set of displaced supercell configurations.

In all the density-functional theory (DFT) calculations, the Troullier-Martins normconserving pseudopotentials are used. DFT calculations for second-order IFCs are conducted with a  $\mathbf{k}$ -space sampling and integration on a  $24 \times 24 \times 24$  Monkhorst-Pack grid and an energy cut-off of  $E_{\text{cut}}$  for the truncation of the plane wave basis set.  $E_{\text{cut}}$  is set to be 100 Ry for Cu, Ag, Au and 120 Ry for Al, Pt, and Ni. In all cases, a Marzari-Vanderbilt cold smearing of 0.02 Ry is used to speed up the convergence of the self-consistent calculations. A  $\mathbf{q}$ -grid with  $5 \times 5 \times 5$   $\mathbf{q}$  points is used for Cu, Ag, and Au, while a denser  $\mathbf{q}$ -grid of  $16 \times 16 \times 16$  is used for Al, Pt, and Ni. The convergence of phonon dispersion with respect to  $\mathbf{k}$ -grid density,  $\mathbf{q}$ -grid density, energy cut-off, and smearing energy has been carefully checked, and the aforementioned values of these parameters ensure convergence within about 2% on phonon frequencies at  $\Gamma$  and  $X$  points and less than 0.001 Ry/atom difference in energy. DFT calculations for third-order IFCs are performed on supercells containing  $4 \times 4 \times 4$  primitive unit cells. A  $\Gamma$ -point algorithm in Quantum ESPRESSO is used for Cu, Ag, and Au for efficient DFT calculation while a  $3 \times 3 \times 3$   $\mathbf{k}$ -grid is used for Al, Pt, and Ni.

Two types of exchange-correlation functionals are used, i.e., Generalized Gradient Approximation (GGA) [185] and Local Density Approximation (LDA) [186]. Generally speaking, LDA tends to overestimate bonding energies and underestimate bond lengths, and vice versa for GGA. Since the harmonic and anharmonic IFCs are derivatives of the energy, as a general rule both sets of constants will be larger in magnitude when computed using the LDA. Accordingly, phonon frequencies and scattering rates are usually overestimated by LDA while underestimated by GGA. This, however, might lead to a fictitious cancelation of error for the prediction of thermal conductivity, which is positively correlated to phonon frequencies (heat capacity) while negatively correlated to scattering rates. Finally, the second-order and third-order IFCs are feeded to ShengBTE [187] to obtain  $\gamma_{\lambda}^{pp}$  on a  $16 \times 16 \times 16$   $\mathbf{q}$ -grid.

### 6.2.2 Phonon-electron Scattering

The phonon-electron scattering rate from the FGR is computed as [180]

$$\gamma_{\lambda}^{pe} = \frac{2\pi}{\hbar} \sum_{\mathbf{k}, i, j} |g_{j\mathbf{k}+\mathbf{q}, i\mathbf{k}}^{\lambda}|^2 f_{i\mathbf{k}} [1 - f_{j\mathbf{k}+\mathbf{q}}] \times \{n_{\lambda} \delta[\epsilon_{i\mathbf{k}} - \epsilon_{j\mathbf{k}+\mathbf{q}} + \hbar\omega_{\lambda}] - (n_{\lambda} + 1) \delta[\epsilon_{i\mathbf{k}} - \epsilon_{j\mathbf{k}+\mathbf{q}} - \hbar\omega_{\lambda}]\}, \quad (6.3)$$

where  $g$  is the electron-phonon matrix element,  $f$  is the Fermi-Dirac distribution function,  $\mathbf{k}$  is the electron wavevector,  $i$  and  $j$  are electron band indices,  $\epsilon$  is the electron energy, and  $\omega$  is the phonon frequency. The electron-phonon matrix element is calculated as

$$g_{j\mathbf{k}+\mathbf{q}, i\mathbf{k}}^{\lambda} = \sqrt{\frac{\hbar}{2\omega_{\lambda}}} \langle \psi_{j\mathbf{k}+\mathbf{q}} | \partial U_{\lambda} | \psi_{i\mathbf{k}} \rangle, \quad (6.4)$$

which describes the transition of an electron at a Bloch state  $i\mathbf{k}$  into another state at  $j\mathbf{k} + \mathbf{q}$  by a phonon at state  $\lambda = (\mathbf{q}, \nu)$ . In Eq. (6.4),  $\psi$  is a ground-state Bloch wavefunction and  $U$  is the self-consistent Kohn-Sham potential felt by electrons, which depends on the atomic positions.  $\partial U_{\lambda}$  denotes the first-order derivative of the Kohn-Sham potential with respect to phonon displacement. Details regarding this quantity can be found in literature. [188]

Under the relaxation time approximation, the scattering rate (inverse lifetime) of phonon mode  $\lambda$  is [189]

$$\gamma_{\lambda}^{pe} = \frac{1}{\tau_{\lambda}^{ep}} = \frac{2\pi}{\hbar} \sum_{\mathbf{k}, i, j} |g_{j\mathbf{k}+\mathbf{q}, i\mathbf{k}}^{\lambda}|^2 [f_{i\mathbf{k}} - f_{j\mathbf{k}+\mathbf{q}}] \times \delta(\epsilon_{i\mathbf{k}} - \epsilon_{j\mathbf{k}+\mathbf{q}} + \hbar\omega_{\lambda}). \quad (6.5)$$

As we can see, the rate for the scattering of a phonon by electrons only depends on the number of electron states ( $f$ ) available under the relaxation time approximation, while phonon distribution  $n$  is not present in Eq. (6.6).

Since the energy span of phonons is much smaller than that of electrons, Eq. (6.5) can be approximated as

$$\gamma_{\lambda}^{pe} \approx 2\pi\omega_{\lambda} \sum_{\mathbf{k}, i, j} |g_{j\mathbf{k}+\mathbf{q}, i\mathbf{k}}^{\lambda}|^2 \frac{\partial f(\epsilon_{i\mathbf{k}}, T)}{\partial \epsilon} \times \delta(\epsilon_{i\mathbf{k}} - \epsilon_{j\mathbf{k}+\mathbf{q}} + \hbar\omega_{\lambda}), \quad (6.6)$$

where  $\partial f/\partial \epsilon$  is a “Fermi window” that peaks at the Fermi level. An important property of this function is that it broadens as temperature increases with its integral over the full  $\epsilon$ -space always being unity. In other words, p-e scattering rate is essentially a weighted average of p-e scattering matrix elements for electron states near the Fermi surface that satisfy energy conservation enforced by the Dirac delta function. Eq. (6.5) indicates that in order to have low/high p-e scattering rates, the metal should have small/large scattering matrix element  $g$  and low/high electron density of states (eDOS) in the Fermi window.

The electron-phonon matrix elements are calculated using ABINIT [190] using the same Troullier-Martins normconserving pseudopotentials as those for IFC calculations. The electron-phonon matrix elements are evaluated on a  $16 \times 16 \times 16$   $\mathbf{k}$ -grid and a  $16 \times 16 \times 16$   $\mathbf{q}$ -grid. In fact, even with a coarser  $12 \times 12 \times 12$   $\mathbf{k}$ -grid and a  $12 \times 12 \times 12$   $\mathbf{q}$ -grid, the values of  $\gamma^{pe}$  differ by no more than 5% in most cases, which suggests the values of  $\gamma^{pe}$  obtained on the  $16 \times 16 \times 16$   $\mathbf{k}$ -grid and  $\mathbf{q}$ -grid pair should be well converged.

### 6.2.3 Lattice Thermal Conductivity

Finally, the lattice thermal conductivity tensor can be calculated as

$$\kappa_{L,\alpha\beta} = \sum_{\lambda} c_{v,\lambda} v_{\lambda,\alpha} v_{\lambda,\beta} \tau_{\lambda}, \quad (6.7)$$

where  $c_{v,\lambda}$  is the volumetric specific heat of a phonon mode  $\lambda$  and is calculated as

$$c_{v,\lambda} = (\hbar\omega_{\lambda})^2 n_{\lambda} (n_{\lambda} + 1). \quad (6.8)$$

Since it is almost impossible to verify our calculations on p-p and p-e scatterings directly, we will compare our results of lattice constants (a), phonon dispersion relations, and electron-phonon coupling parameter  $\lambda^{ep}$ , which is also referred to as the mass enhancement factor, with literature values. The phonon dispersions are presented in Fig. 6.1-6.5, and  $\lambda^{ep}$ 's are calculated using the formalism described in Ref. [193] and listed in Tab. 7.1. We can see that the calculated  $\lambda^{ep}$  generally fall in



Table 6.1. Material properties of Cu, Ag, Au, Al, Pt, and Ni. The 2nd column is the electron configuration of these elements. Columns 3 and 4 are the lattice constants calculated through structural relaxation in this work using LDA and GGA, respectively, while column 5 shows the experimental data. Columns 6 and 7 are the electron-phonon mass enhancement parameter ( $\lambda^{ep}$ ) calculated in this work using LDA and GGA, respectively, and column 8 lists the data from literature.

Material	e <sup>-</sup> configuration	$a_{\text{LDA}}$ (Å)	$a_{\text{GGA}}$ (Å)	$a_{\text{exp.}}$ (Å)	$\lambda_{\text{LDA}}^{ep}$	$\lambda_{\text{GGA}}^{ep}$	$\lambda_{\text{literature}}^{ep}$
Cu	[Ar]3d <sup>10</sup> 4s <sup>1</sup>	3.668	3.553	3.610	0.138	0.142	0.13 [191]
Ag	[Kr]3d <sup>10</sup> 4s <sup>1</sup>	4.210	4.067	4.090	0.135	0.160	0.12 [191]
Au	[Xe]3d <sup>10</sup> 4s <sup>1</sup>	4.183	4.075	4.080	0.189	0.212	0.15 [191]
Al	[Ne]3s <sup>2</sup> 3p <sup>1</sup>	4.046	3.961	4.050	0.377	0.389	0.38 [192]
Pt	[Xe]4f <sup>14</sup> 5d <sup>9</sup> 6s <sup>1</sup>	3.995	3.914	3.920	0.559	0.612	0.66 [191]
Ni	[Ar]4s <sup>2</sup> 3d <sup>8</sup>	3.544	3.441	3.520	0.239	0.257	0.31 [191]

the range of literature values. This means that our calculation can at least capture electron-phonon interactions near the Fermi surface with reasonable accuracy.

It is worth noting that, since GGA considers the gradient of the charge density at each position, it generally works better for molecules in which there are abrupt charge density changes with respect to position, whereas LDA works better for metallic systems. [194] However, we will see that GGA results agree better with experimental data of lattice constant, phonon dispersion relations, and electron-phonon mass enhancement factor than LDA for certain metals. Therefore, in this work, we present the results from both LDA and GGA approximations.

## 6.3 Results and Discussions

### 6.3.1 Cu, Ag, and Au: Noble Metals with Weak Electron-phonon Interaction

Cu, Ag, and Au are noble metals sharing several attributes such as low electrical resistivity and high ductility. All three metals have a single s-orbital electron on top of a fully filled d-orbital electron shell. As a result, the Fermi level of Cu, Ag, and Au lies on the s-band, which has low eDOS, as shown in Fig. 6.1a, Fig. 6.2a, and Fig. 6.3a. This, as discussed in Ref. [162], leads to a low  $G_{ep}$ , which characterizes how fast the thermal energy in hot electrons can be transferred into phonons in the material. [162] Moreover, the s-bands of these metals are rather flat and the d-bands of these metals are well below the Fermi level, and even the Fermi window for 1,000 K shown in Figs. 6.1a, 6.2a, and 6.3a has no visible overlap with the d-bands, which suggests insignificant change in electron-phonon interactions below 1,000 K. Since they have low  $g$  and low eDOS in the Fermi window, these metals are expected to have low p-e scattering rates, according to Eq. (6.6).

The phonon dispersion relations of Cu, Ag, and Au in the  $\Gamma$ - $X$  direction in the FBZ calculated in this work as well as experimental data [195, 197, 198] are shown in the inset of Fig. 6.1a, Fig. 6.2a, and Fig. 6.3a. As we can see, GGA predicts better phonon

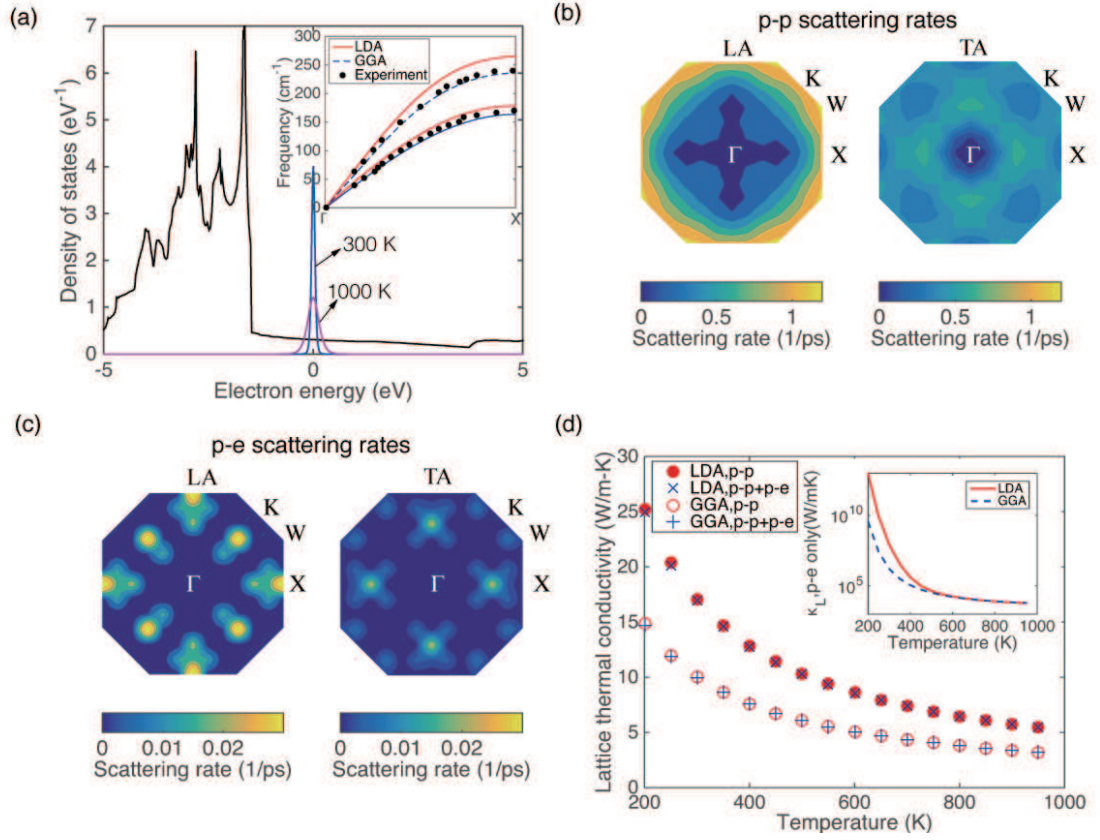


Figure 6.1. Results for Cu. (a) Electronic density of states as well as the Fermi window at 300 K and 1,000 K. All data in this panel and below are obtained under the GGA approximation otherwise mentioned. The inset shows the phonon dispersion relations calculated in this work as well as experimental data. [195] (b) and (c) Contour plot of the p-p and p-e scattering rates in the  $k_x$ - $k_y$  plane of the FBZ. (d) Lattice thermal conductivity computed from first-principles with the LDA and GGA approximations with and without the effect of p-e scattering. The inset shows  $\kappa_L$  when only p-e scattering is considered. Figure reproduced from Ref. [196].

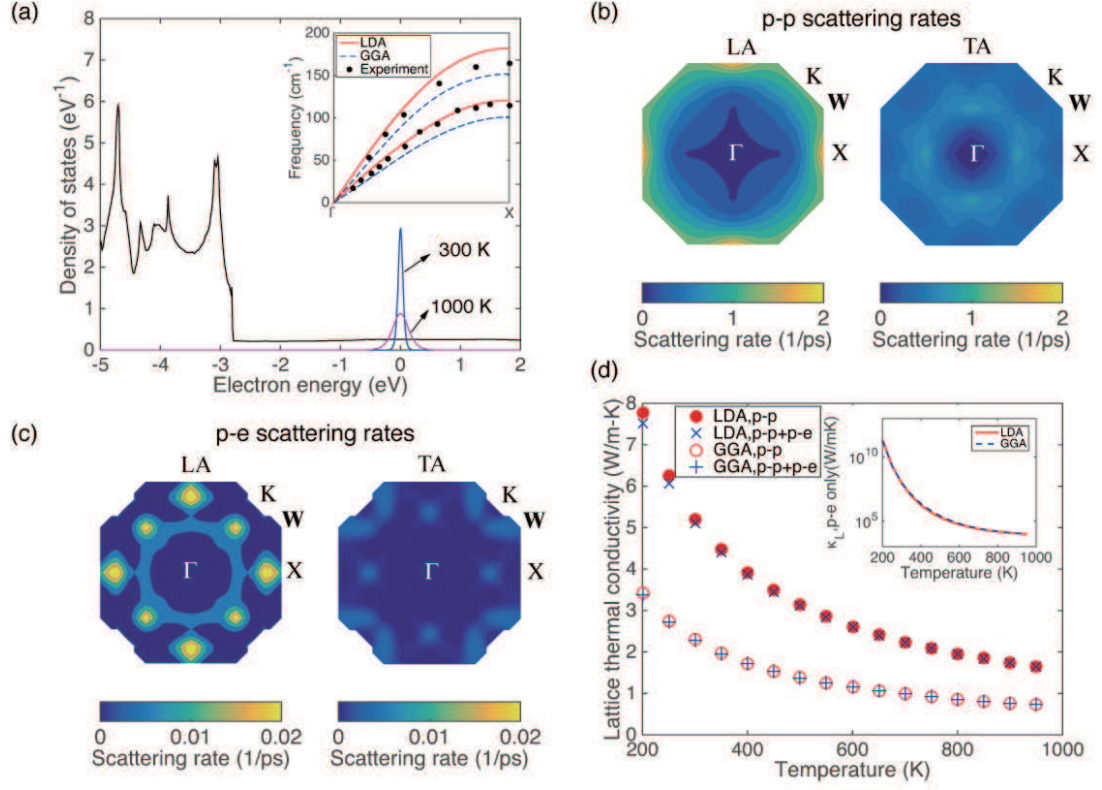


Figure 6.2. Results for Ag. (a) Electronic density of states as well as the Fermi window at 300 K and 1,000 K. All calculations are obtained under the LDA approximation otherwise mentioned. The inset shows the phonon dispersion relations in the  $\Gamma$ -X direction in the FBZ calculated in this work as well as experimental data. [197] (b) and (c) Contour plot of  $\gamma^{pp}$  and  $\gamma^{pe}$  in the  $k_x$ - $k_y$  plane of the FBZ of Ag. (d)  $\kappa_L$  with and without the effect of electron-phonon scattering. The inset shows  $\kappa_L$  when only p-e scattering is considered. Figure reproduced from Ref. [196].

dispersion relations for Cu, while LDA works better for Ag and Au. Specifically, the frequency of the longitudinal acoustic (LA) branch of Cu is overestimated by LDA while the frequency of both the LA and transverse acoustic (TA) branches of Ag and Au are underestimated by GGA, which agrees with previous DFT calculations. [179] Figures 6.1b and c show the room-temperature p-p and p-e scattering rates, or,  $\gamma^{pp}$  and  $\gamma^{pe}$ , in the  $k_x$ - $k_y$  plane of the FBZ.  $\gamma^{pp}$  is on the order of  $1 \text{ ps}^{-1}$ , similar to that of Si, while  $\gamma^{pe}$  is generally two orders of magnitude lower than  $\gamma^{pp}$ . It is worth mentioning that, even with an electron density of  $\sim 8.5 \times 10^{22} \text{ cm}^{-3}$ , the  $\gamma^{pe}$  of the LA branch of Cu is on the same order of magnitude as the  $\gamma^{pe}$  of the LA phonons and one order of magnitude lower than that of the LO phonons in heavily-doped Si with a carrier concentration of  $1 \times 10^{21} \text{ cm}^{-3}$ . [178] This is also true for Ag and Au, both of which are characterized by weak p-e scattering, as shown in Figs 6.2b, 6.2c, 6.3b, and 6.3c.

We can also see that the  $\gamma^{pp}$ 's of Cu, Ag, and Au are on the same order of magnitude. However, since they have very different atomic masses, with Cu the lightest while Au the heaviest, the lattice thermal conductivity  $\kappa_L$  of them differs significantly owing to the difference in phonon group velocities. As shown in Figs. 6.1d, 6.2d, and 6.3d, the  $\kappa_L$  of Cu is the highest among the three metals, while that of Au is the lowest. In all cases,  $\kappa_L$  decreases with temperature due to enhanced p-p scattering. In addition, the  $\kappa_L$  from LDA and GGA can differ by as much as 50% in certain cases. We suggest using the values from GGA for Cu while those from LDA for Ag and Au, as they predict more accurate phonon dispersions than the other for the corresponding material. It is worth mentioning that Makinson's model [199] predicts a converged  $\kappa_L$  in the high-temperature limit when only p-e scattering is considered, while Ziman's model [200] predicts a diverged  $\kappa_L$ . In our work, which considers detailed electronic band structure near the Fermi surface,  $\kappa_L$  is found to decrease with increasing  $T$  between 200-900 K for Cu, Ag, and Au.

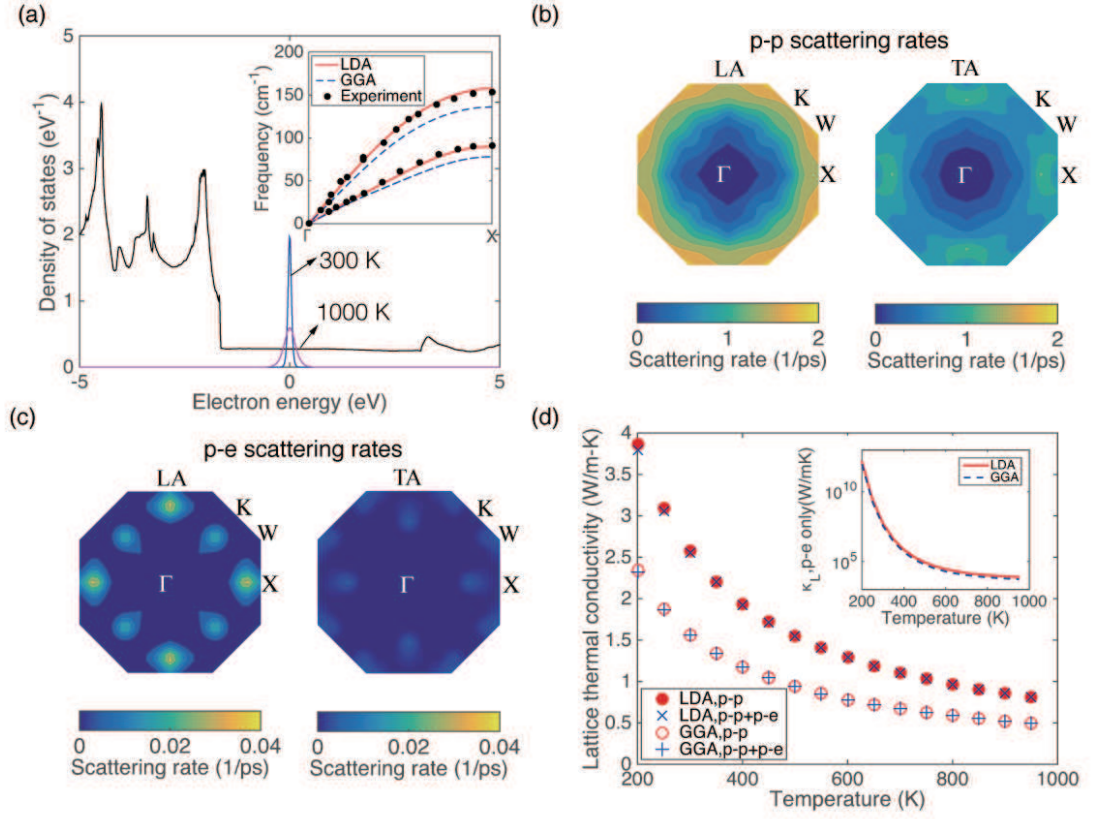


Figure 6.3. Results for Au. (a) Electronic density of states as well as the Fermi window at 300 K and 1,000 K. All calculations are obtained under the LDA approximation otherwise mentioned. The inset shows the phonon dispersion relations calculated in this work as well as experimental data. [198] (b) and (c) Contour plot of  $\gamma^{pp}$  and  $\gamma^{pe}$  in the  $k_x$ - $k_y$  plane of the FBZ. (d)  $\kappa_L$  with and without the effect of electron-phonon scattering. The inset shows  $\kappa_L$  when only p-e scattering is considered. Figure reproduced from Ref. [196].

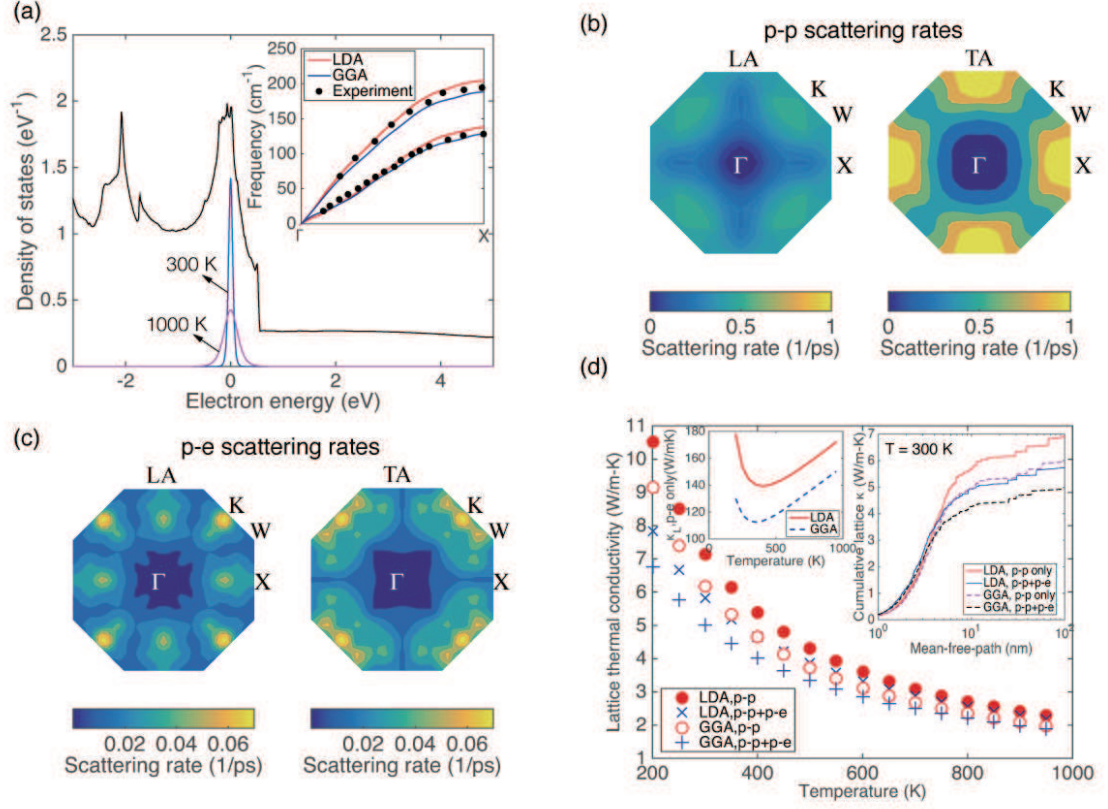


Figure 6.4. Results for Pt. (a) Electronic density of states as well as the Fermi window at 300 K and 1,000 K. All calculations are obtained under the LDA approximation otherwise mentioned. The inset shows the phonon dispersion relations calculated in this work as well as experimental data (dark symbols). [201] (b) and (c) Contour plot of  $\gamma^{pp}$  and  $\gamma^{pe}$  in the  $k_x$ - $k_y$  plane of the FBZ. (d)  $\kappa_L$  with and without the effect of electron-phonon scattering. The inset at the upper left corner shows  $\kappa_L$  when only p-e scattering is considered, and the inset at the upper right corner shows the cumulative thermal conductivity with respect to phonon mean-free-path at 300 K. Figure reproduced from Ref. [196].

### 6.3.2 Pt and Ni: d-band Metals with Strong Electron-phonon Interaction

Pt and Ni are d-band metals, which are characterized by a Fermi level located at the d-band (overlapped with s-band and p-band) with high eDOS. Therefore, e-ph

interaction can be very strong in these materials since there are many electron states available for e-p scattering. The strong e-p interaction is manifested by a high e-p coupling constant  $G_{ep}$  on the order of  $10^{18} \text{W/m}^3\text{-K}$  at room temperature, which is two orders of magnitude higher than that of Cu, Ag, and Au. [162]

Figure 6.4a shows the eDOS of Pt, in which the Fermi level is located at the d-band. Evidently, the eDOS at the Fermi level for Pt is much higher than that for Cu, Ag, and Au in Figs. 6.1a, 6.2a, and 6.3a. The inset of Fig. 6.4a shows the phonon dispersion relations. As we can see, LDA predicts more accurate phonon dispersion relations for Pt than GGA.

Figures 6.4b and c show the  $\gamma^{pp}$  and  $\gamma^{pe}$  of Pt.  $\gamma^{pe}$  is roughly on the same order of magnitude as, though still lower than,  $\gamma^{pp}$ . In particular,  $\gamma^{pp}$  is lower near the center of the FBZ, which indicates that p-e scattering is relatively more significant than at the boundary. The inset of Fig. 6.4d displays the cumulative thermal conductivity of Pt with respect to phonon mean-free-path (MFP). As we can see, most of the  $\kappa_L$  is contributed by phonons with MFP in the range of 1-10 nm. Moreover, phonons with longer MFP ( $> 5$  nm) are more significantly affected by p-e scattering than those with shorter MFP, since the long-MFP phonons are mostly modes near the FBZ center with relatively weaker p-p scattering. The discrepancies between the  $\kappa_L$  predicted from the LDA and GGA approximations are not as much as those for Cu, Ag, and Au. In particular, the short MFP region of the cumulative thermal conductivity curves agree with each other very well. In Fig. 6.4d, we can see that p-e scattering reduces the  $\kappa_L$  by 15% at room temperature, and it is even more important at sub-room-temperature regime, where Umklapp p-p scattering becomes weaker while p-p scattering is less affected.

Figure 6.5a shows the eDOS of Ni, which, similar to Pt, has high eDOS at the Fermi level. The inset shows the phonon dispersion curves. Evidently, the results from GGA agree with experimental data much better than those from LDA. Figure 6.5b and 6.5c are  $\gamma^{pp}$  and  $\gamma^{pe}$  of Ni. Similar to Pt,  $\gamma^{pp}$  and  $\gamma^{pe}$  are comparable to each other. In Fig. 6.5d, we can see that the p-e scattering reduces  $\kappa_L$  significantly by about



30% at room temperature and is even more important at sub-room-temperatures. The cumulative  $\kappa_L$  curve in the inset of Fig. 6.5d indicates that p-e scattering substantially affects the  $\kappa_L$  of phonon modes with a wide span of MFP, not just limited to long-MFP ones as in Pt. Unlike Cu, Ag, and Au,  $\kappa_L$  increases with  $T$  in the high-temperature regime when only p-e scattering is considered, which seems to support Ziman's model. [200] Finally, it is worth mentioning that, considering its total thermal conductivity of 91 W/m-K at room temperature, the  $\kappa_L$  of Ni is comparable to the electronic thermal conductivity. This is unlike most metals in which the lattice thermal conductivity is much lower than the electronic part.

### 6.3.3 Al: Metal with Intermediate Electron-phonon Coupling Constant

Aluminum, as a prototype of free-electron-like metals, is among the first metals that are studied ab initio. The quadratic-shape eDOS shown in Fig. 6.6a is one signature of the free-electron nature of Al. The  $\gamma^{pp}$  and  $\gamma^{pe}$  of Al are shown in Fig. 6.6b and Fig. 6.6c. A somewhat unexpected feature of the  $\gamma^{pe}$  data is that it is much lower than  $\gamma^{pp}$ , contrary to the common notion that it is a metal with a quite high  $G_{ep}$  (for example,  $G_{ep} = 2.46 \times 10^{17} \text{ W/m}^3\text{-K}$  at room temperature in Ref. [162]). Moreover, Fig. 6.6d shows that p-e scattering has negligible effect on the  $\kappa_L$  of Al, unlike Ni and Pt. In fact, the  $G_{ep}$  of Al is about one order of magnitude lower than that of Ni and Pt. A rough estimation of  $\gamma^{pe}$  is  $G_{ep}/c_p$ . With  $c_p$  similar between Ni, Al, and Pt, the difference in  $G_{ep}$  suggests  $\gamma^{pe}$  should also be much lower in Al than the other two, which agrees with our results. Moreover, the highest  $\gamma^{pe}$  occurs in the high frequency spectrum of phonons (near the boundary of the FBZ), while these phonons only contribute a small amount of heat transfer to the overall  $\kappa_L$ .

## 6.4 Summary

To conclude, we extracted from first-principles the phonon scattering rates in several metals considering the contribution from both p-p and p-e scattering processes.

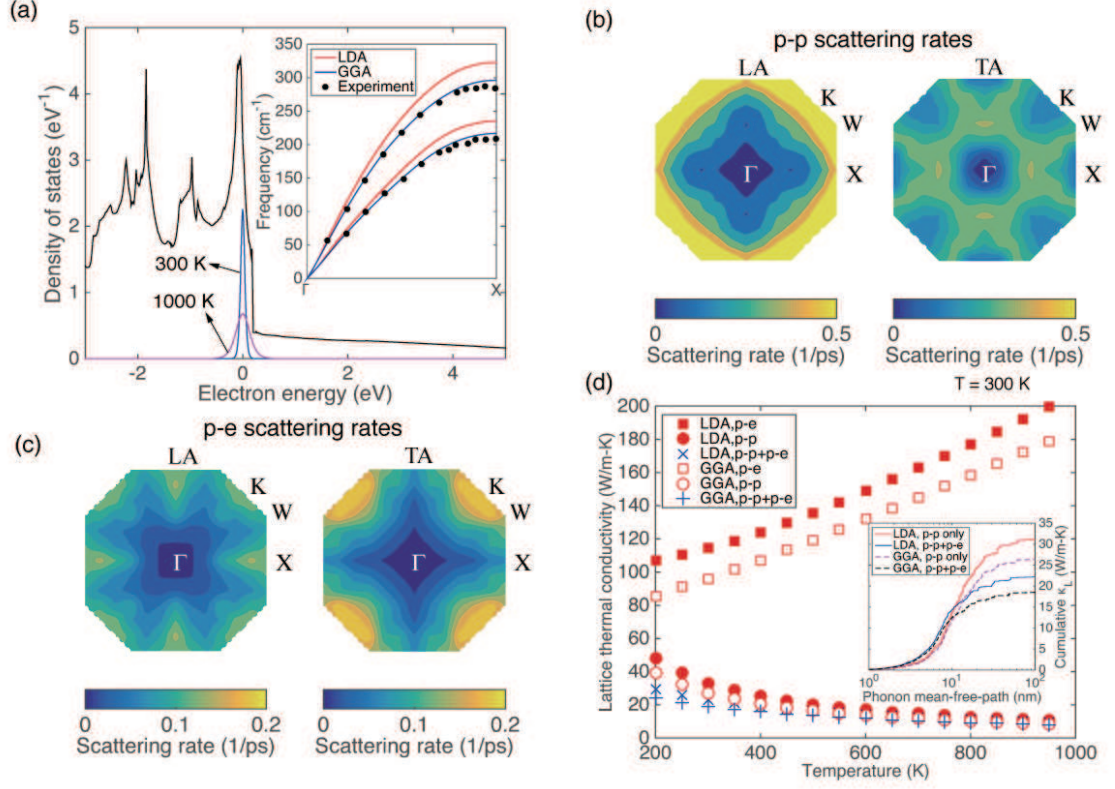


Figure 6.5. Results for Ni. (a) Electronic density of states as well as the Fermi window at 300 K and 1,000 K. All calculations are obtained under the GGA approximation otherwise mentioned. The inset shows the phonon dispersion relations calculated in this work as well as experimental data (dark symbols). [202] (b) and (c) Contour plot of  $\gamma^{pp}$  and  $\gamma^{pe}$  in the  $k_x$ - $k_y$  plane of the FBZ. (d)  $\kappa_L$  considering p-e scattering only, p-p scattering only, and both p-e and p-p scattering. The inset shows the cumulative thermal conductivity with respect to phonon mean-free-path at 300 K. Figure reproduced from Ref. [196].

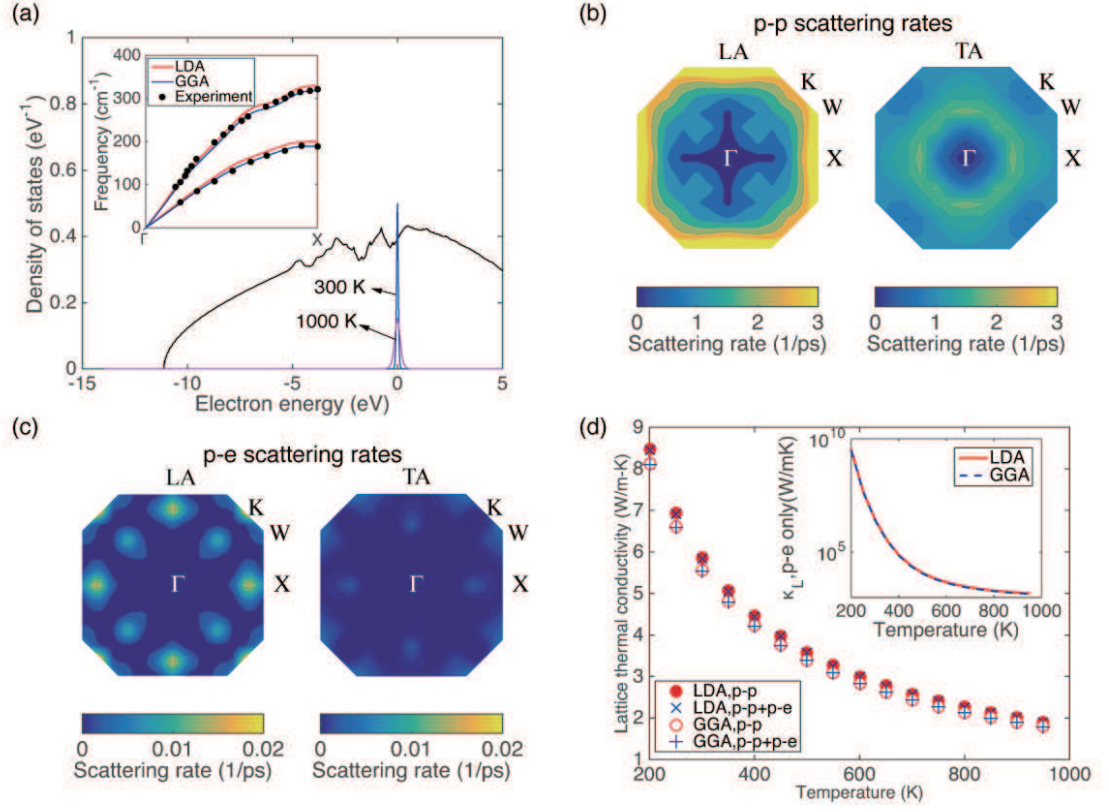


Figure 6.6. Results for Al. (a) Electronic density of states as well as the Fermi window at 300 K and 1,000 K. All calculations are obtained under the GGA approximation otherwise mentioned. The inset shows the phonon dispersion relations calculated in this work as well as experimental data (dark symbols). [203] (b) and (c) Contour plot of  $\gamma^{pp}$  and  $\gamma^{pe}$  in the  $k_x$ - $k_y$  plane of the FBZ. (d)  $\kappa_L$  with and without the effect of electron-phonon scattering. The inset shows  $\kappa_L$  when only p-e scattering is considered. Figure reproduced from Ref. [196].

It was found that p-e scattering is negligible in Cu, Ag, Au, and Al while it is significant in Pt and Ni at room temperature. Specifically, the room temperature  $\kappa_L$  of Cu, Ag, Au, and Al predicted from density-functional theory calculations with the local-density approximation are 16.9, 5.2, 2.6, and 5.8 W/m-K, respectively, when only p-p scattering is considered. p-e scattering was found to be negligible in determining  $\kappa_L$ . In contrast, the room-temperature  $\kappa_L$  of Pt and Ni is reduced from 7.1 and 33.2 W/m-K to 5.8 and 23.2 W/m-K by p-e scattering. Moreover, the effect of p-e scattering on lattice thermal conductivity becomes stronger at sub-room-temperature range.

## 7. TWO-TEMPERATURE BOLTZMANN TRANSPORT EQUATION SIMULATION OF THERMAL TRANSPORT ACROSS LAYERED METAL-NONMETAL STRUCTURES

### 7.1 Introduction

In addition to engineering the thermal conductivity of materials for thermal management, previous studies have also demonstrated various schemes to manipulate thermal transport across solid-solid interfaces, for example, introduction of interface roughness, hierarchical alignment of multiple interfaces, and insertion of an interlayer with intermediate vibrational properties between the two materials. The aforementioned schemes primarily focus on engineering phonon transport, while much less attention was paid to the electron side. Moreover, it was revealed that electron-phonon interaction plays an important role in thermal transport across metal-dielectric interfaces, [23, 24] suggesting the feasibility of controlling interfacial thermal transport by manipulating the electron degree-of-freedom.

The coexistence of electron and phonon channels, however, makes thermal transport occur in a rather complicated manner. In pump-probe experiments, for instance, laser radiation rapidly elevates the electron temperature to thousands of Kelvin in a time scale of tens to hundreds of femtoseconds, while the lattice (phonons) remains cool. Subsequently, the deposition of heat from hot electrons to cold phonons occurs in a time scale of the order of electron-phonon relaxation time (1-10 ps), which renders the electrons and phonons almost in thermal equilibrium with each other yet still at a temperature higher than the substrate. Finally, the gradual heat dissipation across the interface and then into the substrate starts to dominate in a time span of nanoseconds. Obviously, the transient thermal process described above is characterized by the dominance of different thermal transport channels in a sequential

manner. In contrast, steady-state thermal transport reflects the summation of all the existing channels. A rigorous understanding of the above thermal transport processes is therefore important for the management of the overall heat transfer characteristics of electronic and photonic devices.

In this chapter, we strive to understand various heat transfer pathways and evaluate the effect of interlayer on interfacial thermal transport and hot electron cooling dynamics in metal-dielectric systems. Herein we perform simulations including relevant electron-phonon coupling and phonon transmission processes to show that applying an appropriate interlayer can be a practical way to enhance thermal transport across metal-dielectric interfaces. Moreover, we also evaluate the effect of interlayer on hot electron cooling dynamics during ultrafast laser heating. We will show that this is of practical importance because of interlayer's two competing effects on a device: on one hand, it reduces lattice heating and thereby extending device lifetime; on the other hand, it accelerates the energy loss of hot electrons, which degrades energy efficiency.

## 7.2 Two-temperature Boltzmann Transport Equation

We combine the BTE method with the two-temperature model (TTM) by including an electron-phonon coupling term in both the phononic and the electronic BTEs,

$$\frac{\partial e_e}{\partial t} + \mathbf{v}_e \cdot \nabla e_e = \frac{e_e^0 - e_e}{\tau_e} - G_{ep}(T_e - T_p) + \dot{r}_e, \quad (7.1a)$$

$$\frac{\partial e_p}{\partial t} + \mathbf{v}_p \cdot \nabla e_p = \frac{e_p^0 - e_p}{\tau_p} + G_{ep}(T_e - T_p) + \dot{r}_p, \quad (7.1b)$$

where  $e_e$  and  $e_p$  are the energy density of electrons and phonons, respectively, and  $G_{ep}$  is the electron-phonon coupling constant.  $e_e$  and  $e_p$  are related to the electron and phonon temperatures via  $e_e = 0.5\gamma_e T_e^2$  and  $e_p = C_p T_p$  (classical limit), where  $\gamma_e$  is the electron heat capacity constant and  $C_p$  is the phonon heat capacity. In addition,  $\mathbf{v}$  denotes velocity,  $\tau$  is relaxation time, and  $\dot{r}$  is volumetric heat generation rate.

The lattice Boltzmann method [204] (LBM) is used to solve the above BTE equations in the metal film. The simulation domain is divided into discrete grids (finite volumes) of size  $\Delta x^d$ , with  $d$  denoting the dimension. In the two-temperature BTE, Eqs. 7.1a and 7.1b are discretized as follows

$$e_{e,\alpha,x+\Delta x_e,t+\Delta t} = (1 - w_e)e_{e,\alpha,x,t} + w_e e_{e,\alpha,x,t}^0 - G_{ep} \left[ \frac{e_{e,\alpha,x,t}^0}{c_e} - \frac{e_{p,\alpha,x,t}^0}{c_p} \right] \Delta t, \quad (7.2a)$$

$$e_{p,\alpha,x+\Delta x_p,t+\Delta t} = (1 - w_p)e_{p,\alpha,x,t} + w_p e_{p,\alpha,x,t}^0 + G_{ep} \left[ \frac{e_{e,\alpha,x,t}^0}{c_e} - \frac{e_{p,\alpha,x,t}^0}{c_p} \right] \Delta t, \quad (7.2b)$$

where  $\alpha$  is the index for transport directions, which is either forward  $+$  or backward  $-$  in the 1D BTE here.  $e_e^0$  and  $e_p^0$  are the equilibrium energy density of electrons and phonons, which are approximated as  $(e_{e,+} + e_{e,-})/2$  and  $(e_{p,+} + e_{p,-})/2$ , respectively. In addition,  $w_e = \Delta t/\tau_e$  and  $w_p = \Delta t/\tau_p$ , where  $\tau_e$  and  $\tau_p$  denote the relaxation time of electrons and phonons, respectively. In this work the computational grid size is mode-dependent, that is,  $\Delta x_e = v_e \Delta t$  and  $\Delta x_p = v_p \Delta t$ , which is different from the mode-dependent time step size scheme used in previous LBM-based BTE calculations. [205] We note that  $v_e \gg v_p$  in most metals and semiconductors, with the former usually being close to the Fermi velocity  $v_f$  (on the order of  $1 \times 10^6$  m/s) and the latter approximately being the phonon group velocity  $v_s$  (on the order of  $1 \times 10^3$  m/s). The great mismatch between  $v_f$  and  $v_s$  makes  $\Delta x_e$  and  $\Delta x_p$  differ by almost three orders of magnitude. As a result, each electron grid is coupled to thousands of phonon grids.

The fact that the thickness of the thin film is usually between 20-200 nm while the substrate is usually much thicker renders a full BTE calculation for both sides rather computationally demanding, especially when multiple phonon modes or electron modes are included. Because the substrate is usually much thicker than the mean-free-path of the heat carriers, we use the diffusive TTM,

$$C_e \frac{\partial T_e}{\partial t} = \nabla \cdot (\kappa_e \nabla T_e) - G_{ep}(T_e - T_p) + \dot{r}_e, \quad (7.3a)$$

$$C_p \frac{\partial T_p}{\partial t} = \nabla \cdot (\kappa_p \nabla T_p) + G_{ep}(T_e - T_p) + \dot{r}_p, \quad (7.3b)$$

to model the heat transfer in the substrate. In the above equations,  $C$ ,  $T$ ,  $\kappa$ , and  $\dot{r}$  are the heat capacity, temperature, thermal conductivity, and volumetric heat generation rate of electrons (subscript  $e$ ) and phonons (subscript  $p$ ), respectively.  $G_{ep}$  is the electron-phonon coupling constant, which describes the strength of thermal coupling between electrons and phonons.

In the diffusive TTM calculation, the phonon channel and the electron channel are discretized uniformly with the same  $\Delta x_F$ , and Eq. (7.3a) and Eq. (7.3b) are discretized and rearranged as

$$T_{e,x,t+\Delta t} = (1 - 2\alpha_e - \beta_{ep})T_{e,x,t} + \alpha_e(T_{e,x+\Delta x_F,t} + T_{e,x-\Delta x_F,t}) + \beta_{ep}T_{p,x,t}, \quad (7.4a)$$

$$T_{p,x,t+\Delta t} = (1 - 2\alpha_p - \beta_{pe})T_{p,x,t} + \alpha_p(T_{p,x+\Delta x_F,t} + T_{p,x-\Delta x_F,t}) + \beta_{pe}T_{e,x,t}, \quad (7.4b)$$

where  $\alpha_e = \Delta t \kappa_e / [c_e (\Delta x_F)^2]$ ,  $\beta_{ep} = \Delta t G_{ep} / c_e$ ,  $\alpha_p = \Delta t \kappa_p / [c_p (\Delta x_F)^2]$ , and  $\beta_{pe} = \Delta t G_{ep} / c_p$ . This coupled BTE-Fourier scheme is able to capture the ballistic nature of heat transfer in the metal film and account for the diffusive thermal transport inside the substrate effectively and efficiently, which has been used for phonon transport previously. [206]

### 7.3 Input Parameters

The BTE simulation described in the last section requires several input parameters: velocity  $v$ , heat capacity  $c$  (or the electron heat capacity constant  $\gamma$ ), and lifetime  $\tau$  of electrons and phonons, as well as the electron-phonon coupling constant  $G_{ep}$ . The values of  $v_e$ ,  $\gamma$ , and  $G_{ep}$  can be obtained from literature, while the calculation of other parameters is presented in this section.



### 7.3.1 Bulk Properties: $v_p$ , $c_p$ , $\tau_p$ , and $\tau_e$

In metals, both phonon and electron contribute to thermal transport. As the total thermal conductivity  $\kappa_{tot}$  and electrical conductivity  $\sigma$  of metals are usually available, one can roughly estimate the phononic part based on

$$\kappa_{tot} = \kappa_p + \kappa_e, \quad (7.5)$$

in which the electronic thermal conductivity  $\kappa_e$  can be estimated by the Wiedemann-Franz law,

$$\kappa_e = LT\sigma, \quad (7.6)$$

where  $L$  is the Lorenz number. The Sommerfield value of  $2.44 \times 10^{-8} \text{W}\Omega\text{K}^{-2}$  was derived for  $L$  in degenerate metals, semi-metals, or semiconductors. However, we note that Eq. (7.5) is a rather rough approach to estimate  $\kappa_p$ .<sup>1</sup> Herein we adopt the  $\kappa_p$ , heat capacity, and phonon dispersion relations obtained from first-principles calculations in the last chapter. We will solve the BTE equations under a gray approximation where average phonon properties are used.  $v_p$  is calculated as the average Brillouin Zone center group velocity (in the  $\Gamma$ -X direction) of the three acoustic branches as

$$v_p^{-1} = (v_{LA}^{-1} + v_{TA,1}^{-1} + v_{TA,2}^{-1})/3, \quad (7.7)$$

where LA and TA (two branches) denote the longitudinal and transverse acoustic branch, respectively. The average phonon relaxation time  $\tau_p$  is estimated from the kinetic theory,

$$\kappa_p = c_p v_p^2 \tau_p / 3. \quad (7.8)$$

It is worth mentioning that even though such gray approximation has been widely used to interpret experiments, it inherently neglects the influence of spectral phonon and electron properties on heat transfer. In this work, we deliberately choose to use a gray model because it is accurate enough to capture the effect of interlayer on the

---

<sup>1</sup>For example, the  $\kappa_p$  of Nickel based on Eq. (7.5) is  $91 \text{ W/m-K} - 2.44 \times 10^{-8} \times 300 \times 1.43 \times 10^7 \text{ W/m-K} = -14 \text{ W/m-K}$ , which is not physical.

Table 7.1. Average phonon and electron properties of Au, Al, Pt, and Si used in the BTE or Fourier calculations. Table reproduced from Ref. [207].

Quantity	Au	Al	Pt	Si
$v_p$ ( $\times 10^3$ m/s)	1.85	3.43	1.91	6.40
$c_p$ ( $\times 10^6$ J/m <sup>3</sup> -K)	2.40	2.43	2.67	1.66
$\tau_p$ (ps)	0.95	0.58	1.79	6.53
$\kappa_p$ (W/m-K)	2.6	5.5	5.8	148.0
$\kappa_{tot}$ (W/m-K)	314.0 [208]	205.0 [208]	71.6 [208]	148.0
$\kappa_e$ (W/m-K)	311.4	199.5	65.8	N/A
$v_e$ ( $\times 10^6$ m/s)	1.40 [209]	2.03 [209]	0.46	N/A
$\gamma_e$ (W/m <sup>3</sup> -K <sup>2</sup> )	62.9 [162]	91.2 [162]	748.1 [162]	N/A
$\tau_e$ (fs)	25.3	5.3	4.1	N/A
$G_{ep}$ ( $\times 10^{16}$ W/m <sup>3</sup> -K)	2.6 [162]	24.6 [162]	108.7 [162]	N/A

overall heat transfer characteristics of the system of interest, while a more complicated spectral model is not necessary.

After we obtain  $\kappa_p$ ,  $\kappa_e$  can be obtained by Eq. (7.5) with a knowledge of the experimental value of the total thermal conductivity. The relaxation time of electrons can be estimated in a similar way as Eq. (7.8) for phonons. Table 7.1 lists the average phonon and electron properties of Au, Al, Pt, and Si to be used in the BTE simulations.

### 7.3.2 Interfacial Thermal Transport Properties

**Phonon transmission** We use the diffuse mismatch model (DMM) to calculate phonon transmission coefficients. The  $R_{pp}$  between two materials is computed using full phonon dispersion relations over the entire first Brillouin zone (FBZ) as [210]

$$R_{pp}^{-1} = G_{pp} = \frac{1}{V_{\text{FBZ}} N_k} \sum_{\nu \mathbf{k}, v_{\nu \mathbf{k}Ax} > 0} \frac{(\hbar \omega_{\nu \mathbf{k}})^2}{k_B T^2} v_{\nu \mathbf{k}Ax} \Xi_{AB, \nu \mathbf{k}} f(\omega_{\nu \mathbf{k}}, T) [f(\omega_{\nu \mathbf{k}}, T) + 1], \quad (7.9)$$

where  $V_{\text{FBZ}}$  is the volume of the FBZ,  $\hbar$  is the reduced Planck constant,  $N_k$  is the number of grids we have divided the FBZ into, that is,  $16 \times 16 \times 16$  uniform grids of volume  $\Delta V_A$  and  $\Delta V_B$ . In addition,  $v_{\nu \mathbf{k}Ax}$  is the group velocity of a phonon mode with wavevector  $\mathbf{k}$  and polarization  $\nu$  in material A projected in the  $x$  direction, and  $f$  is the distribution function. The elastic phonon transmission coefficient  $\Xi_{AB}$  for phonon transmission from material A to material B is calculated using DMM as

$$\Xi_{AB}(\omega) = \frac{\Delta V_B \sum_{\nu \mathbf{k}} v_{\nu \mathbf{k}Bx} \delta_{\omega_{\nu \mathbf{k}}, \omega}}{\Delta V_A \sum_{\nu \mathbf{k}} v_{\nu \mathbf{k}Ax} \delta_{\omega_{\nu \mathbf{k}}, \omega} + \Delta V_B \sum_{\nu \mathbf{k}} v_{\nu \mathbf{k}Bx} \delta_{\omega_{\nu \mathbf{k}}, \omega}}, \quad (7.10)$$

where  $\delta_{\omega_{\nu \mathbf{k}}, \omega}$  is the Kronecker delta function. The  $R_{pp}$ 's of Au-Si, Au-Al, Au-Pt, Al-Si, and Pt-Si as a function of temperature computed in this way are plotted in Fig. 7.1b. It is worth mentioning that the vibrational density of states of Al and Pt are between those of Au and Si, as shown in Fig. 7.1a. As a result, both the  $G_{pp}$  of Au-Al/Pt and that of Al/Pt-Si are higher than the  $G_{pp}$  of Au-Si. Therefore, adding a thin layer of Al or Pt to Au-Si interface should not increase the effective interfacial thermal resistance significantly in terms of phonon transport. Later we will see that a thin Al or Pt interlayer could even enhance interfacial thermal transport by reducing the nonequilibrium between electrons and phonons near the interface.

**Electron transmission** Electron transmission across the interface between metal and low-doped semiconductor is usually a thermionic emission process, which has an effective thermal conductance lower than or comparable to its phonon counterpart. Moreover, the very low density of free electrons (or holes) in the low-doped semiconductor renders it difficult for electronic heat to be dissipated further into the sub-

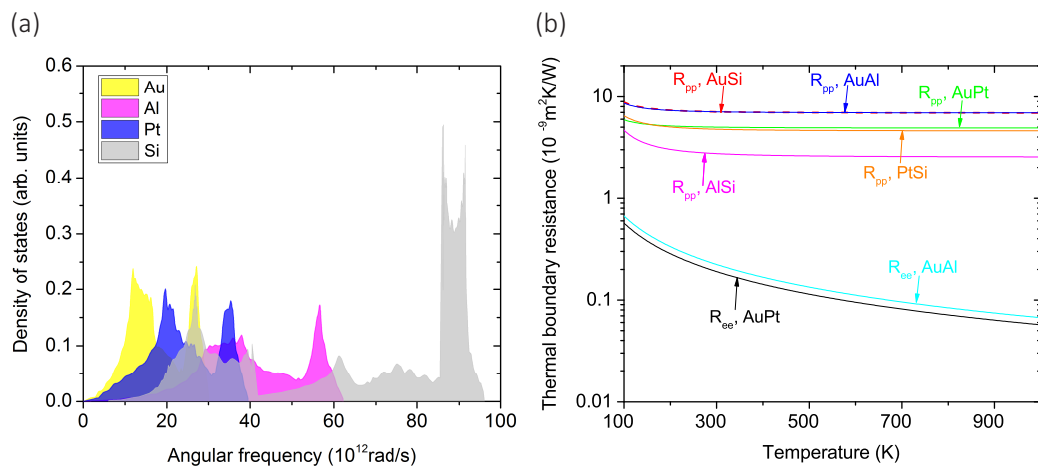


Figure 7.1. (a) The vibrational density of states of Au, Al, Pt, and Si. (b) The interfacial thermal resistance, electronic ( $R_{ee}$ ) or phononic ( $R_{pp}$ ), for various interfaces. Figure reproduced from Ref. [207].

strate. Therefore, the electron transmission channel is negligible in metal-low-doped semiconductor systems.

For electron transport across the interface between two metals, Gundrum et al. extended the DMM for phonon to electron. [211] Specifically, the electronic interfacial thermal resistance  $R_{ee}$  can be computed as

$$R_{ee}^{-1} = G_{ee} = \frac{Z_A Z_B}{4(Z_A + Z_B)}, \quad (7.11)$$

where  $Z_A = c_{e,A} v_{e,A}$  and  $Z_B = c_{e,B} v_{e,B}$ . As shown in Fig. 7.1b, the computed  $R_{ee}$ 's are 1-2 orders of magnitude lower than corresponding  $R_{pp}$ 's but are very close to the  $R_{ee}$ 's measured in Gundrum et al.'s experiments for metal-metal interfaces. [211]

## 7.4 Results and Discussions

### 7.4.1 Steady-State Thermal Transport

In practical applications, a thin Cr, Ti, or Pt layer is usually deposited on the Si substrate before the deposition of the Au layer as an adhesion layer or diffusion barrier. It has been reported that a Ti interlayer at the Au-Si interface can enhance the effective thermal conductance significantly owing to the enhanced bonding at the interface. [212] We note that Al and Pt have 1-2 orders of magnitude higher  $G_{ep}$  than Au, which may reduce the interfacial thermal resistance due to electron-phonon nonequilibrium near the interface. To assess this effect, we calculate the effective  $R$  for Au-Si interfaces with and without an interlayer of Al or Pt, of which the schematics are shown in Fig. 7.2a.

In our simulations, we maintain the surface of the Au film, as shown in Fig. 7.2a, at 310 K while the bottom of the Si substrate at 290 K. The effective interfacial thermal resistance  $R_{\text{eff}}$  is computed as

$$R_{\text{eff}} = \frac{20\text{K}}{J} - \frac{l_{\text{Au}}}{\kappa_{\text{Au}}} - \frac{l_{\text{Si}}}{\kappa_{\text{Si}}}, \quad (7.12)$$

where  $J$  is the heat flux (in W/m<sup>2</sup>), and  $l_{\text{Au}}$  and  $l_{\text{Si}}$  are the thickness of the Au and Si segment respectively.

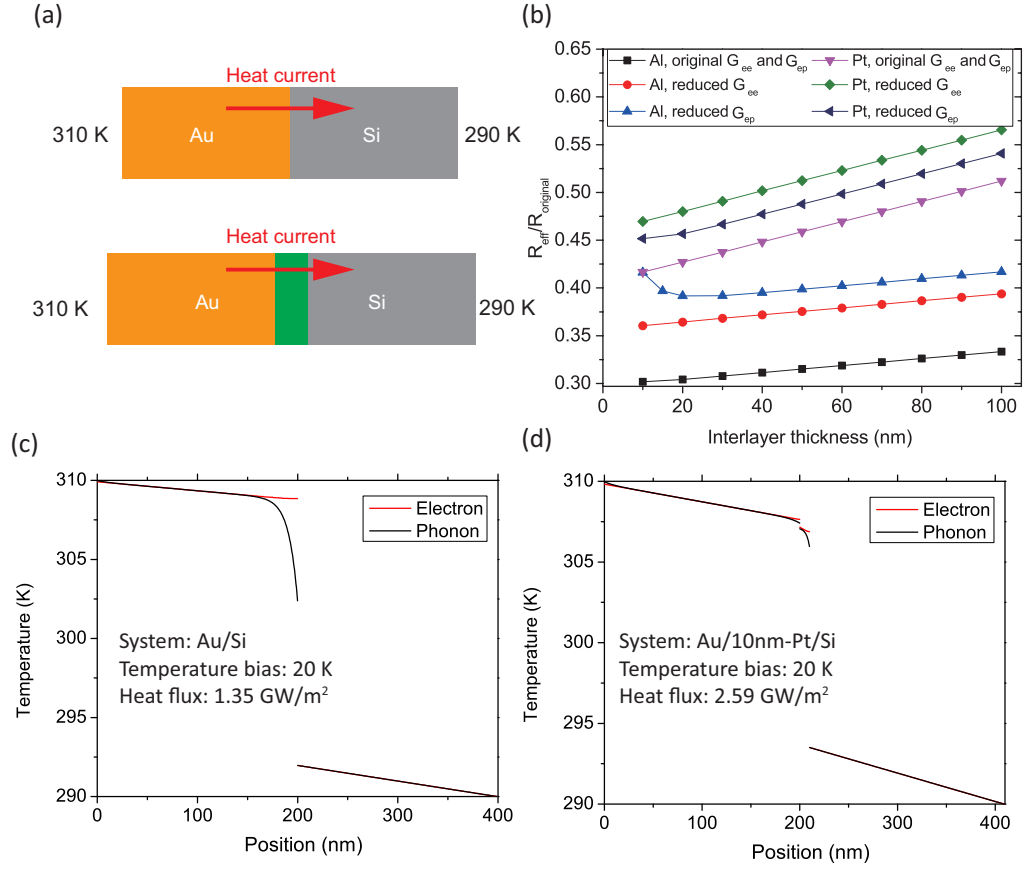


Figure 7.2. (a) Schematic illustration of the simulated Au-Si and Au-interlayer-Si systems. (b) The ratio of the effective interfacial thermal resistance,  $R_{\text{eff}}$ , to the original interfacial thermal resistance,  $R_{\text{original}}$ , as a function of interlayer thickness. (c) and (d) Temperature profiles of electron and phonon obtained in the simulation. Figure reproduced from Ref. [207].

In Fig. 7.2b we show the effective interfacial thermal resistance normalized by that of a direct Au-Si interface ( $R_{\text{original}} = 1.33 \times 10^{-8} \text{m}^2 \text{K/W}$ ) as a function of interlayer thickness. To account for the possibility of non-ideal contact between the Au film and the interlayer, which causes lower  $G_{ee}$ , additional simulations using 20% of the theoretical value of  $G_{ee}$  predicted by Eq. (7.11) are also conducted. The artificially reduced  $G_{ee}$ 's are much lower than the experimental values for metal-metal interfaces reported in Ref. [211], therefore we assert that it can well represent the lower limit of the  $G_{ee}$  of well-welded Au-Al and Au-Pt interfaces. As we can see in Fig. 7.2b, for both ideal or non-ideal contact cases, the interfacial thermal resistance is reduced significantly by the interlayer, suggesting the robustness of this scheme to enhance interfacial thermal transport.  $R_{\text{eff}}$  is higher when  $G_{ee}$  is lower as it becomes more difficult for hot electrons in the Au film to transport into the Al or Pt interlayer and then equilibrate with phonons. Moreover, the effective interfacial thermal resistance  $R_{\text{eff}}$  increases with interlayer thickness, since the thermal resistance of the interlayer itself increases as  $l_{\text{interlayer}}/\kappa_{\text{interlayer}}$ .

Figure 7.2c and 7.2d are the temperature profiles of electron and phonon obtained in our simulations on Au-Si and Au-Pt-Si systems. A notable electron-phonon nonequilibrium region can be seen near the interface in Fig. 7.2c, while this region is significantly reduced by the Pt interlayer, as shown in Fig. 7.2d. The elimination of the nonequilibrium region leads to reduced  $R_{\text{eff}}$ .

Therefore, we conclude that interlayers can significantly affect the thermal transport across metal/dielectric interfaces if the heat dissipation across the original interface is limited by large electron-phonon nonequilibrium. This is usually true for metals with weak electron-phonon coupling, for example, Cu, Ag, and Au, and interlayers with strong electron-phonon coupling, for example, Al, Pt, Cr, and Ti.

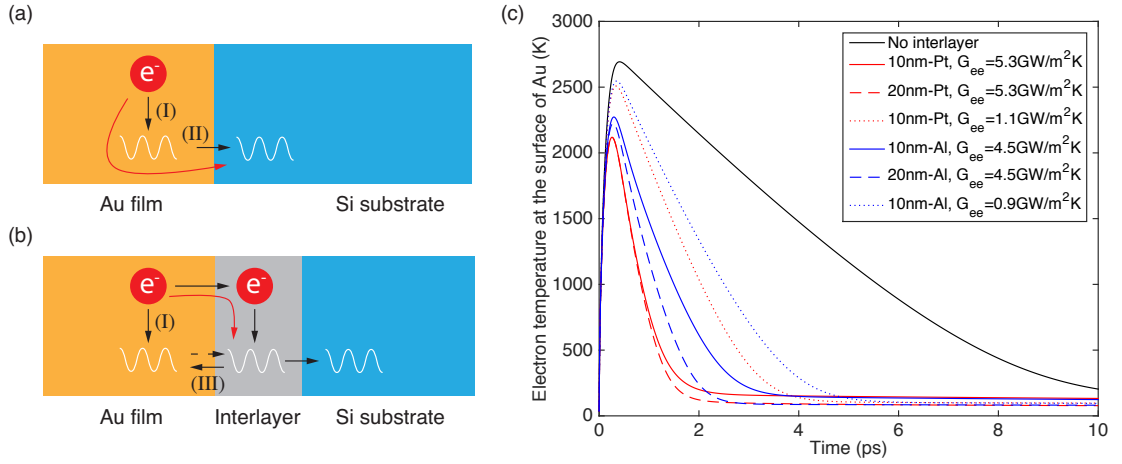


Figure 7.3. (a) Heat transfer channels in Au-Si without an interlayer. (I) and (II) denote lattice heat transfer channels, with (I) denoting electron-phonon coupling while (II) denoting phonon transmission into the substrate. (b) Heat transfer channels in Au-Si with an interlayer. (I) denotes the same process as that in (a), while (III) denotes backflow of heat from the hotter interlayer lattice to the Au lattice. The heat flow direction indicated by the dashed arrow is also possible, for example, when  $G_{ep}$  of the interlayer is lower than that of Au. (c) Transient electron temperature at the surface of a Au thin film for different interlayer thickness,  $G_{ee}$  between Au film and interlayer, and interlayer material. Figure reproduced from Ref. [207].



### 7.4.2 Ultrafast Electron Cooling in Au Thin Films

The pump-probe technique has been used to evaluate the electron-phonon coupling constant  $G_{ep}$  of metals. In a pump-probe measurement, a pump laser is injected to the metal thin film in which the temperature of electrons can be elevated to thousands of Kelvins in tens to hundreds of femtoseconds. Subsequently, the hot electrons are cooled down by the colder lattice, and the cooling curve allows one to evaluate  $G_{ep}$ . Similar process also happens in practical applications such as heat-assisted magnetic recording. In this section we assess the effect of interlayers on hot electron cooling dynamics in Au thin films.

The simulations are conducted to mimic Guo et al.'s pump-probe experiments [213], in which a pump laser with a pulse width of 390 fs was used. All the parameters of the laser in our simulations are the same as those in Ref. [213]. In Figs. 7.3a and b we show the possible heat transfer pathways in the Au-Si system without (a) and with (b) an interlayer. When Au is in direct contact with Si, initially hot electrons dissipate heat into the lattice through electron-phonon coupling, and then the hot Au lattice transfers heat into the Si lattice. When there is an interlayer between Au and Si, an additional channel is created, in which hot electrons carry heat into the interlayer and deposit heat into the interlayer lattice. If the interlayer has much higher  $G_{ep}$  than Au, the lattice temperature of the interlayer increases more quickly than Au. This leads to backflow of phononic heat from the interlayer to the Au lattice. The above heat transfer pathways are indicated as (I),(II), and (III), and their effect on lattice heating will be discussed later. The direction indicated by the dashed arrow for channel (III) is when the interlayer has lower  $G_{ep}$  than Au.

As shown in Fig 7.3c, the electron temperature increases to 2,000-3,000 K within hundreds of femtoseconds and then decreases at a much lower speed. Moreover, adding an interlayer accelerates hot electron cooling substantially. The acceleration arises from the new electron cooling channel created by the interlayer, as shown in Fig. 7.3b. Specifically, hot electrons in Au can readily transmit across the Au-Al

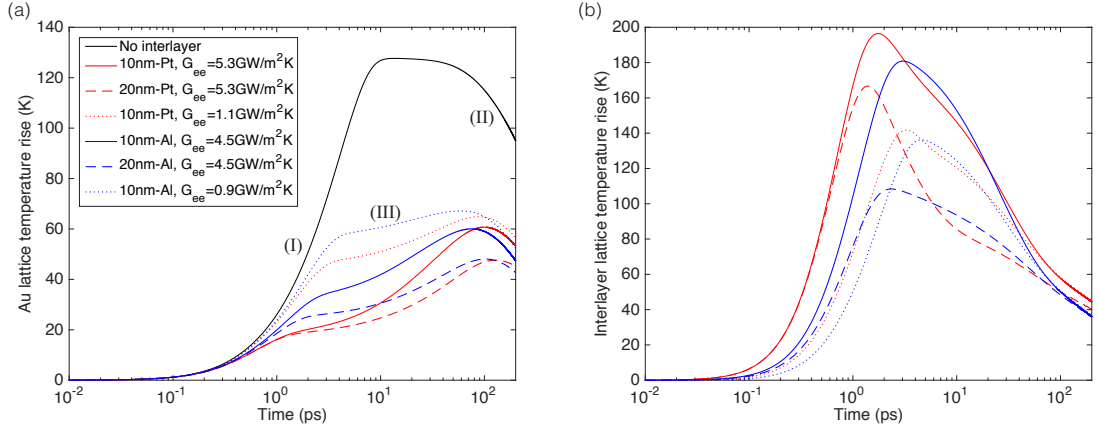


Figure 7.4. (a) Lattice temperature rise of the Au film as a function of time for different interlayer thickness or  $G_{ee}$ . A laser fluence of  $20 \text{ J/m}^2$  is used for all cases. The heating or cooling of the Au lattice is dominated by different mechanisms at different stages: (I) heat transfer from hot electrons; (II) heat dissipation into the substrate; (III) backflow of heat from the hotter interlayer lattice. (b) Lattice temperature rise of the interlayer as a function of time. Figure reproduced from Ref. [207].

or Au-Pt interface and then rapidly dissipate heat into the Al or Pt lattice due to their high  $G_{ep}$ . To consider the effect of interface nonideality, we also conduct additional simulations in which we reduce the  $G_{ee}$  of Au-interlayer interface to 20% of the theoretical value. It is obvious that even for the reduced  $G_{ee}$  cases, a Pt or Al interlayer can accelerate hot electron cooling substantially. We also study the effect of interlayer thickness by simulating two different structures: one with a 10-nm thick interlayer while the other with a 20-nm interlayer. As shown in Fig. 7.3c, electron temperature drops more quickly in the case with thicker interlayer. This is because a thicker interlayer has a larger volume  $V$  to absorb electronic heat through electron-phonon coupling, of which the heat transfer rate is on the order of  $G_{ep, \text{interlayer}} V_{\text{interlayer}}$ .

In Fig. 7.4a we show the lattice temperature rise ( $T_p - 300 \text{ K}$ ) as a function of time. As we can see, the lattice temperature of the Au film in the no-interlayer case increases at the beginning due to electron-phonon coupling (channel I), and decreases

thereafter due to heat dissipation into the substrate (channel II). The above two competing processes, I and II, lead to a maximum lattice temperature ( $T_{p,max}$ ), which is an important factor determining the lifetime of devices. In many applications, a high  $T_{p,max}$  degrades or even destroys the device and therefore should be minimized. As we can see, adding an interlayer of Al or Pt helps to reduce  $T_{p,max}$  significantly. For the cases with interlayers, as shown in Fig. 7.4a, the lattice temperature of Au increases at two distinctly different speeds. Similar to the no-interlayer case, the initial fast increase in  $T_p$  is due to electron-phonon coupling, while the subsequent slower increase is caused by phononic heat transfer from the hotter lattice of the interlayer (channel III). Moreover, thicker interlayer or higher  $G_{ee}$  between the Au film and the interlayer reduces  $T_{p,max}$  more significantly .

The above observations can be understood more clearly by Fig. 7.4b, where we plot the lattice temperature rise in the interlayer as a function of time. Comparing Fig. 7.4a and Fig. 7.4b, we can see that the temperature rise in the interlayer is much higher than that in the Au film. This is because the hot electrons in the Au film transfer heat into the interlayer quickly due to the high  $G_{ee}$  and then dissipate heat into the interlayer lattice rapidly due to the high  $G_{ep}$ . The above channel is much more efficient in transferring heat from hot electrons to the lattice than the electron-phonon coupling channel in the Au film, which has much lower  $G_{ep}$  than Pt and Al. As a result, most of the electron energy is deposited into the interlayer lattice rather than the Au lattice. Moreover, a higher  $G_{ee}$  leads to faster transfer of electronic heat from Au film to the interlayer and a thicker interlayer has a larger volume to absorb electronic heat, of which both reduce the lattice temperature rise in Au.

As a final remark of this section, we note that adding an interlayer of Al or Pt to the Au-Si interface has two-fold effects on the heat transfer characteristics of the system. On one hand, it accelerates hot electron cooling and thereby causes more energy loss, which should be minimized for energy efficiency; on the other hand, it reduces lattice heating in the Au thin film significantly, which could assist in maintaining a longer

device lifetime. This means that sophisticated thermal design is needed to achieve an optimal balance between device performance and lifetime.

## 7.5 Summary

We built a two-temperature Boltzmann transport equation method for modeling thermal transport in metal thin films. We compare the heat transfer rate from different interfacial thermal transport pathways for different film thickness and initial electron temperature. The results indicate that the direct interface electron-phonon coupling becomes more important when the metal film gets thinner. On the other hand, we also found that the electron transmission is negligible in terms of heat transfer in this model as there is not efficient channel to remove the heat from the hot electrons at the substrate surface, due to the low  $\kappa_e$  and  $g_{ep}$  in intrinsic or low-doped Si. However, this model only considers electronic heat transfer across the interface due to the thermionic emission, but not the number transfer to the substrate. At high temperatures, the emitted electrons dope the substrate, increasing its carrier density and consequently its  $\kappa_e$  and  $g_{ep}$ . This mechanism may decrease  $R_{pe}$  of the substrate significantly, which makes electron transmission an important mechanism.

## 8. MONTE CARLO BASED SPECTRAL BOLTZMANN SIMULATION OF ELECTRON-PHONON COUPLED THERMAL TRANSPORT ACROSS METAL-SEMICONDUCTOR INTERFACES

### 8.1 Introduction

An accurate predictive modeling of heat transfer is important for the design of novel materials and structures for various applications such as thermoelectrics and thermal management. Several methods have been developed to model heat transfer in solids. Classical molecular dynamics (MD) models the vibration of atoms based on the Newton's second law of motion. The interactions between atoms are described by empirical interatomic potentials. MD can directly model phonon transport and naturally account for atomic-level structural details, such as interfaces, defects, strain, surface reconstruction, etc. Schemes such as equilibrium/nonequilibrium MD, wave-packet method, and spectral energy density analysis have been used for modeling heat transfer or quantifying the contribution of individual phonon modes to thermal conductivity. The disadvantage of classical MD is also obvious. First, its accuracy is limited by the quality of empirical interatomic potentials, which were mostly developed for purposes other than heat transfer. Second, heat capacity in classical MD corresponds to the Dulong-Petit limit, while in a quantum system it increases from zero to the Dulong-Petit limit gradually as temperature increases. The above two issues usually make the accuracy of classical MD questionable when dealing with materials with a high Debye temperature.

First-principles-based methods enables a parameter-free calculation of phonon and electron properties, which have been used for evaluating the thermal properties of materials. The nonequilibrium Green's function (NEGF) approach has been used to calculate the thermal conductance of single materials and between different materials.

[60, 61, 152] Since harmonic force constants can be obtained from first-principles, NEGF used in this way is usually referred to as first-principles. One major drawback of current NEGF scheme is the complexity to include realistic anharmonic effects, therefore only harmonic force constants were used in most NEGF calculations.

First-principles molecular dynamics (FPMD) simulations, either in the form of NEMD or anharmonic lattice dynamics have been used to predict thermal conductivity of materials. [59, 214] However, limited by its high computational cost, small supercells and short simulation time were used in FPMD simulations. This restricts this approach for a wider application for materials with long phonon mean-free-path or long phonon relaxation time, which typically requires a large unit cell or a long simulation time. Anharmonic lattice dynamics can be used to predicted phonon properties based on force constants obtained from first-principles. This approach has been used under the relaxation time approximation (RTA) for evaluating the lattice thermal conductivity of materials. Beyond the RTA, Omini and Sparavigna [66] successfully solved the linearized Boltzmann equation iteratively, which was later adopted by Brodido and coworkers for calculating the lattice thermal conductivity of various materials in the last decade. [181] This method deals with three-phonon scattering processes in a self-consistent manner that deviation from Bose-Einstein distribution of phonons due to phonon-phonon scatterings are captured, which is important for materials with weak momentum-conserving process (or N-process) such as graphene.

To model heat transfer across solid-solid interfaces, various methods have been proposed and used. For example, the two-temperature molecular dynamics method has been used to simulate electron-phonon coupled thermal transport across interfaces, as discussed in Chapter 5. Besides, a gray, two-temperature Boltzmann transport equation method along with parameters obtained from first-principles was also used, as discussed in Chapter 7. To allow for first-principles based mode-wise simulation of electron-phonon coupled thermal transport, a Boltzmann transport equation framework is promising. However, as one can expect, it must involve complicated meshing for complicated geometries and. In fact, its computational cost is too high

even for most of the supercomputers. Monte Carlo technique has been used extensively to reduce the computational cost of such deterministic method at the sacrifice of accuracy. [215–218] In fact, as long as we include enough statistic samplings, for example, simulation time and number of phonon/electron modes, it is possible to achieve an acceptable accuracy. Mazumder and Majumdar proposed a Monte Carlo technique based on the assumption of small perturbations, in which all phonon modes are forced to equilibrium state at the end of every simulation step. [215] This was followed by Lacroix and Joulain, who improved the scheme by treating the normal process and Umklapp process of phonon-phonon scatterings differently. [216] Chen et al. proposed a genetic algorithm to model the normal process and Umklapp process separately and ensure the conservation of momentum and energy. [217] Péraud and Hadjiconstantinou proposed an energy-based variance-reduced Monte Carlo technique that reduces the computational cost significantly by simulating only the deviation from equilibrium. [218] This approach also adopts Mazumder and Majumdar’s scheme of small perturbation and therefore not suitable for simulating heat transfer under large perturbations.

In this work, we introduce a Monte Carlo approach to solve Boltzmann transport equations for mode-wise electron-phonon coupled thermal transport across metal-nonmetal interfaces. All the input parameters can be obtained from first-principles and the Fermi’s Golden Rule is used to evaluate the scattering rates of phonon-phonon processes on-the-fly. Specifically, phonons are modeled similar to Mazumder and Majumdar’s scheme but the requirement for thermodynamic equilibrium is relaxed. Electrons are modeled as a gray medium and implemented as local heat baths to phonons to reduce the computational cost. This method can be used for predictive simulation of heat transfer in nanodevices involving metal-nonmetal interfaces.

## 8.2 Methodology: Monte Carlo Boltzmann Solver

The phonon and electron Boltzmann transport equations are [180]

$$\frac{\delta N_\nu(r, q, t)}{\delta t} + v_{g,\nu}(r, q, t) \nabla \delta N_\nu(r, q, t) = \left[ \frac{\delta N_\nu(r, q, t)}{\delta t} \right]_{scattering}, \quad (8.1)$$

and

$$\frac{\delta f_\nu(r, k, t)}{\delta t} + v_{e,\nu}(r, k, t) \nabla \delta f_\nu(r, k, t) = \left[ \frac{\delta f_\nu(r, k, t)}{\delta t} \right]_{scattering}, \quad (8.2)$$

respectively, where  $N$  is the phonon number density,  $f$  is the electron number density,  $r$  is position,  $q$  is phonon wave vector,  $k$  is electron wave vector,  $t$  is time,  $\nu$  is the polarization of phonon wave vectors,  $\mu$  is the branch number in the electronic band structure,  $v_g$  is the group velocity of phonon modes, and  $v_e$  is the velocity of electrons (in many cases can be safely approximated as  $v_F$ , the Fermi velocity). The scattering terms on the right hand side of the equations determines how electron and phonon modes changes into others. The relaxation time approximation (RTA) is the most popular approximation of the scattering terms, in which the scattering rate for each phonon mode are modeled by a “relaxation time”  $\tau$ . In spectral simulations, different electron or phonon modes can have different  $\tau$ , where in gray simulations a common  $\tau$  is used for all modes.

In most of the BTE simulations of electrons or phonons, a constant or quasi-equilibrium relaxation time is used. However, it is possible that when the system is in nonequilibrium, for example, when the phonon distribution is distorted from the Bose-Einstein distribution or the electron distribution is distorted from the Fermi-Dirac distribution, it is possible that the relaxation time of a certain phonon or electron mode will be different from its quasi-equilibrium value (that calculated based on Bose-Einstein or Fermi-Dirac statistics). Therefore, a simulation that allows real-time calculation of scattering rates based on the local population of electron or phonon modes will be advantageous for highly nonequilibrium cases, for example, laser pump-probe experiments.

In this work, we propose a spectral Monte Carlo approach for electron-phonon coupled thermal transport, of which the flowchart is shown in Fig. 8.1. Specifically, we



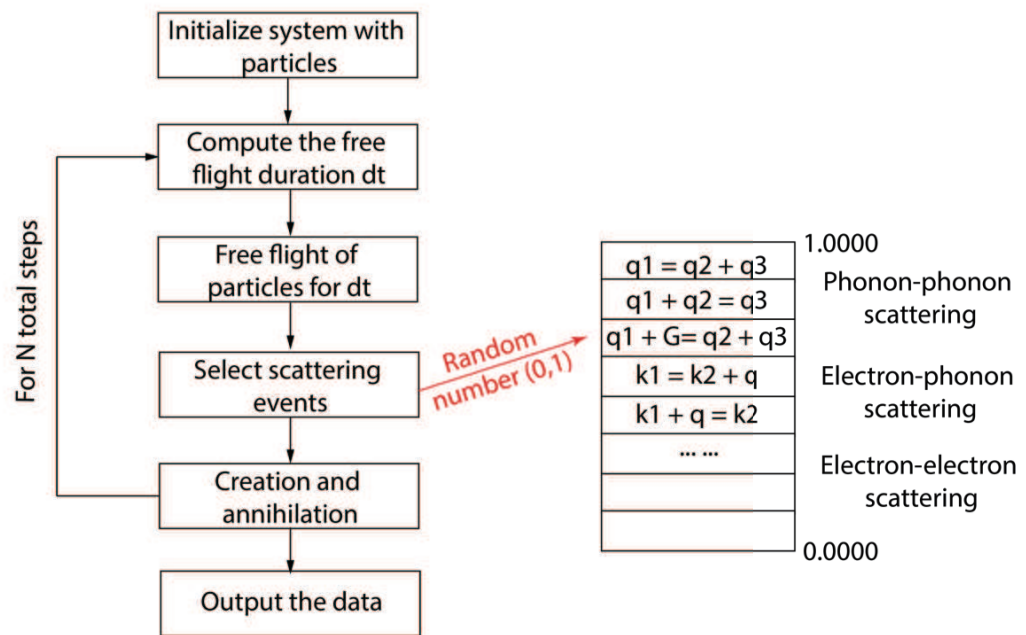


Figure 8.1. Flowchart of our Monte Carlo simulation of electron-phonon coupled thermal transport.

initialize the system with electron and phonon density profile  $f_\mu(r, k, 0)$  and  $N_\nu(r, q, 0)$  based on the local temperature. During each step, the heat carriers move by  $v \times dt$ . At the end of each step, scattering events are selected based on random numbers generate by pseudo-random number engines. The scattering rates can be determined in various way, from the conventional relaxation time approximation approaches to real-time Fermi's Golden Rule calculations based on the local electron and phonon density. Using the relaxation time approximation requires that a local equilibrium must be enforced each time step. In practice, phonon distribution is forced to follow a Bose-Einstein distribution after phonon-phonon scattering process (creation and annihilation process shown in Fig. 8.1), even if it has become a distorted, nonequilibrium distribution right after the scatterings. The above procedure is achieved by matching the total local energies of the as-obtained phonon distribution with an equilibrium Bose-Einstein distribution. As we can see, no non-equilibrium between phonons is allowed in such treatment. This method, though, saves a lot of computational efforts, ensures convergence of simulation in most cases, and allows simulation of large (microscale) system and long temporal scales (nanosecond-microsecond). In this work, in order to capture the nonequilibrium between phonon modes, we have relaxed the requirement of local equilibrium. In the simulation, we divide the simulation domain into cubic grids. Each phonon searches in the same grid for possible phonons to scatter with, i.e., those satisfying energy and momentum conservation (or quasi-momentum conservation for the Umklapp process). This is different from a realistic case, where each phonon might possibly scatter with phonons everywhere in the range of its path. However, the treatment of this range is approximated by this cutoff scheme based on the notion that there is a higher chance for phonons to scatter with phonons closer to themselves. More than 80% of the simulation time is consumed by the phonon searching process.

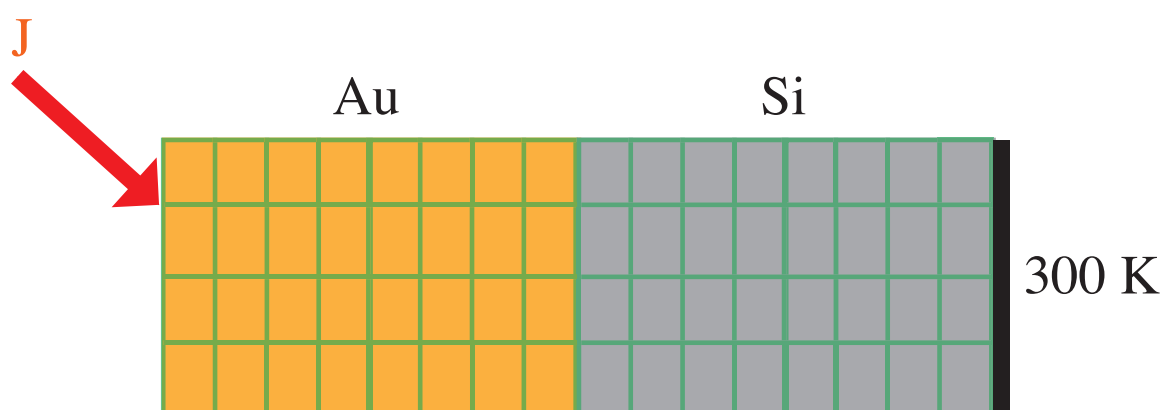


Figure 8.2. Illustration of the simulated Au/Si structure.

### 8.3 Results and Discussions

In this work, we simulate a typical heat transfer process in pump-probe experiments, in which a short-duration “pump” laser is used to inject a large amount of heat flux into the electrons in the metal. After the laser radiation, electron temperature in the metal thin film becomes very high and electrons start depositing energy into the lattice, or phonons, in the metal, since phonons are still at room temperature. As phonon temperature increases, phonon transmission across the interface enables heat dissipation from the hot metal thin film into the Si substrate. The simulated structure is shown in Fig. 8.2. Both the thin film and the Si substrate are 20 nm long. The left end is an adiabatic (reflective) surface and the right end is a constant-temperature heat bath with a length of 1 nm, in which phonon distribution is enforced to be equilibrium Bose-Einstein distribution at 300 K at the beginning of every simulation step. We conduct simulations using same parameters for laser as Guo et al.’s experiment, in which a 390 fs-long laser was used to heat up the electrons in the metal thin film.

Figure 8.3 shows our simulation of heat transfer in a Au-thin-film/Si-substrate system. Figure 8.3a shows how the average temperature of electron and different phonon modes vary with time. As we can see, electron temperature drops quickly from  $\sim 3,000$  K to  $\sim 400$  K in about 10 ps. During the same period, the temperature of LA and TA modes increases gradually. The fluctuation in the temperature of the LA and TA modes is quite large compared to the absolute temperature. The fluctuation can be reduced by including more phonon modes in the simulation. However, this will make the computation too expensive at the moment. Similar to pump-probe experiments, we can also obtain the electron-phonon coupling constant  $G_{ep}$  by fitting the electron temperature decay to an exponential function,  $T_e(t) \propto \exp(-G_{ep}t/c_e)$ , in which we assume lumped capacitance of the electron system. From the curve in Fig. 8.3a,  $G_{ep}$  is found to be  $1.7 \times 10^{16} \text{ W/m}^3\text{-K}$ , which agrees reasonably well with the input of  $2.5 \times 10^{16} \text{ W/m}^3\text{-K}$ .

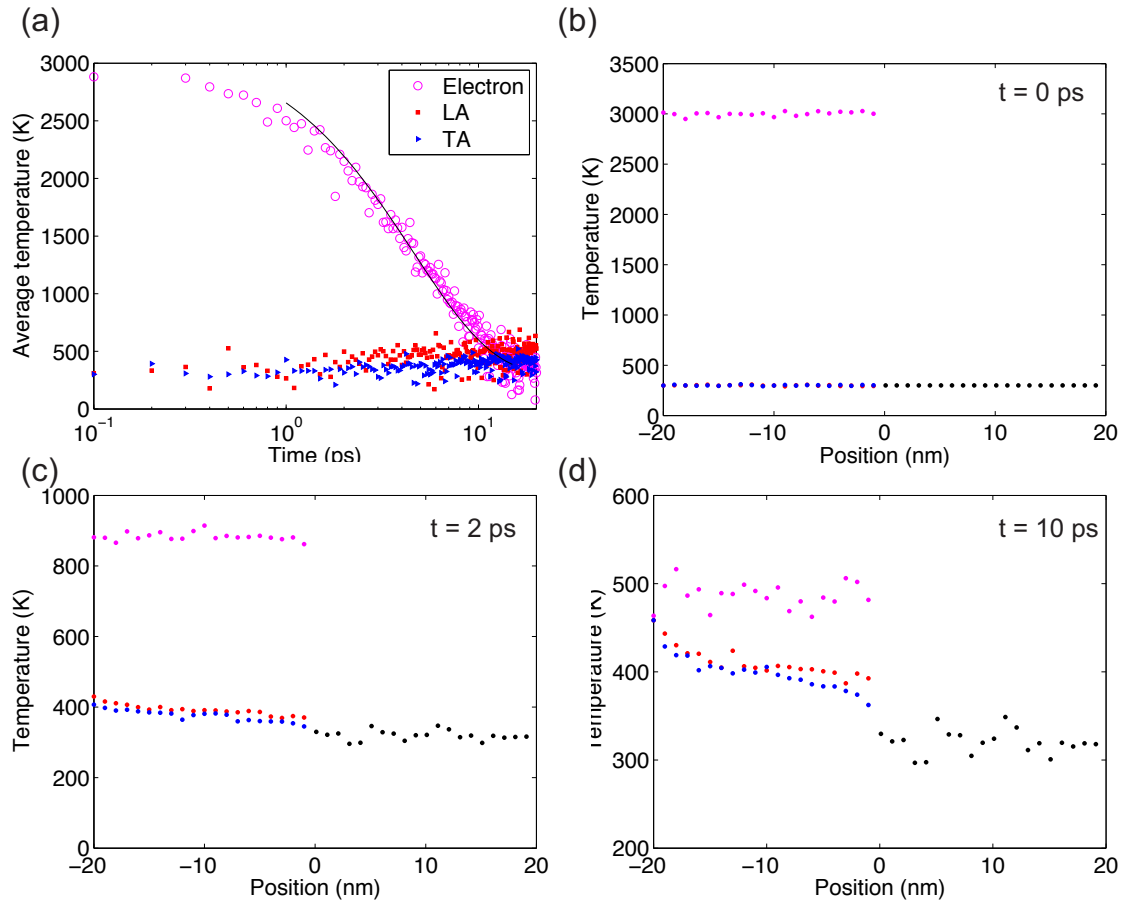


Figure 8.3. Simulation results for a Au/Si system under ultrafast laser radiation. (a) average temperature of electron, LA phonon, and TA phonon as a function of time. The dark line is an exponential fit of the temperature of electrons in the thin film. (b)-(d) temperature profiles at different time instants after the laser radiation.

Figure 8.3b-d show the temperature profiles at different time instants after the laser radiation. In Fig. 8.3b, we can see that at the beginning of the simulation, electron temperature in the thin film is 3,000 K. In Fig. 8.3c, we can see that electron temperature is quite uniform in the metal and it has reduced to  $\sim 900$  K at  $t=7$ ps. It is quite obvious that the temperature of LA modes is generally higher than TA modes. This is even more obvious in Fig. 8.3d. The nonequilibrium between different modes can possibly cause an increased thermal resistance for interfacial thermal transport, similar to our previous work on electron-phonon coupled thermal transport across metal-nonmetal interfaces. Figure 8.3d shows that at  $t=10$ ps, electron temperature has dropped to  $\sim 500$  K, and the temperature of LA and TA phonons have increased, while the nonequilibrium between LA and TA modes persists.

#### 8.4 Summary

In this work, we have developed a Monte-Carlo simulation approach to solve for thermal transport in metal-nonmetal heterojunctions contributed by both electrons and phonons. This approach enables us to conduct a spectral electron-phonon simulation considering the selection rules for three-phonon scatterings. To reduce the computational cost while preserving the accuracy of the physical quantities of interest, we also simplified the simulation by different degrees through a gray approximation of electron channel. We demonstrated the approach using a Au-Si bilayer system under ultrafast laser radiation. Nonequilibrium between electrons and different phonon modes were observed. This approach enables first-principles-based simulation of heat transfer across metal-nonmetal interfaces, which will be useful for designing thermoelectric devices and for thermal management of electronic devices.

## 9. SUMMARY

In this work, we have explored several mechanisms that can affect thermal transport in graphene and its derivatives. The thermal conductivity of zigzag-edged GNRs is found to be higher than that of armchair-edge ones in our MD simulations, and phonon localization at edges is attributed to underlie such edge-chirality dependence. Thermal rectification TR is a phenomenon in which heat flows faster in one direction while slower in the opposite direction, which is particularly useful for thermal management. Using MD simulations, we have found significant TR in asymmetrically defected GNRs and pristine GNRs with asymmetric geometry. However, TR in these two structures arises from different mechanisms. In the former case, GNRs are pristine on one side while defective on the other, and TR is caused by the different temperature dependence of the  $\kappa$  of the two sides. In the latter case, TR can be enabled by phonon lateral confinement when the width of the GNR is smaller than the phonon mean free path. These findings will provide useful guidance to the fabrication of thermal rectifiers from pristine materials including but not limited to graphene.

We have conducted NEMD simulations on conceptual binary Lennard-Jones systems and proposed a two-phonon model to interpret the simulation results for superlattices and random multilayers. Our model considers the coexistence of coherent and incoherent phonon contribution to heat conduction in SLs and RMLs, and can fit the simulation data very well.  $\kappa_{SL}$  and  $\kappa_{RML}$  were found to increase with the total length of the structure, while  $\kappa_{RML} < \kappa_{SL}$  and  $\kappa_{RML}$  saturates at a finite value much sooner than  $\kappa_{SL}$ . We attribute the increasing  $\kappa$  with total length in SLs to coherent phonon transport, and the lower  $\kappa$  of RML than SL to the localization of coherent phonons due to the random layer thickness. Using the two-phonon model, we also extracted the phonon MFP and ballistic-limit thermal conductance of coherent phonons and incoherent phonons. The  $\kappa$  of RMLs can be as low as that of SLs

with interface mixing or roughness, even though RMLs have atomically smooth and planar interfaces. Nonetheless, the reduction of  $\kappa$  in these structures may result from different mechanisms, e.g. localization and scattering, and display different  $G$ - $L_{tot}$  relations. Based on our findings, we propose RMLs as low- $\kappa$  materials that may be used for thermoelectric applications. This work also shows the great tunability of thermal transport in multilayer structures, and our findings are beneficial for thermal management of them.

A two-temperature non-equilibrium MD simulation technique has been developed to atomically model electron-phonon coupled thermal transport across interfaces between metals and semiconductors. On the metal side, the lattice part of thermal transport is modeled with MD while the electronic part is simultaneously modeled with the Fourier's law using the finite difference method. On the semiconductor side, electrons are neglected and only phonons are considered. Our method naturally accounts for the effect of defects, interface, temperature, etc., on thermal properties of phonons and also includes the coupling between electron and phonon. We have used this technique to compute the thermal boundary resistance (TBR) of Si/Cu and CNT/Cu interfaces. In a region within a "cooling length" distance to the interface, electron and phonon are revealed to be in thermal non-equilibrium, which considerably impedes heat transfer across the interface. The TBR of CNT/Cu interfaces predicted using our method is in better agreement with experimental results than conventional MD methods.

A two-temperature Boltzmann transport equation method has also been built. We conducted BTE simulations to study electron-phonon coupled thermal transport in Au-Si systems. We demonstrated that by applying an interlayer with stronger electron-phonon coupling than the original metal film, the effective interfacial thermal resistance can be significantly reduced. This is because the interlayer can drag electrons and phonons back into equilibrium efficiently, thereby reducing the resistance caused by the nonequilibrium between electrons and phonons. Moreover, we observed that interlayers can also cause a faster energy loss of hot electrons. The



reduced interfacial resistance and accelerated electron cooling impose a tradeoff between the lifetime and the energy efficiency of the device, which requires sophisticated thermal design.

We also extracted from first-principles the phonon scattering rates in several metals considering the contribution from both phonon-phonon and phonon-electron scattering processes. It was found that phonon-electron scattering is negligible in Cu, Ag, Au, and Al while it is significant in Pt and Ni at room temperature. Specifically, the room temperature  $\kappa_L$  of Cu, Ag, Au, and Al predicted from density-functional theory calculations with the local-density approximation are 16.9, 5.2, 2.6, and 5.8 W/m-K, respectively, when only phonon-phonon scattering is considered, while phonon-electron scattering was found to be negligible in determining  $\kappa_L$ . In contrast, the room-temperature  $\kappa_L$  of Pt and Ni is reduced from 7.1 and 33.2 W/m-K to 5.8 and 23.2 W/m-K by phonon-electron scattering.

Finally, we developed a Monte-Carlo approach to solve heat transfer problems in metal-nonmetal heterojunctions including both electrons and phonons. This approach enables us to conduct a spectral electron-phonon simulation considering the selection rules for three-phonon scatterings. To reduce the computational cost while preserving the accuracy of the physical quantities of interest, we also simplified the simulation by different degrees through a gray approximation of electron channel. We demonstrated the approach using a Au-Si bilayer system under ultrafast laser radiation. Nonequilibrium between electrons and different phonon modes were observed. This approach enables first-principles-based simulation of heat transfer across metal-nonmetal interfaces, which will be useful for designing thermoelectric devices and for thermal management of electronic devices.

The results obtained in this study will provide a deeper understanding of nanoscale thermal transport involving multiple types of heat carriers, and the approaches developed will aid the thermal design of micro- and nano-devices. This research also provides new perspectives of atomic- and nano-scale engineering of materials and structures to enhance efficiency of thermal management.

## LIST OF REFERENCES

## LIST OF REFERENCES

- [1] M. Waldrop. The chips are down for moores law. *Nature News*, 530(7589):144, 2016.
- [2] E. Pop and K. Goodson. Thermal phenomena in nanoscale transistors. *Journal of electronic packaging*, 128(2):102–108, 2006.
- [3] A. Tilke, L. Pescini, A. Erbe, H. Lorenz, and R. H. Blick. Electron-phonon interaction in suspended highly doped silicon nanowires. *Nanotechnology*, 13(4):491, 2002.
- [4] L. Pan and D. Bogy. Data storage: Heat-assisted magnetic recording. *Nature Photonics*, 3(4):189–190, 2009.
- [5] A. K. Geim and K. S. Novoselov. The rise of graphene. *Nat Mater*, 6(3):183–191, 2007.
- [6] K. Nakada, M. Fujita, G. Dresselhaus, and M. S. Dresselhaus. Edge state in graphene ribbons: Nanometer size effect and edge shape dependence. *Phys. Rev. B*, 54:17954–17961, Dec 1996.
- [7] A. Balandin, S. Ghosh, W. Bao, I. Calizo, D. Teweldebrhan, F. Miao, and C. Lau. Superior thermal conductivity of single-layer graphene. *Nano Letters*, 8(3):902–907, 2008. PMID: 18284217.
- [8] A. Balandin. Thermal properties of graphene and nanostructured carbon materials. *Nat Mater*, 10(8):569–581, 2011.
- [9] J. Hu, X. Ruan, and Y. P. Chen. Thermal conductivity and thermal rectification in graphene nanoribbons: A molecular dynamics study. *Nano Letters*, 9(7):2730–2735, 2009. PMID: 19499898.
- [10] Z. Ong, E. Pop, B. Qiu, and X. Ruan. A flexural resonance mechanism in graphene-sio2 interfacial thermal transport.
- [11] B. Persson and H. Ueba. Heat transfer between graphene and amorphous sio2. *Journal of Physics: Condensed Matter*, 22(46):462201, 2010.
- [12] A. Vallabhaneni, B. Qiu, J. Hu, Y. Chen, A. Roy, and X. Ruan. Interfacial thermal conductance limit and thermal rectification across vertical carbon nanotube/graphene nanoribbon-silicon interfaces. *Journal of Applied Physics*, 113(6):064311–064311, 2013.
- [13] P. A. Khomyakov, G. Giovannetti, P. C. Rusu, G. Brocks, J. van den Brink, and P. J. Kelly. First-principles study of the interaction and charge transfer between graphene and metals. *Phys. Rev. B*, 79:195425, May 2009.

- [14] R. Mao, B. D. Kong, C. Gong, S. Xu, T. Jayasekera, K. Cho, and K. W. Kim. First-principles calculation of thermal transport in metal/graphene systems. *Phys. Rev. B*, 87:165410, Apr 2013.
- [15] Baratunde C., J. Xu, C. Cheng, X. Xu, T. S. Fisher, and H. Hu. Photoacoustic characterization of carbon nanotube array thermal interfaces. *Journal of Applied Physics*, 101(5):054313, 2007.
- [16] M. A. Panzer, H. M. Duong, J. Okawa, J. Shiomi, B. L. Wardle, S. Maruyama, and K. E. Goodson. Temperature-dependent phonon conduction and nanotube engagement in metalized single wall carbon nanotube films. *Nano Letters*, 10(7):2395–2400, 2010.
- [17] D. Wang, M. Carlson, and H. Richardson. Absorption cross section and interfacial thermal conductance from an individual optically excited single-walled carbon nanotube. *ACS nano*, 5(9):7391–7396, 2011.
- [18] S. Shin and M. Kaviani. Interflake thermal conductance of edge-passivated graphene. *Phys. Rev. B*, 84:235433, Dec 2011.
- [19] L. Hu, T. Desai, and P. Keblinski. Determination of interfacial thermal resistance at the nanoscale. *Physical Review B*, 83(19):195423, 2011.
- [20] L. Hu, T. Desai, and P. Keblinski. Thermal transport in graphene-based nanocomposite. *Journal of Applied Physics*, 110(3):–, 2011.
- [21] V. Varshney, S. Patnaik, A. Roy, G. Froudakis, and B. Farmer. Modeling of thermal transport in pillared-graphene architectures. *ACS nano*, 4(2):1153–1161, 2010.
- [22] J. Lee, V. Varshney, J. S. Brown, A. K. Roy, and B. L. Farmer. Single mode phonon scattering at carbon nanotube-graphene junction in pillared graphene structure. *Applied Physics Letters*, 100(18):–, 2012.
- [23] A. Majumdar and P. Reddy. Role of electron–phonon coupling in thermal conductance of metal–nonmetal interfaces. *Applied Physics Letters*, 84(23):4768–4770, 2004.
- [24] Y. Wang, X. Ruan, and A. K. Roy. Two-temperature nonequilibrium molecular dynamics simulation of thermal transport across metal-nonmetal interfaces. *Phys. Rev. B*, 85:205311, May 2012.
- [25] X. Li, B. D. Kong, J. M. Zavada, and K. W. Kim. Strong substrate effects of joule heating in graphene electronics. *Applied Physics Letters*, 99(23):233114, 2011.
- [26] B. Li, L. Wang, and G. Casati. Thermal diode: Rectification of heat flux. *Phys. Rev. Lett.*, 93:184301, Oct 2004.
- [27] C. Starr. The copper oxide rectifier. *Physics*, 7(1):15–19, 1936.
- [28] C. Chang, D. Okawa, A. Majumdar, and A. Zettl. Solid-state thermal rectifier. *Science*, 314(5802):1121–1124, 2006.

- [29] M. Alaghemandi, E. Algaer, M. Böhm, and F. Müller-Plathe. The thermal conductivity and thermal rectification of carbon nanotubes studied using reverse non-equilibrium molecular dynamics simulations. *Nanotechnology*, 20(11):115704, 2009.
- [30] M. Alaghemandi, F. Leroy, E. Algaer, M. Böhm, and F. Müller-Plathe. Thermal rectification in mass-graded nanotubes: a model approach in the framework of reverse non-equilibrium molecular dynamics simulations. *Nanotechnology*, 21(7):075704, 2010.
- [31] N. Yang, G. Zhang, and B. Li. Thermal rectification in asymmetric graphene ribbons. *Applied Physics Letters*, 95(3):033107–033107, 2009.
- [32] G. Wu and B. Li. Thermal rectification in carbon nanotube intramolecular junctions: Molecular dynamics calculations. *Phys. Rev. B*, 76:085424, Aug 2007.
- [33] G. Wu and B. Li. Thermal rectifiers from deformed carbon nanohorns. *Journal of Physics: Condensed Matter*, 20(17):175211, 2008.
- [34] N. Yang, G. Zhang, and B. Li. Carbon nanocone: a promising thermal rectifier. *Applied Physics Letters*, 93(24):243111–243111, 2008.
- [35] Y. Wang, S. Chen, and X. Ruan. Tunable thermal rectification in graphene nanoribbons through defect engineering: A molecular dynamics study. *Applied Physics Letters*, 100(16):163101–163101, 2012.
- [36] K. Gunawardana, K. Mullen, J. Hu, Y. Chen, and X. Ruan. Tunable thermal transport and thermal rectification in strained graphene nanoribbons. *Phys. Rev. B*, 85:245417, Jun 2012.
- [37] P. K. Schelling, S. R. Phillpot, and P. Keblinski. Comparison of atomic-level simulation methods for computing thermal conductivity. *Phys. Rev. B*, 65:144306, Apr 2002.
- [38] F. Müller-Plathe. A simple nonequilibrium molecular dynamics method for calculating the thermal conductivity. *The Journal of Chemical Physics*, 106(14):6082–6085, 1997.
- [39] P. Schelling, S. Phillpot, and P. Keblinski. Phonon wave-packet dynamics at semiconductor interfaces by molecular-dynamics simulation. *Applied Physics Letters*, 80(14):2484–2486, 2002.
- [40] A. J. H. McGaughey and M. Kaviani. Quantitative validation of the boltzmann transport equation phonon thermal conductivity model under the single-mode relaxation time approximation. *Phys. Rev. B*, 69:094303, Mar 2004.
- [41] A. Henry and G. Chen. Spectral phonon transport properties of silicon based on molecular dynamics simulations and lattice dynamics. *Journal of Computational and Theoretical Nanoscience*, 5(2):141–152, 2008.
- [42] R. Car and M. Parrinello. Unified approach for molecular dynamics and density-functional theory. *Phys. Rev. Lett.*, 55:2471–2474, Nov 1985.

- [43] M. Pozzo, C. Davies, D. Gubbins, and D. Alfè. Thermal and electrical conductivity of iron at earth's core conditions. *Nature*, 485(7398):355–358, 2012.
- [44] T. Gibbons, S. Estreicher, C. Carbogno, et al. Thermal conductivity of si nanostructures containing defects: Methodology, isotope effects, and phonon trapping. *Physical Review B*, 84(3):035317, 2011.
- [45] T. M. Gibbons and S. K. Estreicher. Impact of impurities on the thermal conductivity of semiconductor nanostructures: First-principles theory. *Phys. Rev. Lett.*, 102:255502, Jun 2009.
- [46] V. K. Tewary and B. Yang. Singular behavior of the debye-waller factor of graphene. *Phys. Rev. B*, 79:125416, Mar 2009.
- [47] C. Oligschleger and J. Schön. Simulation of thermal conductivity and heat transport in solids. *Physical Review B*, 59(6):4125, 1999.
- [48] A. Casher. Heat flow in regular and disordered harmonic chains. *Journal of Mathematical Physics*, 12(8):1701–1711, 1971.
- [49] R. J. Rubin and W. L. Greer. Abnormal lattice thermal conductivity of a one-dimensional, harmonic, isotopically disordered crystal. *Journal of Mathematical Physics*, 12(8):1686–1701, 1971.
- [50] L. Lee and A. Dhar. Heat conduction in a two-dimensional harmonic crystal with disorder. *Phys. Rev. Lett.*, 95:094302, Aug 2005.
- [51] M. Kaviani. *Heat transfer physics*. Cambridge University Press Cambridge, UK, 2008.
- [52] A. McGaughey and M. Kaviani. Thermal conductivity decomposition and analysis using molecular dynamics simulations. part i. lennard-jones argon. *International Journal of Heat and Mass Transfer*, 47(8):1783–1798, 2004.
- [53] H. Kaburaki, J. Li, and S. Yip. Thermal conductivity of solid argon by classical molecular dynamics. In *Materials Research Society Symposium Proceedings*, volume 538, pages 503–508. Cambridge Univ Press, 1999.
- [54] P. C. Howell. Comparison of molecular dynamics methods and interatomic potentials for calculating the thermal conductivity of silicon. *The Journal of Chemical Physics*, 137(22):224111, 2012.
- [55] K. Esfarjani, G. Chen, and H. Stokes. Heat transport in silicon from first-principles calculations. *Physical Review B*, 84(8):085204, 2011.
- [56] Y. Wang, B. Qiu, and X. Ruan. Edge effect on thermal transport in graphene nanoribbons: A phonon localization mechanism beyond edge roughness scattering. *Applied Physics Letters*, 101(1):013101, 2012.
- [57] A. McGaughey. Predicting phonon properties from equilibrium molecular dynamics simulations. *Annual Review of Heat Transfer*.
- [58] A. J. C. Ladd, B. Moran, and W. G. Hoover. Lattice thermal conductivity: A comparison of molecular dynamics and anharmonic lattice dynamics. *Phys. Rev. B*, 34:5058–5064, Oct 1986.

- [59] N. de Koker. Thermal conductivity of mgo periclase from equilibrium first principles molecular dynamics. *Phys. Rev. Lett.*, 103:125902, Sep 2009.
- [60] W. Zhang, T. S. Fisher, and N. Mingo. The atomistic green's function method: An efficient simulation approach for nanoscale phonon transport. *Numerical Heat Transfer, Part B: Fundamentals*, 51(4):333–349, 2007.
- [61] J. Wang, J. Wang, and N. Zeng. Nonequilibrium green's function approach to mesoscopic thermal transport. *Physical Review B*, 74(3):033408, 2006.
- [62] J. Lan, J. Wang, C. Gan, and S. Chin. Edge effects on quantum thermal transport in graphene nanoribbons: Tight-binding calculations. *Phys. Rev. B*, 79:115401, Mar 2009.
- [63] J. Wang, L. Li, and J. Wang. Tuning thermal transport in nanotubes with topological defects. *Applied Physics Letters*, 99(9):091905, 2011.
- [64] N. Mingo. Anharmonic phonon flow through molecular-sized junctions. *Phys. Rev. B*, 74:125402, Sep 2006.
- [65] G. P. Srivastava. *The physics of phonons*. CRC Press, 1990.
- [66] M. Omini and A. Sparavigna. An iterative approach to the phonon boltzmann equation in the theory of thermal conductivity. *Physica B: Condensed Matter*, 212(2):101–112, 1995.
- [67] L. Lindsay, D. A. Broido, and N. Mingo. Diameter dependence of carbon nanotube thermal conductivity and extension to the graphene limit. *Phys. Rev. B*, 82:161402, Oct 2010.
- [68] L. Lindsay, D. A. Broido, and Natalio Mingo. Flexural phonons and thermal transport in graphene. *Phys. Rev. B*, 82:115427, Sep 2010.
- [69] L. Lindsay, D. Broido, and N. Mingo. Lattice thermal conductivity of single-walled carbon nanotubes: Beyond the relaxation time approximation and phonon-phonon scattering selection rules. *Physical Review B*, 80(12):125407, 2009.
- [70] Z. Aksamija and I. Knezevic. Lattice thermal conductivity of graphene nanoribbons: Anisotropy and edge roughness scattering. *Applied Physics Letters*, 98(14):141919, 2011.
- [71] Y. Xu, X. Chen, B. Gu, and W. Duan. Intrinsic anisotropy of thermal conductance in graphene nanoribbons. *Applied Physics Letters*, 95(23):233116, 2009.
- [72] Z. Tan, J. Wang, and C. Gan. First-principles study of heat transport properties of graphene nanoribbons. *Nano Letters*, 11(1):214–219, 2011.
- [73] W. J. Evans, L. Hu, and P. Koblinski. Thermal conductivity of graphene ribbons from equilibrium molecular dynamics: Effect of ribbon width, edge roughness, and hydrogen termination. *Applied Physics Letters*, 96(20):203112, 2010.
- [74] L. Liu and X. Chen. Effect of surface roughness on thermal conductivity of silicon nanowires. *Journal of Applied Physics*, 107(3):033501, 2010.

- [75] B. Qiu, L. Sun, and X. Ruan. Lattice thermal conductivity reduction in  $\text{bi}_2\text{te}_3$  quantum wires with smooth and rough surfaces: A molecular dynamics study. *Phys. Rev. B*, 83:035312, Jan 2011.
- [76] S. Plimpton. Fast parallel algorithms for short-range molecular dynamics. *J. Comput. Phys.*, 117:1–19, March 1995.
- [77] L. Lindsay and D. A. Broido. Optimized tersoff and brenner empirical potential parameters for lattice dynamics and phonon thermal transport in carbon nanotubes and graphene. *Phys. Rev. B*, 81:205441, May 2010.
- [78] J. Tersoff. New empirical approach for the structure and energy of covalent systems. *Phys. Rev. B*, 37(12):6991–7000, Apr 1988.
- [79] H. Cao, Z. Guo, H. Xiang, and X. Gong. Layer and size dependence of thermal conductivity in multilayer graphene nanoribbons. *Physics Letters A*, 376(4):525 – 528, 2012.
- [80] Z. Guo, D. Zhang, and X. Gong. Thermal conductivity of graphene nanoribbons. *Applied Physics Letters*, 95(16):163103, 2009.
- [81] M. Hu, K. P. Giapis, J. V. Goicochea, X. Zhang, and D. Poulikakos. Significant reduction of thermal conductivity in si/ge core-shell nanowires. *Nano Letters*, 11(2):618–623, 2011.
- [82] J. Chen, G. Zhang, and B. Li. Remarkable reduction of thermal conductivity in silicon nanotubes. *Nano Letters*, 10(10):3978–3983, 2010.
- [83] A. Bodapati, P. Schelling, S. Phillpot, and P. Keblinski. Vibrations and thermal transport in nanocrystalline silicon. *Phys. Rev. B*, 74(24):245207, Dec 2006.
- [84] B. Liang, X. S. Guo, J. Tu, D. Zhang, and J. C. Cheng. An acoustic rectifier. *Nat Mater*, 9(16):989–992, 2010.
- [85] B. Li, J. Lan, and L. Wang. Interface thermal resistance between dissimilar anharmonic lattices. *Phys. Rev. Lett.*, 95:104302, Sep 2005.
- [86] M. Peyrard. The design of a thermal rectifier. *EPL (Europhysics Letters)*, 76(1):49, 2006.
- [87] C. Dames. Solid-state thermal rectification with existing bulk materials. *Journal of Heat Transfer*, 131(6):061301, 2009.
- [88] W. Kobayashi, Y. Teraoka, and I. Terasaki. An oxide thermal rectifier. *Applied Physics Letters*, 95(17):171905, 2009.
- [89] D. Sawaki, W. Kobayashi, Y. Moritomo, and I. Terasaki. Thermal rectification in bulk materials with asymmetric shape. *Applied Physics Letters*, 98(8):081915, 2011.
- [90] J. Lee, V. Varshney, A. Roy, J. Ferguson, and B. Farmer. Thermal rectification in three-dimensional asymmetric nanostructure. *Nano Letters*, 12(7):3491–3496, 2012.
- [91] J. Jiang, J. Wang, and B. Li. Topology-induced thermal rectification in carbon nanodevice. *EPL (Europhysics Letters)*, 89(4):46005, 2010.



- [92] Y. Wang, A. Vallabhaneni, J. Hu, B. Qiu, Y. P. Chen, and X. Ruan. Phonon lateral confinement enables thermal rectification in asymmetric single-material nanostructures. *Nano Letters*, 14(2):592–596, 2014. PMID: 24393070.
- [93] D. B. Go and M. Sen. On the condition for thermal rectification using bulk materials. *Journal of Heat Transfer*, 132(12):124502, 2010.
- [94] X. Zhang, M. Hu, and D. Tang. Thermal rectification at silicon/horizontally aligned carbon nanotube interfaces. *Journal of Applied Physics*, 113(19):194307, 2013.
- [95] Q. Pei, Y. Zhang, Z. Sha, and V. Shenoy. Carbon isotope doping induced interfacial thermal resistance and thermal rectification in graphene. *Applied Physics Letters*, 100(10):101901, 2012.
- [96] H. Bao, X. L. Ruan, and M. Kaviani. Theory of the broadening of vibrational spectra induced by lowered symmetry in yttria nanostructures. *Phys. Rev. B*, 78(12):125417, Sep 2008.
- [97] M. Bae, Z. Li, Z. Aksamija, P. Martin, F. Xiong, Z. Ong, I. Knezevic, and E. Pop. Ballistic to diffusive crossover of heat flow in graphene ribbons. *Nature communications*, 4:1734, 2013.
- [98] T. Ouyang, Y. Chen, Y. Xie, X. L. Wei, K. Yang, P. Yang, and J. Zhong. Ballistic thermal rectification in asymmetric three-terminal graphene nanojunctions. *Phys. Rev. B*, 82:245403, Dec 2010.
- [99] N. A. Roberts and D. G. Walker. Phonon transport in asymmetric saw-tooth nanowires. *ASME Conference Proceedings*, 2011(38921):T30053–T30053–9, 2011.
- [100] H. Tian, D. Xie, Y. Yang, T. Ren, G. Zhang, Y. Wang, C. Zhou, P. Peng, L. Wang, and L. Liu. A novel solid-state thermal rectifier based on reduced graphene oxide. *Sci. Rep.*, 2:523, Jul 2012.
- [101] J. Haskins, A. Kinaci, C. Sevik, H. Sevini, G. Cuniberti, and T. Cgin. Control of thermal and electronic transport in defect-engineered graphene nanoribbons. *ACS Nano*, 5(5):3779–3787, 2011.
- [102] J. Jiang, B. Wang, and J. Wang. First principle study of the thermal conductance in graphene nanoribbon with vacancy and substitutional silicon defects. *Applied Physics Letters*, 98(11):113114, 2011.
- [103] H. Hayashi, Y. Ito, and K. Takahashi. Thermal rectification of asymmetrically-defective materials. *Journal of Mechanical Science and Technology*, 25:27–32, 2011. 10.1007/s12206-010-1008-x.
- [104] R. Venkatasubramanian, E. Siivola, T. Colpitts, and B. O’quinn. Thin-film thermoelectric devices with high room-temperature figures of merit. *Nature*, 413(6856):597–602, 2001.
- [105] T. Harman, P. Taylor, M. Walsh, and B. LaForge. Quantum dot superlattice thermoelectric materials and devices. *Science*, 297(5590):2229–2232, 2002.

- [106] H. Boettner, G. Chen, and R. Venkatasubramanian. Aspects of thin-film superlattice thermoelectric materials, devices, and applications. *MRS bulletin*, 31(03):211–217, 2006.
- [107] I. Chowdhury, R. Prasher, K. Lofgreen, G. Chrysler, S. Narasimhan, R. Mahajan, D. Koester, R. Alley, and R. Venkatasubramanian. On-chip cooling by superlattice-based thin-film thermoelectrics. *Nature Nanotechnology*, 4(4):235–238, 2009.
- [108] G. Chen. *Nanoscale energy transport and conversion: a parallel treatment of electrons, molecules, phonons, and photons*. Oxford University Press, USA, 2005.
- [109] S. Tamura, Y. Tanaka, and H. J. Maris. Phonon group velocity and thermal conduction in superlattices. *Phys. Rev. B*, 60:2627–2630, Jul 1999.
- [110] E. Landry and A. McGaughey. Effect of film thickness on the thermal resistance of confined semiconductor thin films. *Journal of Applied Physics*, 107(1):013521–013521, 2010.
- [111] M. V. Simkin and G. D. Mahan. Minimum thermal conductivity of superlattices. *Phys. Rev. Lett.*, 84:927–930, Jan 2000.
- [112] R. Venkatasubramanian. Lattice thermal conductivity reduction and phonon localizationlike behavior in superlattice structures. *Physical Review B*, 61(4):3091, 2000.
- [113] B. Daly, H. Maris, K. Imamura, and S. Tamura. Molecular dynamics calculation of the thermal conductivity of superlattices. *PHYSICAL REVIEW-SERIES B*, 66(2):024301–024301, 2002.
- [114] B. Yang and G. Chen. Partially coherent phonon heat conduction in superlattices. *Physical Review B*, 67(19):195311, 2003.
- [115] Y. Chen, D. Li, J. Lukes, Z. Ni, and M. Chen. Minimum superlattice thermal conductivity from molecular dynamics. *Physical Review B*, 72(17):174302, 2005.
- [116] J. Garg and G. Chen. Minimum thermal conductivity in superlattices: A first-principles formalism. *Physical Review B*, 87(14):140302, 2013.
- [117] J. Ravichandran, A. Yadav, R. Cheaito, P. Rossen, A. Soukiassian, S. Suresha, J. Duda, B. Foley, C. Lee, Y. Zhu, et al. Crossover from incoherent to coherent phonon scattering in epitaxial oxide superlattices. *Nature materials*, 13(2):168–172, 2014.
- [118] S. Lee, D. Cahill, and R. Venkatasubramanian. Thermal conductivity of si-ge superlattices. *Applied physics letters*, 70(22):2957–2959, 1997.
- [119] W. Capinski, H. Maris, T. Ruf, M. Cardona, K. Ploog, and D. Katzer. Thermal-conductivity measurements of gaas/alas superlattices using a picosecond optical pump-and-probe technique. *Phys. Rev. B*, 59:8105–8113, Mar 1999.
- [120] S. Huxtable, A. Abramson, C. Tien, A. Majumdar, C. LaBounty, X. Fan, G. Zeng, J. Bowers, A. Shakouri, and E. Croke. Thermal conductivity of si/sige and sige/sige superlattices. *Applied Physics Letters*, 80(10):1737–1739, 2002.

- [121] K. Imamura, Y. Tanaka, N. Nishiguchi, S. Tamura, and H. Maris. Lattice thermal conductivity in superlattices: molecular dynamics calculations with a heat reservoir method. *Journal of Physics: Condensed Matter*, 15(50):8679, 2003.
- [122] E. Landry and A. McGaughey. Effect of interfacial species mixing on phonon transport in semiconductor superlattices. *Physical Review B*, 79(7):075316, 2009.
- [123] K. Termentzidis, S. Merabia, P. Chantrenne, and P. Keblinski. Cross-plane thermal conductivity of superlattices with rough interfaces using equilibrium and non-equilibrium molecular dynamics. *International Journal of Heat and Mass Transfer*, 54:2014 – 2020, 2011.
- [124] V. Narayanamurti, H. L. Störmer, M. A. Chin, A. C. Gossard, and W. Wiegmann. Selective transmission of high-frequency phonons by a superlattice: The "dielectric" phonon filter. *Phys. Rev. Lett.*, 43:2012–2016, Dec 1979.
- [125] M. Luckyanova, J. Garg, K. Esfarjani, A. Jandl, M. Bulsara, A. Schmidt, A. Minnich, S. Chen, M. Dresselhaus, Z. Ren, et al. Coherent phonon heat conduction in superlattices. *Science*, 338(6109):936–939, 2012.
- [126] V. Samvedi and V. Tomar. The role of interface thermal boundary resistance in the overall thermal conductivity of sige multilayered structures. *Nanotechnology*, 20(36):365701, 2009.
- [127] K. Lin and A. Strachan. Thermal transport in sige superlattice thin films and nanowires: Effects of specimen and periodic lengths. *Phys. Rev. B*, 87:115302, Mar 2013.
- [128] P. W. Anderson. Absence of diffusion in certain random lattices. *Phys. Rev.*, 109:1492–1505, Mar 1958.
- [129] M. Kohmoto, B. Sutherland, and K. Iguchi. Localization of optics: Quasiperiodic media. *Physical review letters*, 58(23):2436, 1987.
- [130] W. Gellermann, M. Kohmoto, B. Sutherland, and P. Taylor. Localization of light waves in fibonacci dielectric multilayers. *Physical review letters*, 72(5):633, 1994.
- [131] X. Ruan and M. Kaviany. Photon localization and electromagnetic field enhancement in laser-irradiated, random porous media. *Microscale Thermophysical Engineering*, 9(1):63–84, 2005.
- [132] K. Ishii. Localization of eigenstates and transport phenomena in the one-dimensional disordered system. *Progress of Theoretical Physics Supplement*, 53:77–138, 1973.
- [133] S. Tamura and J. Wolfe. Acoustic-phonon transmission in quasiperiodic superlattices. *Physical Review B*, 36(6):3491, 1987.
- [134] N. Nishiguchi, S. Tamura, and F. Nori. Phonon universal-transmission fluctuations and localization in semiconductor superlattices with a controlled degree of order. *Phys. Rev. B*, 48:14426–14435, Nov 1993.

- [135] N. Nishiguchi, S. Tamura, and F. Nori. Phonon-transmission rate, fluctuations, and localization in random semiconductor superlattices: Green-function approach. *Physical Review B*, 48(4):2515, 1993.
- [136] P. Schelling and S. Phillpot. Multiscale simulation of phonon transport in superlattices. *Journal of applied physics*, 93(9):5377–5387, 2003.
- [137] G. Chen. Thermal conductivity and ballistic-phonon transport in the cross-plane direction of superlattices. *Phys. Rev. B*, 57:14958–14973, Jun 1998.
- [138] Z. Aksamija and I. Knezevic. Thermal conductivity of sige superlattices: Competition between interfacial and internal scattering. *Phys. Rev. B*, 88:155318, Oct 2013.
- [139] E. S. Landry, M. I. Hussein, and A. J. H. McGaughey. Complex superlattice unit cell designs for reduced thermal conductivity. *Phys. Rev. B*, 77:184302, May 2008.
- [140] S. C. Huberman, J. M. Larkin, A. J. H. McGaughey, and C. H. Amon. Disruption of superlattice phonons by interfacial mixing. *Phys. Rev. B*, 88:155311, Oct 2013.
- [141] K. Termentzidis, P. Chantrenne, and P. Keblinski. Nonequilibrium molecular dynamics simulation of the in-plane thermal conductivity of superlattices with rough interfaces. *Phys. Rev. B*, 79:214307, Jun 2009.
- [142] S. Datta. *Quantum transport: atom to transistor*. Cambridge University Press, 2005.
- [143] C. Jeong, S. Datta, and M. Lundstrom. Full dispersion versus debye model evaluation of lattice thermal conductivity with a landauer approach. *Journal of Applied Physics*, 109(7):–, 2011.
- [144] C. Jeong, S. Datta, and M. Lundstrom. Thermal conductivity of bulk and thin-film silicon: A landauer approach. *Journal of Applied Physics*, 111(9):–, 2012.
- [145] S. Ren and J. D. Dow. Thermal conductivity of superlattices. *Phys. Rev. B*, 25:3750–3755, Mar 1982.
- [146] A. Frachioni and B. White. Simulated thermal conductivity of silicon-based random multilayer thin films. *Journal of Applied Physics*, 112(1):014320–014320, 2012.
- [147] P. Hyldgaard and G. D. Mahan. Phonon superlattice transport. *Phys. Rev. B*, 56:10754–10757, Nov 1997.
- [148] R. Cheaito, J. Duda, T. Beechem, K. Hattar, J. Ihlefeld, D. Medlin, M. Rodriguez, M. Champion, E. Piekos, and P. Hopkins. Experimental investigation of size effects on the thermal conductivity of silicon-germanium alloy thin films. *Phys. Rev. Lett.*, 109:195901, Nov 2012.
- [149] X. Wu and T. Luo. The importance of anharmonicity in thermal transport across solid-solid interfaces. *Journal of Applied Physics*, 115(1):–, 2014.

- [150] E. T. Swartz and R. O. Pohl. Thermal boundary resistance. *Rev. Mod. Phys.*, 61:605–668, Jul 1989.
- [151] P. E. Hopkins, P. M. Norris, M. S. Tsegaye, and A. W. Ghosh. Extracting phonon thermal conductance across atomic junctions: Nonequilibrium green’s function approach compared to semiclassical methods. *Journal of Applied Physics*, 106(6):063503, 2009.
- [152] Z. Huang, T. S. Fisher, and J. Y. Murthy. Simulation of thermal conductance across dimensionally mismatched graphene interfaces. *Journal of Applied Physics*, 108(11):114310, 2010.
- [153] J. Diao, D. Srivastava, and M. Menon. Molecular dynamics simulations of carbon nanotube/silicon interfacial thermal conductance. *The Journal of Chemical Physics*, 128(16):164708, 2008.
- [154] E. S. Landry and A. J. H. McGaughey. Thermal boundary resistance predictions from molecular dynamics simulations and theoretical calculations. *Phys. Rev. B*, 80:165304, Oct 2009.
- [155] J. E. Turney, A. J. H. McGaughey, and C. H. Amon. Assessing the applicability of quantum corrections to classical thermal conductivity predictions. *Phys. Rev. B*, 79:224305, Jun 2009.
- [156] Z. Lin, R. A. Johnson, and L. V. Zhigilei. Computational study of the generation of crystal defects in a bcc metal target irradiated by short laser pulses. *Phys. Rev. B*, 77:214108, Jun 2008.
- [157] Carolyn P., Rudolph M., and Paul C. A two-temperature model of radiation damage in alpha-quartz. *J. Chem. Phys.*, 133(14):144711, 2010.
- [158] A. Caro and M. Victoria. Ion-electron interaction in molecular-dynamics cascades. *Phys. Rev. A*, 40:2287–2291, Sep 1989.
- [159] Carolyn P. and Paul C. An energy-conserving two-temperature model of radiation damage in single-component and binary lennard-jones crystals. *J. Chem. Phys.*, 131(7), 2009.
- [160] G. L. Eesley. Generation of nonequilibrium electron and lattice temperatures in copper by picosecond laser pulses. *Phys. Rev. B*, 33:2144–2151, Feb 1986.
- [161] L. W. da Silva and M. Kaviany. Micro-thermoelectric cooler: interfacial effects on thermal and electrical transport. *International Journal of Heat and Mass Transfer*, 47(10-11):2417 – 2435, 2004.
- [162] Z. Lin, L. V. Zhigilei, and V. Celli. Electron-phonon coupling and electron heat capacity of metals under conditions of strong electron-phonon nonequilibrium. *Phys. Rev. B*, 77:075133, Feb 2008.
- [163] H. E. Elsayed-Ali, T. B. Norris, M. A. Pessot, and G. A. Mourou. Time-resolved observation of electron-phonon relaxation in copper. *Phys. Rev. Lett.*, 58:1212–1215, Mar 1987.

- [164] F. Banfi, F. Pressacco, B. Revaz, C. Giannetti, D. Nardi, G. Ferrini, and F. Parmigiani. *Ab initio* thermodynamics calculation of all-optical time-resolved calorimetry of nanosize systems: Evidence of nanosecond decoupling of electron and phonon temperatures. *Phys. Rev. B*, 81:155426, Apr 2010.
- [165] D. Duffy and A. Rutherford. Including the effects of electronic stopping and electron-ion interactions in radiation damage simulations. *Journal of Physics: Condensed Matter*, 19(1):016207, 2007.
- [166] A. Rutherford and D. Duffy. The effect of electron-ion interactions on radiation damage simulations. *Journal of Physics: Condensed Matter*, 19(49):496201, 2007.
- [167] S. Shin, M. Kaviany, T. Desai, and R. Bonner. Roles of atomic restructuring in interfacial phonon transport. *Phys. Rev. B*, 82:081302, Aug 2010.
- [168] T. Beechem, S. Graham, P. Hopkins, and P. Norris. Role of interface disorder on thermal boundary conductance using a virtual crystal approach. *Applied Physics Letters*, 90(5):054104, 2007.
- [169] S. M. Foiles, M. I. Baskes, and M. S. Daw. Embedded-atom-method functions for the fcc metals cu, ag, au, ni, pd, pt, and their alloys. *Phys. Rev. B*, 33:7983–7991, Jun 1986.
- [170] C. Y. Ho P. E. Liley Powell, R.W. *Thermal conductivity of selected materials*. U.S. Govt. Print. Off., 1966.
- [171] B. Feng, Z. Li, and X. Zhang. Role of phonon in the thermal and electrical transports in metallic nanofilms. *Journal of Applied Physics*, 105(10):104315, 2009.
- [172] E. B. Webb, J. A. Zimmerman, and S. Seel. Reconsideration of continuum thermomechanical quantities in atomic scale simulations. *Mathematics and Mechanics of Solids*, 13(3-4):221–266, 2008.
- [173] Z. Hong S. Hwang, Y. Li. *Recent researches in mechanics*. WSEAS Press, 2011.
- [174] H. Hwang, O. Kwon, and J. Kang. Copper nanocluster diffusion in carbon nanotube. *Solid State Communications*, 129(11):687 – 690, 2004.
- [175] B. I. Cho, K. Engelhorn, A. A. Correa, T. Ogitsu, C. P. Weber, H. J. Lee, J. Feng, P. A. Ni, Y. Ping, A. J. Nelson, D. Prendergast, R. W. Lee, R. W. Falcone, and P. A. Heimann. Electronic structure of warm dense copper studied by ultrafast x-ray absorption spectroscopy. *Phys. Rev. Lett.*, 106:167601, Apr 2011.
- [176] B. A. Cola, J. Xu, C. Cheng, X. Xu, T. S. Fisher, and H. Hu. Photoacoustic characterization of carbon nanotube array thermal interfaces. *Journal of Applied Physics*, 101(5):054313, 2007.
- [177] Q. Liang, X. Yao, W. Wang, Y. Liu, and C. Wong. A three-dimensional vertically aligned functionalized multilayer graphene architecture: An approach for graphene-based thermal interfacial materials. *ACS Nano*, 5(3):2392–2401, 2011.

- [178] B. Liao, B. Qiu, J. Zhou, S. Huberman, K. Esfarjani, and G. Chen. Significant reduction of lattice thermal conductivity by the electron-phonon interaction in silicon with high carrier concentrations: A first-principles study. *Physical review letters*, 114(11):115901, 2015.
- [179] X. Tang and B. Fultz. First-principles study of phonon linewidths in noble metals. *Physical Review B*, 84(5):054303, 2011.
- [180] J. Ziman. *Electrons and phonons: the theory of transport phenomena in solids*. Oxford University Press, 1960.
- [181] A. Ward, D. Broido, D. Stewart, and G. Deinzer. Ab initio theory of the lattice thermal conductivity in diamond. *Physical Review B*, 80(12):125203, 2009.
- [182] P. Giannozzi, S. Baroni, N. Bonini, M. Calandra, R. Car, C. Cavazzoni, D. Ceresoli, G. Chiarotti, M. Cococcioni, et al. Quantum espresso: a modular and open-source software project for quantum simulations of materials. *Journal of Physics: Condensed Matter*, 21(39):395502, 2009.
- [183] L. Paulatto, F. Mauri, and M. Lazzeri. Anharmonic properties from a generalized third-order ab initio approach: Theory and applications to graphite and graphene. *Physical Review B*, 87(21):214303, 2013.
- [184] Dario A. Phon: A program to calculate phonons using the small displacement method. *Computer Physics Communications*, 180(12):2622 – 2633, 2009. 40 {YEARS} {OF} CPC: A celebratory issue focused on quality software for high performance, grid and novel computing architectures.
- [185] J. P. Perdew, K. Burke, and M. Ernzerhof. Generalized gradient approximation made simple. *Phys. Rev. Lett.*, 77:3865–3868, Oct 1996.
- [186] J. P. Perdew and Y. Wang. Accurate and simple analytic representation of the electron-gas correlation energy. *Phys. Rev. B*, 45:13244–13249, Jun 1992.
- [187] W. Li, J. Carrete, N. A. Katcho, and N. Mingo. Shengbte: A solver of the boltzmann transport equation for phonons. *Computer Physics Communications*, 185(6):1747 – 1758, 2014.
- [188] S. Baroni, S. De Gironcoli, A. Dal Corso, and P. Giannozzi. Phonons and related crystal properties from density-functional perturbation theory. *Reviews of Modern Physics*, 73(2):515, 2001.
- [189] P. Allen. Neutron spectroscopy of superconductors. *Physical Review B*, 6(7):2577, 1972.
- [190] X. Gonze, B. Amadon, P.-M. Anglade, J.-M. Beuken, F. Bottin, P. Boulanger, F. Bruneval, D. Caliste, R. Caracas, T. Deutsch, L. Genovese, Ph. Ghosez, M. Giantomassi, S. Goedecker, D.R. Hamann, P. Hermet, F. Jollet, G. Jomard, S. Leroux, M. Mancini, S. Mazevet, M.J.T. Oliveira, G. Onida, Y. Pouillon, T. Rangel, G.-M. Rignanese, D. Sangalli, R. Shaltaf, M. Torrent, M.J. Verstraete, G. Zerah, and J.W. Zwanziger. Abinit: First-principles approach to material and nanosystem properties. *Computer Physics Communications*, 180(12):2582 – 2615, 2009. 40 {YEARS} {OF} CPC: A celebratory issue focused on quality software for high performance, grid and novel computing architectures.

- [191] P. Allen. Empirical electron-phonon  $\lambda$  values from resistivity of cubic metallic elements. *Physical Review B*, 36(5):2920, 1987.
- [192] W. L. McMillan. Transition temperature of strong-coupled superconductors. *Phys. Rev.*, 167:331–344, Mar 1968.
- [193] S. Y. Savrasov and D. Y. Savrasov. Electron-phonon interactions and related physical properties of metals from linear-response theory. *Phys. Rev. B*, 54:16487–16501, Dec 1996.
- [194] A. Cohen, P. Mori-Sánchez, and W. Yang. Challenges for density functional theory. *Chemical Reviews*, 112(1):289–320, 2011.
- [195] E. C. Svensson, B. N. Brockhouse, and J. M. Rowe. Crystal dynamics of copper. *Phys. Rev.*, 155:619–632, Mar 1967.
- [196] Y. Wang, Z. Lu, and X. Ruan. First principles calculation of lattice thermal conductivity of metals considering phonon-phonon and phonon-electron scattering. *Journal of Applied Physics*, 119(22), 2016.
- [197] W. Kamitakahara and B. Brockhouse. Crystal dynamics of silver. *Physics Letters A*, 29(10):639–640, 1969.
- [198] J. W. Lynn, H. G. Smith, and R. M. Nicklow. Lattice dynamics of gold. *Phys. Rev. B*, 8:3493–3499, Oct 1973.
- [199] R. E. B. Makinson. The thermal conductivity of metals. *Mathematical Proceedings of the Cambridge Philosophical Society*, 34:474–497, 7 1938.
- [200] J. M. Ziman. Xvii. the effect of free electrons on lattice conduction. *Philosophical Magazine*, 1(2):191–198, 1956.
- [201] D. Dutton, B. Brockhouse, and A. Miiller. Crystal dynamics of platinum by inelastic neutron scattering. *Canadian Journal of Physics*, 50(23):2915–2927, 1972.
- [202] R. Birgeneau, J. Cordes, G. Dolling, and A. Woods. Normal modes of vibration in nickel. *Physical Review*, 136(5A):A1359, 1964.
- [203] R. Stedman and G. Nilsson. Dispersion relations for phonons in aluminum at 80 and 300k. *Phys. Rev.*, 145:492–500, May 1966.
- [204] S. S. Ghai, W. Kim, R. Escobar, C. Amon, and M. Jhon. A novel heat transfer model and its application to information storage systems. *Journal of Applied Physics*, 97(10):–, 2005.
- [205] D. Sellan, J. Turney, A. McGaughey, and C. Amon. Cross-plane phonon transport in thin films. *Journal of Applied Physics*, 108(11):113524, 2010.
- [206] J. Loy, D. Singh, and J. Murthy. Non-gray phonon transport using a hybrid bte-fourier solver. In *ASME 2009 Heat Transfer Summer Conference collocated with the InterPACK09 and 3rd Energy Sustainability Conferences*, pages 601–610. American Society of Mechanical Engineers, 2009.



- [207] Y. Wang, Z. Lu, A. Roy, and X. Ruan. Effect of interlayer on interfacial thermal transport and hot electron cooling in metal-dielectric systems: An electron-phonon coupling perspective. *Journal of Applied Physics*, 119(6), 2016.
- [208] F. Sears, M. Zemansky, and H. Young. *University physics*. Addison-Wesley, 1982.
- [209] N. Ashcroft. Nd mermin solid state physics. *Saunders College, Philadelphia*, 1976.
- [210] P. Reddy, K. Castelino, and A. Majumdar. Diffuse mismatch model of thermal boundary conductance using exact phonon dispersion. *Applied Physics Letters*, 87(21):–, 2005.
- [211] B. Gundrum, D. Cahill, and R. Averback. Thermal conductance of metal-metal interfaces. *Phys. Rev. B*, 72:245426, Dec 2005.
- [212] B. F. Donovan, C. J. Szwejkowski, J. C. Duda, R. Cheaito, J. T. Gaskins, and P. E. Hopkins. Thermal boundary conductance across metal-gallium nitride interfaces from 80 to 450 k. *Applied Physics Letters*, 105(20):–, 2014.
- [213] L. Guo, S. L. Hodson, T. S. Fisher, and X. Xu. Heat transfer across metal-dielectric interfaces during ultrafast-laser heating. *Journal of Heat Transfer*, 134(4):042402, 2012.
- [214] S. Stackhouse, L. Stixrude, and B. Karki. Thermal conductivity of periclase (mgo) from first principles. *Phys. Rev. Lett.*, 104:208501, May 2010.
- [215] S. Mazumder and A. Majumdar. Monte carlo study of phonon transport in solid thin films including dispersion and polarization. *Journal of Heat Transfer*, 123(4):749–759, 2001.
- [216] D. Lacroix, K. Joulain, and D. Lemonnier. Monte carlo transient phonon transport in silicon and germanium at nanoscales. *Physical Review B*, 72(6):064305, 2005.
- [217] Y. Chen, D. Li, J. Lukes, and A. Majumdar. Monte carlo simulation of silicon nanowire thermal conductivity. *Journal of Heat Transfer*, 127(10):1129–1137, 2005.
- [218] J. Péraud and N. Hadjiconstantinou. Efficient simulation of multidimensional phonon transport using energy-based variance-reduced monte carlo formulations. *Physical Review B*, 84(20):205331, 2011.

VITA

## VITA

Yan Wang obtained his B.S. degree in Mechanical Engineering from Tsinghua University, Beijing, China, in 2010. Currently he is a graduate research assistant in the Nanoscale Energy Transport and Conversion Lab at Purdue University, West Lafayette, USA. He is pursuing Ph.D. degree in Mechanical Engineering at Purdue University, West Lafayette, USA. His primary research interest lies in energy transport and conversion processes over a wide spectrum of time and length scales, designing micro/nano-materials for thermal management and thermoelectric applications, and developing theoretical and computational approaches to model and simulate thermal transport processes in nanostructures. Yan Wang received the College of Engineering Outstanding Graduate Research Award (2015), the Bilsland Dissertation Fellowship (2014-2015), and the Frederick N. Andrews Fellowship (2010-2012) from Purdue University.